

# **Photon and Dark Counts in NbN Superconducting Single-Photon Detectors and Nanostripes**

by

**Jennifer Kitaygorsky**

Submitted in partial fulfillment  
of the  
Requirements for the Degree  
Doctor of Philosophy

Supervised by  
Professor Roman Sobolewski

Department of Electrical and Computer Engineering  
The College  
School of Engineering and Applied Science

University of Rochester  
Rochester, New York

2008

To Michail and Aleksandra  
and  
Christopher Bruce Crosby

## **Curriculum Vitae**

Jennifer Kitaygorsky was born in Kiev, the Ukraine, in 1978. She attended the University of Colorado at Denver from 1998 to 2001, and received a Bachelor of Science degree in Physics in May of 2001. She came to the University of Rochester for graduate study at the Department of Electrical and Computer Engineering in 2002. She received a Master of Science degree in 2005, and continued to pursue her doctoral study in superconducting detectors and intrinsic properties of low-dimensional superconductors under the supervision of Professor Roman Sobolewski. Ms. Kitaygorsky is a member of IEEE and American Physical Society.

## List of refereed journals and published conference proceedings

### 2008

12. “Resolving dark pulses from photon pulses in NbN superconducting single-photon detectors,” **J. Kitaygorsky**, R. Schouten, E. Reiger, V. Zwiller, R. Sobolewski, to appear in *J. Mod. Opt.* (2008).
11. “Registration of infrared single photons by a two-channel receiver based on fiber-coupled superconducting single-photon detectors,” O. Okunev, G. Chulkova, I. Milostnaya, A. Antipov, K. Smirnov, D. Morozov, A. Korneev, B. Voronov, G. Gol’tsman, W. Slysz, M. Wegrzecki, J. Bar, P. Grabiec, M. Górska, A. Pearlman, A. Cross, J. Kitaygorsky, and R. Sobolewski in *Second International Conference on Advanced Optoelectronics and Lasers*, ed. By I. A. Sukhoivanov, V. A. Svich, and Y. S. Shmaliy, *Proc. Of SPIE*, **7009**, 70090V, (2008).

### 2007

10. “Spectroscopy with nanostructured superconducting single-photon detectors,” E. Reiger, S. Dorenbos, V. Zwiller, A. Korneev, G. Chulkova, I. Milostnaya, O. Minaeva, G. Gol’tsman, **J. Kitaygorsky**, D. Pan, W. Slysz, A. Jukna, R. Sobolewski, *IEEE Journal of Selected Topics in Quantum Electronics*, **13**, 934-943 (2007).
9. “Dark counts in nanostructured NbN superconducting single photon detectors and bridges,” **J. Kitaygorsky**, I. Komissarov, A. Jukna, O. Minaeva, N. Kaurova, A. Divochiy, A. Korneev, M. Tarkhov, B. Voronov, I. Milostnaya, G. Gol’tsman, R. Sobolewski, *IEEE Trans. Applied Superconductivity*, **17**, 275-278 (2007).
8. “Middle-infrared to visible-light ultrafast superconducting single-photon detectors,” G. Gol’tsman, O. Minaeva, A. Korneev, M. Tarkhov, I. Rubtsova, A. Divochiy, I. Milostnaya, G. Chulkova, N. Kaurova, B. Voronov, D. Pan, **J. Kitaygorsky**, A. Cross, A. Pearlman, I. Komissarov, W. Slysz, M. Wegrzecki, P. Grabiec, R. Sobolewski, *IEEE Trans. Applied Superconductivity*, **17**, 246-251 (2007).
7. “Fibre-coupled, single-photon detector based on NbN superconducting nanostructures for quantum communications,” W. Slysz, M. Wegrzecki, J. Bar, P. Grabiec, M. Gorska, V. Zwiller, C. Latta, P. Bohi, A. J. Pearlman, A. S. Cross, D. Pan, **J. Kitaygorsky**, I. Komissarov, A. Verevkin, I. Milostnaya, A. Korneev, O. Minaeva, G. Chulkova, K. Smirnov, B. Voronov, G. N. Gol’tsman, and Roman Sobolewski, *Journal of Modern Optics*, **54**, 315-326 (2007).
6. “Ultrafast and high quantum efficiency large-area superconducting single-photon detectors,” A. Korneev, O. Minaeva, A. Divochiy, A. Antipov, N. Kaurova, V. Seleznev, B. Voronov, G. Gol’tsman, D. Pan, **J. Kitaygorsky**, W. Slysz, R. Sobolewski, *SPIE Proceedings*, **6583**, 65830I (2007).

5. “Fiber-coupled NbN superconducting single-photon detectors for quantum correlation measurements,” W. Slysz, M. Wegrzecki, J. Bar, P. Grabiec, M. Gorska, E. Reiger, S. Dorenbos, V. Zwiller, I. Milostnaya, O. Minaeva, A. Antipov, O. Okunev, A. Korneev, K. Smirnov, B. Voronov, N. Kaurova, G. N. Gol’tsman, **J. Kitaygorsky**, D. Pan, A. Pearlman, A. Cross, I. Komissarov, and Roman Sobolewski, *SPIE Proceedings*, **6583**, 65830J (2007).

#### 2006

4. “Superconducting single-photon detectors designed for operation at 1.55- $\mu$ m telecommunication wavelength,” I. Milostnaya, A. Korneev, I. Rubtsova, V. Seleznev, O. Minaeva, G. Chulkova, O. Okunev, B. Voronov, K. Smirnov, G. Gol’tsman, W. Slysz, M. Wegrzecki, M. Guzewicz, J. Bar, M. Gorska, A. Pearlman, **J. Kitaygorsky**, A. Cross, R. Sobolewski, *Journal of Physics: Conference Series*, **43**, no.1, 1334-7 (2006).

#### 2005

3. “Origin of dark counts in nanostructured NbN single-photon detectors,” **J. Kitaygorsky**, J. Zhang, A. Verevkin, A. Korneev, V. Matvienko, P. Kouminov, K. Smirnov, B. Voronov, G. Gol’tsman, R. Sobolewski, *IEEE Transactions on Applied Superconductivity*, **15**, no.2, 545-8 (2005).
2. “Registration of infrared single photons by a two-channel receiver based on fiber-coupled superconducting single-photon detectors,” O. Okunev, G. Chulkova, I. Milostnaya, A. Antipov, K. Smirnov, D. Morozov, A. Korneev, B. Voronov, G. Gol’tsman, W. Slysz, M. Wegrzecki, J. Bar, P. Grabiec, M. Gorska, A. Pearlman, A. Cross, **J. Kitaygorsky**, R. Sobolewski, *Proceedings of the CAOL 2005. 2<sup>nd</sup> International Conference on Advanced Optoelectronics and Lasers, IEEE Part vol. 2*, 282-285 (2005).

Figure 6. □ “Superconducting nanostructures for counting of single photons in the infrared range,” G. Chulkova, I. Milostnaya, A. Korneev, O. Minaeva, I. Rubtsova, B. Voronov, O. Okunev, K. Smirnov, G. Gol’tsman, **J. Kitaygorsky**, A. Cross, A. Pearlman, R. Sobolewski, W. Slysz, *Proceedings of the CAOL 2005. 2<sup>nd</sup> International Conference on Advanced Optoelectronics and Lasers, IEEE Part vol. 2*, 100-103 (2005).

## Acknowledgements

First and foremost, I would like to thank my advisor, Prof. Roman Sobolewski, for all his support, and the opportunities he provided for me. Because of him, I was able to travel for research work to other countries, and meet with many great scientists.

I would also like to acknowledge all the members of our Ultrafast Phenomena research group, in particular, Allen Cross and Dong Pan. Also thanks to our past group members, Dr. Ivan Komissarov, Dr. Aaron Pearlman, and Dr. Jin Zhang, who led the research effort in superconducting detectors. Also our visiting scientists, Drs. Arturas Jukna for helpful discussions about transport properties of superconductors, and Wojtek Slysz for experimental help.

I am very grateful to our collaborators from the Moscow State Pedagogical University, Drs. Gregory Gol'tsman and Boris Voronov, also Natalie Kaurova and Olga Minaeva, who helped me learn the fabrication process and provided me with devices. Also, from the Delft University of Technology, Dr. Val Zwiller, Dr. Elisabeth Reiger, and Mr. Raymond Schouten, who allowed me to take over their laboratory for six months in an effort to achieve photon-number resolution, as well as Prof. Hans Mooij for helpful discussions. I am also grateful for being able to work in the past with Dr. Sae Woo Nam from NIST in Boulder, CO, who taught me many useful experimental techniques early in my career.

Finally, I would like to thank the Civilian Research and Development Foundation for a travel fellowship I received from them, which allowed me to travel to Moscow.

This work was supported in part by the US AFOSR under Grant FA9550-04-1-0123 and FA9550-06-1-0348 (Rochester), in part by the CRDF under Grant RE2-2529-MO-03 (Moscow and Rochester), the NYSTAR grant to the University of Rochester CAT-EIS, INTAS 03-51-4145, and the CRDF travel grant RUP1-2676-MO-05.

## Abstract

Nanostructured NbN superconducting single-photon detectors (SSPDs) are fast and reliable photon counters that have become a highly desired technology in recent years. SSPDs feature counting rates up to 250 MHz in the wavelength range from UV to mid-IR, along with very low dark count rates, low timing jitter, and high detection efficiencies.

Nanosecond and sub-nanosecond spontaneous transient voltage pulses, or dark counts, are studied in SSPDs along with NbN nanostripes of various dimensions. Dark counts, along with quantum efficiency (QE), determine the ultimate SSPD sensitivity. In experiments, the detector was completely isolated from the outside world by a metallic shield, and kept at temperatures below the superconducting critical temperature. Dark counts are associated with the formation of phase-slip centers, and dissociation of vortex-antivortex pairs, due to thermal fluctuations. Both temperature and current dependences are studied extensively. Additionally, resistive transitions of different samples are investigated, as well as their transport properties.

Investigation of the photodetection mechanism, which requires understanding of hotspot dynamics, is presented. This was accomplished by measuring the QE dependence on temperature; it was found that QE increases monotonically with decreasing temperature.

Additionally, two different read-out schemes are presented: the first is the standard scheme, where SSPDs act as photon counters, and dark counts are



indistinguishable from photon counts. The second scheme is based on integrating the SSPD with a low-noise cryogenic HEMT amplifier with high-input impedance, which allows us to achieve amplitude resolution of the recorded output transients. The new read-out technique should enable photon-number resolving capability of standard devices, and possibly even energy-resolving capability, while also allowing us to study further the physics of dark counts and the photoresponse mechanism.

## Table of Contents

<b>Chapter 1</b>	Superconducting single-photon detectors .....	1
1.1	Fabrication and material characterization .....	3
1.2	Photoresponse mechanisms in superconductors .....	10
1.3	Electrical model and device performance .....	13
1.4	Thesis motivation .....	17
1.5	Outline of the thesis .....	19
<b>Chapter 2</b>	Experimental methods .....	20
2.1	Dark counts .....	20
2.2	Photon counts and quantum efficiency .....	23
2.3	HEMT-amplifier-based detection setup .....	24
2.4	PSpice simulations and circuit limitations .....	26
<b>Chapter 3</b>	Dissipation and fluctuations in low-dimensional superconductors .....	33
3.1	Introduction .....	33
3.2	Fluctuations in 2D superconductors: vortex-antivortex pairs .....	35
3.3	Fluctuations in 1D superconductors: phase slip centers .....	36
3.4	Resistive transitions .....	38
3.4.1	Two-dimensional nanostripes .....	39
3.4.2	One-dimensional nanowires .....	40
3.4.3	Resistance measurements .....	41
3.5	Current-voltage characteristics .....	45
3.6	Summary .....	48

<b>Chapter 4</b> Dark counts: experimental results and interpretation.....	50
4.1 Experimental results.....	50
4.2 Early data and discussion.....	52
4.3 Vortex-antivortex unbinding approach.....	56
4.3.1 Pulse amplitudes.....	58
4.4 Summary.....	60
<b>Chapter 5</b> Hotspot dynamics.....	62
5.1 Hotspot model.....	62
5.1.1 Hotspot radius.....	64
5.2 Revised hotspot model: heating effects and resistive domain wall propagation.....	68
5.3 Fluctuation-enhanced photodetection: vortex-antivortex pairs.....	75
5.4 Summary.....	76
<b>Chapter 6</b> Toward photon-number resolution.....	77
6.1 Introduction.....	77
6.2 Experimental results.....	79
6.3 Photon-number resolution.....	84
6.4 Summary.....	90
<b>Chapter 7</b> Conclusions and future work.....	92

## List of Tables

<b>Table 1.1</b> Comparison of single-photon detectors .....	16
<b>Table 3.1</b> Device parameters .....	41
<b>Table 4.1</b> Parameters of measured devices .....	51

## List of Figures

Figure 1.1 SEM images of SSPDs. (a) One of the older devices with 150 nm stripe width, the red dotted line shows the meander structure. (b) A latest device with $10 \times 10 \mu\text{m}^2$ active area and 120 nm stripe width, NbN here is black. ....	4
Figure 1.2 Sheet resistance dependence on temperature for a typical SSPD.....	5
Figure 1.3 Comparison of resistance dependence on temperature for a NbN film, and a typical SSPD. ....	5
Figure 1.4 SSPD fabrication process, direct e-beam lithography. ....	8
Figure 1.5 Nanobridge fabrication process, lift-off e-beam lithography. There are two bridges, completely isolated from each other, on each chip. ....	9
Figure 1.6 Two-temperature model. After photoabsorption, electrons thermalize on a $\tau_T$ time scale. The energy from the electron subsystem is then transferred to the phonon subsystem with a time $\tau_{e-ph}$ . Some of the phonons give the energy back to the electron subsystem with time $\tau_{ph-e}$ , and the phonon escape time into the substrate is given by $\tau_{es}$ . ....	11
Figure 1.7 Rothwarf-Taylor model, (a) a photon breaks a Cooper pair to create a highly-excited quasiparticle, which breaks other Cooper pairs via electron-electron and electron-phonon interactions. (b) Quasiparticles begin to recombine and emit acoustic phonons with energy $2\Delta$ . (c) $2\Delta$ -phonons have enough energy to break other Cooper pairs. (d) Phonons escape to the substrate. ....	12

Figure 1.8 (a) Transient voltage pulse corresponding to a single-photon event (black line), a simulated photoresponse (dashed line). (b) Equivalent electrical model of the photoresponse mechanism [23]. .....	15
Figure 1.9 Comparison of dark-count event (dotted line) with a photon-count event (gray line).....	18
Figure 1.10 (a) Typical QE dependence on bias current and (b) dark counting rate dependence on bias current at temperatures 2.0 (red symbols) and 4.2 K (black symbols). The dashed lines indicate typical operation point, $I_b/I_c = 0.9$ .....	18
Figure 2.1 SEM image of two nanobridge structures on the same chip. ....	20
Figure 2.2 Experimental setup for dark count measurements.....	22
Figure 2.3 Low-bias resistance measurement schematic. The current source is the 26.1 Hz voltage oscillator in series with a 100 k $\Omega$ resistor. The lock-in amplifier reads out the voltage across the SSPD. ....	23
Figure 2.4 Fiber-based experimental setup.....	24
Figure 2.5 Circuit schematics implementing HEMT amplifier and a 500- $\Omega$ load resistor, $R_L$ . The 10 nF capacitor sets the maximum AC gain and 200- $\Omega$ resistor sets the DC current for the HEMT; $R_{bias}$ and $R_D$ are the biasing and pull-up resistors, respectively. The inset shows the actual physical layout. ....	26
Figure 2.6 PSpice simulations of voltage transients at different values of $R_L$ : 50 $\Omega$ (black curve), 270 $\Omega$ (red curve), 500 $\Omega$ (green curve), and 2 k $\Omega$ (blue curve); and (b) measured photoresponse (black curve) and simulated photoresponse (red curve), for $R_L = 500 \Omega$ . ....	27

Figure 2.7 Comparison of a latching event (black curve), where the pulse rise-time is simply the relaxation time of the HEMT, and a typical photodetection event (red curve). ..... 29

Figure 2.8 Current flowing through the SSPD at the time of a photodetection event,  $t = 0$ . In (b),  $I_b$  overshoots  $I_c$  at  $t = 5$  ns, leading the device to latch. Here,  $I_c = 18$   $\mu$ A. .... 29

Figure 2.9 (a) Current monitored through the SSPD during a photodetection event. Here, the switch remains open in order to observe better what happens to the current. (b) Comparison of two voltage pulses when the switch for a double-hotspot closes twice as fast. (c) Comparison of two voltage pulses when the switch for a single hotspot ( $t = 0$ ) closes as fast as that for a double-hotspot ( $t = 15$  ns). .... 32

Figure 3.1 Resistive transition in low-dimensional superconductors. Above  $T_c$ , the magnitude of the superconducting order parameter fluctuates, while below  $T_c$ , the phase of the order parameter fluctuates until a second transition temperature is reached, in this case, at  $T_{BKT}$ . .... 34

Figure 3.2 Resistance versus temperature measurements for devices (a) B1 and (b) B2. The blue curves are fits from (3.7), and green curves are fits from (3.13). The insets show the measurements on a linear scale, with fits from (3.4). ..... 42

Figure 3.3 Resistance versus temperature measurements for devices E11. The green curve is a fit from (3.13), with (3.7) plotted for comparison (blue curve). The inset shows the measurements on a linear scale, with a fit from (3.4). ..... 45

- Figure 3.4 (a) *IV* characteristics different temperatures near the superconducting transition for device B3. From left to right, the temperatures are: 10.06, 9.53, 9.27, 9.17, 9.07, 9.02, 8.88, and 8.68 K. (b) Exponent  $\alpha$  as a function of  $T$ . The BKT transition occurs at  $T = 9.17$  K. .... 47
- Figure 3.5 Current-voltage characteristics measured for device B4 at different temperatures. The inset shows the curve at  $T = 4.2$  K once again, to demonstrate that the voltage steps have excess current (slope does not go back to the origin). The curves are also hysteretic. .... 48
- Figure 4.1 Dark-count pulses for (a) device F and (b) device B at temperatures of 2.0 K (solid black line), 4.5 K (gray line), and 7.0 K (dotted line). The inset in (a) shows a typical dark-count pulse from device E, while the inset in (b) corresponds to device A. .... 52
- Figure 4.2 Dark counting rate dependence on the bias current for device A, in the temperature range between 100 mK and 6.4 K. The solid lines are fits according to the PSC model, with  $R_0$  and  $I_0$  as fitting parameters. .... 53
- Figure 4.3 Characteristic current for devices A, B, C, and D, extracted from dark counting rate data, as a function of temperature. The inset shows dependence on  $1/T$  for device B. .... 55
- Figure 4.4 Prefactor  $R_0$  for devices A, B, C, and D, extracted from dark counting rate data, as a function of temperature. Solid lines are guides to the eye. .... 56
- Figure 4.5 Dark counting rate dependence on bias current for sample B, where the solid lines are fits according to (4.9). .... 57



Figure 4.6 Fitting parameters $\Omega_{VAP}$ (left axis) and $\varepsilon(l_j)$ (right axis) from (4.9) for (a) device F and (b) device B. ....	58
Figure 4.7 Dark-count pulse amplitudes versus temperature for (a) device F and (b) device B. The solid line is a theoretical fit from (4.11), while the dotted line represents what would be a simple resistive behavior. ....	60
Figure 5.1 Hotspot model for single-photon response. ....	63
Figure 5.2 SSPD quantum efficiency as a function of bias current at different ambient temperatures. ....	65
Figure 5.3 Hotspot radius extracted from QE measurements as a function of temperature (closed circles), and $r_m$ calculated from (5.1) (red curve). ....	66
Figure 5.4 Cross-section of the SSPD nanowire, showing the hotspot generated by a single photon. The original hotspot consists of a QP core with diameter $r_m$ . Due to QP out-diffusion and electric field penetration at the normal (hotspot) boundary with the superconductor, the total hotspot diameter is now $2(r_m + L_E)$ . The supercurrent, denoted by the arrows, is now expelled from the hotspot region into the stripe edges. ....	67
Figure 5.5 Typical SSPD current-voltage characteristics at $T = 4.2$ K. ....	70
Figure 5.6 Stekly parameter $\alpha_S$ as a function of temperature. ....	71
Figure 5.7 Resistive domain propagation velocity as a function of reduced bias current, at $T = 4.2$ K. ....	72
Figure 5.8 Hotspot radius with a fit using (5.4) (black curve), with $r_m$ from (5.1) for comparison. ....	73

Figure 5.9 Quantum efficiency dependence on temperature at different reduced bias currents.....	74
Figure 5.10 Photon count rate as a function of bias current for bridges of different widths.....	76
Figure 6.1 Comparison of live oscilloscope time-domain traces for (a) traditional scheme and (b) HEMT read-out scheme, taken at similar laser intensities, such that $n \leq 1$ (HEMT is an inverting amplifier, resulting in negative pulses). Here, $n$ is the number of absorbed photons per pulse.....	79
Figure 6.2 Pulse amplitude histograms of dark counts (a), photon counts at $\lambda = 700$ nm in the single-photon regime, $n \ll 1$ (b), and multi-photon regime, $n \geq 1$ (c). All measurements performed at 4.2 K and at $I_b = 0.9 I_c$ . The SSPD output voltage amplitudes are divided by the amplifier gain.....	80
Figure 6.3 Amplitude distribution width (FWHM of Gaussian fits) for dark counts (open squares), $n \ll 1$ (closed circles), $n \leq 1$ (open triangles), and $n \geq 1$ (closed triangles). The inset shows counting rate as a function of bias current for dark counts (open squares), and $n \ll 1$ (closed circles).....	81
Figure 6.4 Comparison of (a) mean pulse amplitudes and (b) FWHM of 267 nm photons (open triangles), 720 nm photons (closed circles), 1310 nm photons (open circles), and dark counts (closed squares). .....	84
Figure 6.5 Live oscilloscope time-domain trace, showing higher pulse amplitudes of some pulses. ....	85

Figure 6.6 Pulse amplitude histograms for (a) $n \ll 1$ , $I_b = 0.7 I_c$ , (b) $n \leq 1$ , $I_b = 0.7 I_c$ , (c) $n \ll 1$ , $I_b = 0.9 I_c$ , (d) $n \leq 1$ , $I_b = 0.9 I_c$ , (e) semi-log plot of (c), (f) semi-log plot of (d) (black histograms indicate the same incident photon flux for the $n \ll$ 1 regime, red histograms indicate the same incident photon flux for the $n \leq 1$ regime). .....	87
Figure 6.7 Photon pulse amplitude distribution representing single-photon events (main peak), and possible double-photon events (secondary peak). .....	88
Figure 6.8 (a) Pulse amplitude and (b) amplitude distribution width as a function of bias current, for dark counts (black squares) and photon counts (red circles) at $\lambda$ = 800 nm. The inset in (b) shows amplitude distribution histogram at $I_b = 0.9 I_c$ . .....	90

## List of Abbreviations

1D	One-dimensional
2D	Two-dimensional
2-T	Two-temperature model
$A$	Cross sectional area
$A(T)$	Vortex energy scale
APD	Avalanche photodiode
$b$	Nonuniversal constant
BCS	Bardeen-Cooper-Shrieffer
BKT	Berezinskii-Kosterlitz-Thouless
$c_e$	Electron specific heat
$c_{ph}$	Phonon specific heat
$D$	Diffusivity
$d$	Film thickness
$e-e$	Electron-electron
$e-ph$	Electron-phonon
FET	Field-effect transistor
GL	Ginzburg-Landau
$h$	Heat transfer coefficient
$H_c$	Critical magnetic field
HEMT	High electron mobility transistor
$i$	Reduced bias current
$I_b$	Bias current
$I_c$	Critical current
$I_p$	Minimum propagation current
IR	Infra-red
$I_r$	Return current
$I_{sc}$	Scaling current
$I_{th}$	Threshold current
$IV$	Current-voltage
$J_c$	Critical current density
$J_{c0}$	Depairing current density
$K_0$	Vortex energy scale
$L$	Length
LAMH	Langer Ambegaokar McCumber and Halperin
$L_E$	Electric field penetration length
$L_h$	Thermal healing length
$L_k$	Kinetic inductance
$L_{th}$	Thermalization length
$M$	Quasiparticle multiplication
$n$	Mean absorbed photon number
NbN	Niobium nitride

NEP	Noise equivalent power
$n_f$	Free vortex density
NIR	Near infra-red
$N_0$	Electron density of states at the Fermi level
NQP	Non-equilibrium quasiparticles
$n_{qp}$	Density of non-equilibrium quasiparticles
N-S	Normal-superconducting (boundary)
PMT	Photomultiplier tube
PNR	Photon number resolution
PSC	Phase-slip centers
QE	Quantum efficiency
QKD	Quantum key distribution
QP	Quasiparticles
$R$	Resistance
$R_0$	Prefactor
$R_{AL}$	Aslamasov-Larkin resistance
$R_{dk}$	Dark-count rate
$R_{HN}$	Halperin-Nelson resistance
$R_{hs}$	Hotspot resistance
$R_L$	Load resistance
$r_m$	Hotspot radius
$R_N$	Normal state resistance
$R_{PSC}$	Resistance due to phase-slip centers
$R_s$	Sheet resistance
$RT$	Resistance-temperature
R-T	Rothwarf-Taylor
$R_{VAP}$	Resistance due to vortex-antivortex pairs
SPD	Single-photon detector
STJ	Superconducting tunnel junction
$T_0$	Bath temperature
$T_{BKT}$	Berezinskii-Kosterlitz-Thouless transition temperature
$T_c$	Critical temperature
$t_d$	Time delay
$T_e$	Electron temperature
TES	Transition-edge sensor
$T_{ph}$	Phonon temperature
$U$	Vortex-antivortex binding energy
$v$	N-S boundary velocity
VAP	Vortex-antivortex pair
$w$	Stripe width
$\alpha$	Nonlinear exponent
$\alpha_S$	Stekly parameter
$2\Delta$	Superconducting energy gap
$\Delta F$	Saddle-point energy

$\varepsilon$	
$\Phi_0$	Renormalization factor
$\lambda$	Superconducting flux quantum
$\lambda_L$	Photon wavelength
$\mu_c$	London penetration depth
$\nu$	Vortex core potential
$\rho_N$	Photon frequency
$\sigma_{th}$	Normal state resistivity
$\tau$	Thermal conductivity
$\tau_e$	Effective electron cooling time
$\tau_{e-ph}$	Inelastic electron scattering time at the Fermi surface
$\tau_{es}$	Electron-phonon interaction time
$\tau_{GL}$	Phonon escape time
$\tau_{th}$	Ginzburg-Landau relaxation time
$\Omega$	Thermalization time
$\xi$	Attempt rate
$\xi$	Ginzburg-Landau coherence length
$\zeta$	Subgap phonon losses

## **Chapter 1 Superconducting single-photon detectors**

Fast and reliable single-photon detectors (SPDs) have become a highly sought after technology in recent years. Applications for ultraviolet (UV) to infrared (IR) detection range from single-molecule fluorescence to high-resolution astronomy, linear optical quantum computing, quantum communications, and single photon metrology.

Some of the most interesting applications for SPDs, which include quantum cryptography and quantum key distribution (QKD), as well as satellite communications, require devices that can operate at telecommunications wavelengths, namely 1310 nm and 1550 nm. Silicon avalanche photodiodes (APDs) cannot operate in these regimes, as the bandgap of Si is too wide (1.1 eV) [1], while photomultiplier tube's (PMT) performance is not satisfactory for most applications. One solution is to use a semiconductor material with a narrower bandgap, such as InGaAs, for APDs. Such devices are widely used, they have, however, complicated biasing and read-out schemes, due to high dark count rates ( $\sim 10$  kHz) and large timing jitter [2],[3],[4]. Because the InGaAs fabrication technology is still immature (as compared to Si), such APDs need to be time-gated and quenched, which slows down their operational speed to a 1-MHz maximum count rate [5].

A different class of SPDs are superconducting detectors. Three main types of superconducting photon counters are available to us today. Superconducting tunnel junctions (STJs) [6],[7] and tungsten-based transition-edge sensors (TESs) [8],[9] are not only sensitive to single photons in the IR range, have low dark counts and low timing jitter, but also exhibit capability for photon-number resolution, which is highly desirable for many advanced SPD applications. The main drawback, however, is that they are quite slow, with counting rates of up to 50 kHz. Another drawback is their sub-Kelvin operation temperatures, which means they require dilution refrigerators in order to operate.

Perhaps the most promising and practical type of a superconducting detector is the NbN single-photon detector (SSPD). SSPDs are nanostructured ultrathin (4-nm thickness), submicron width (80 to 120 nm), and up to 500- $\mu\text{m}$ -long meandering NbN stripes fabricated on epitaxial-quality sapphire substrates [10],[11]. They are ultrafast photon counters with a timing jitter below 20 ps [12], moderate-to-high quantum efficiency within the wavelength range from IR to UV, very low dark counts, and operation at liquid helium temperatures. The device's operation temperature is between 2 and 4.2 K, far below the NbN critical temperature  $T_c$ , and they are biased with a dc current close to the superconducting critical current  $I_c$ . In contrast to the semiconductor counterparts, SSPDs do not need quenching circuits, nor time gating. The devices have been already successfully implemented in commercial testers for noninvasive VLSI chip debugging [13], and are very promising as



telecommunication-wavelength photon counters for both free-space (satellite) and fiber-based (network) quantum communications and QKD applications [14].

## 1.1 Fabrication and material characterization

NbN superconducting films are typically deposited on epitaxially flat *R*-plane sapphire substrates via dc reactive magnetron sputtering in Ar and N<sub>2</sub> mixture and are characterized by the room temperature sheet resistance of about 250  $\Omega$ /square to 500  $\Omega$ /square,  $T_c \approx 11$  K, and critical current density  $J_c = 6$  to 7 MA/cm<sup>2</sup> at  $T = 4.2$  K. During the NbN deposition process the substrate is heated up to 900 K, leading to an epitaxial growth of the film. The most recent detectors, shown in Fig. 1.1, have a meander-type geometry that covers a  $10 \times 10 \mu\text{m}^2$  area and has a filling factor (ratio of the area occupied by the superconducting meander to the device nominal area) up to 0.5. The width of the superconducting stripe is typically 80 to 120 nm, with 4 nm thickness.

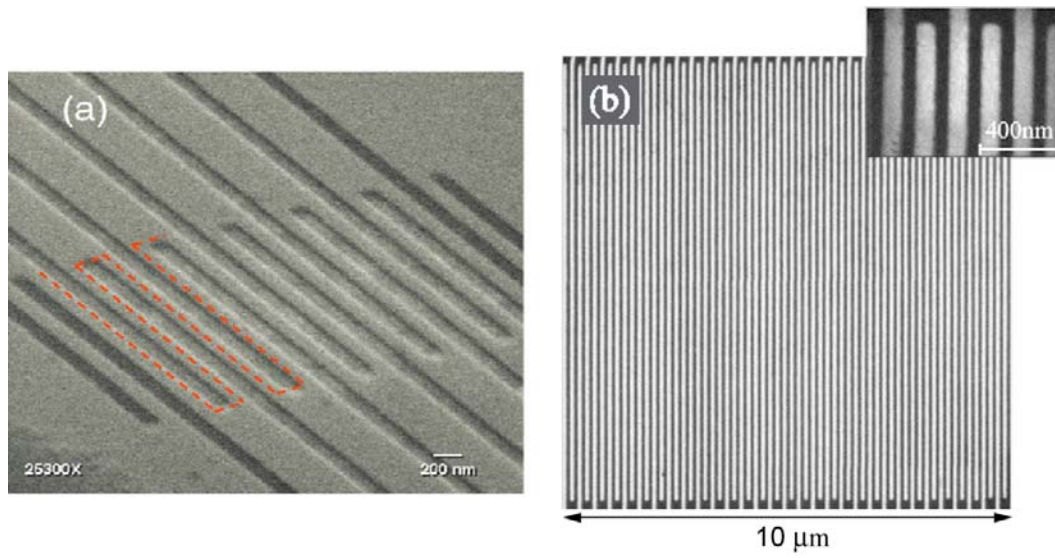


**Figure 1.1 SEM images of SSPDs. (a) One of the older devices with 150 nm stripe width, the red dotted line shows the meander structure. (b) A latest device with  $10 \times 10 \mu\text{m}^2$  active area and 120 nm stripe width, NbN here is black.**

Figure 1.2 presents a typical dependence of the sheet resistance on temperature for a meander-like 4-nm thick SSPD, measured in the temperature range between 4.2 and 300 K, with a bias current of 500 nA (small fraction of the critical current at  $T = 4.2$  K), to insure minimal Joule heating. The sheet resistance increased with temperature decrease, which indicates that the NbN film may be under some stress given by a lattice mismatch with the sapphire substrate. The overall low sheet resistance values indicate that the NbN film is structurally homogeneous.

Figure 1.3 shows the comparison between the superconducting transition of a plain NbN film and a patterned meander. In both cases, the superconducting transition width is practically the same, confirming that meander patterning does not degrade superconducting properties of our devices.

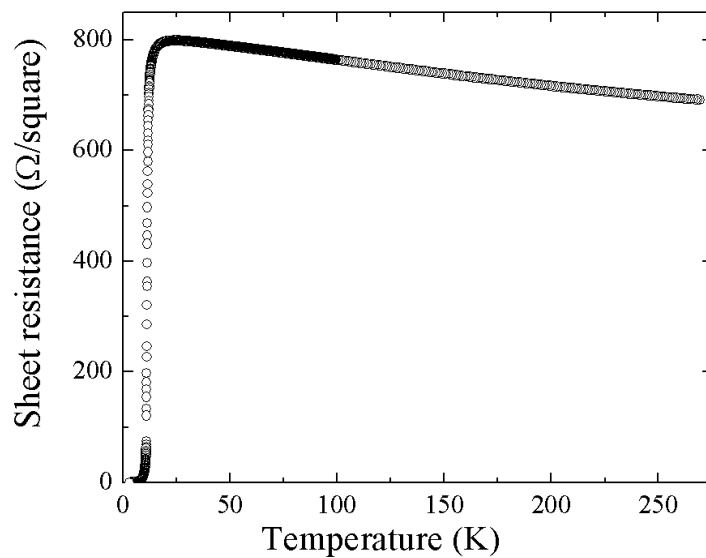


Figure 1.2 Sheet resistance dependence on temperature for a typical SSPD.

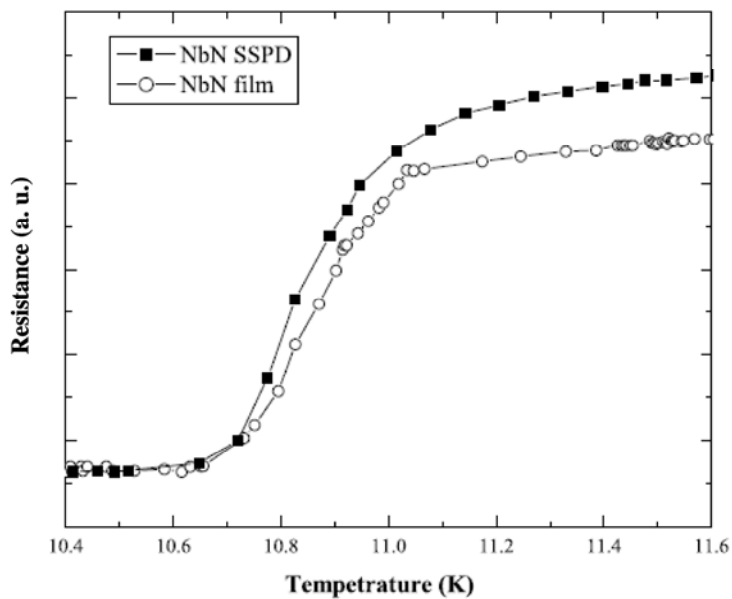


Figure 1.3 Comparison of resistance dependence on temperature for a NbN film, and a typical SSPD.

Figure 1.4 shows schematically the SSPD fabrication process, where the devices are patterned using direct e-beam lithography and subsequent selective ion etching [15]. Here, the areas under which the superconducting film is removed are exposed in the resist during electron beam lithography. The minimal width of the stripe is largely determined by scattering in the photoresist and does not depend directly on the electron beam diameter. An 80-nm thick layer of resist PMMA 950 K is later removed from the superconductor using reactive ion etching. This process results in a narrow meander stripe with uniform edges and a high yield of good devices.

Early devices, and later NbN nanobridge structures used in our dark count studies, were patterned by lift-off electron-beam lithography and ion milling, as shown in detail in Fig. 1.5. Here, a Ti mask is deposited and patterned where the nanobridges will eventually be, and the ion beam milling of the unprotected NbN film, and chemical etching of the Ti mask are required. This latter technological process has its limitations, among them the most important are unavoidable electron illumination of unexposed photoresist areas and the need for a consistent lift-off process, which results in somewhat nonuniform edges of nanobridges; thus, it was discontinued for fabrication of meanders, but worked fine for the simple, single-bridge structures[16]. The SSPD/nanobridge fabrication of almost all studied devices in this thesis was performed in the group of Professor G. N. Golt'sman at the Moscow

State Pedagogical University in Moscow, Russia. Many such devices were actually fabricated during my two, two-months visits to Moscow.

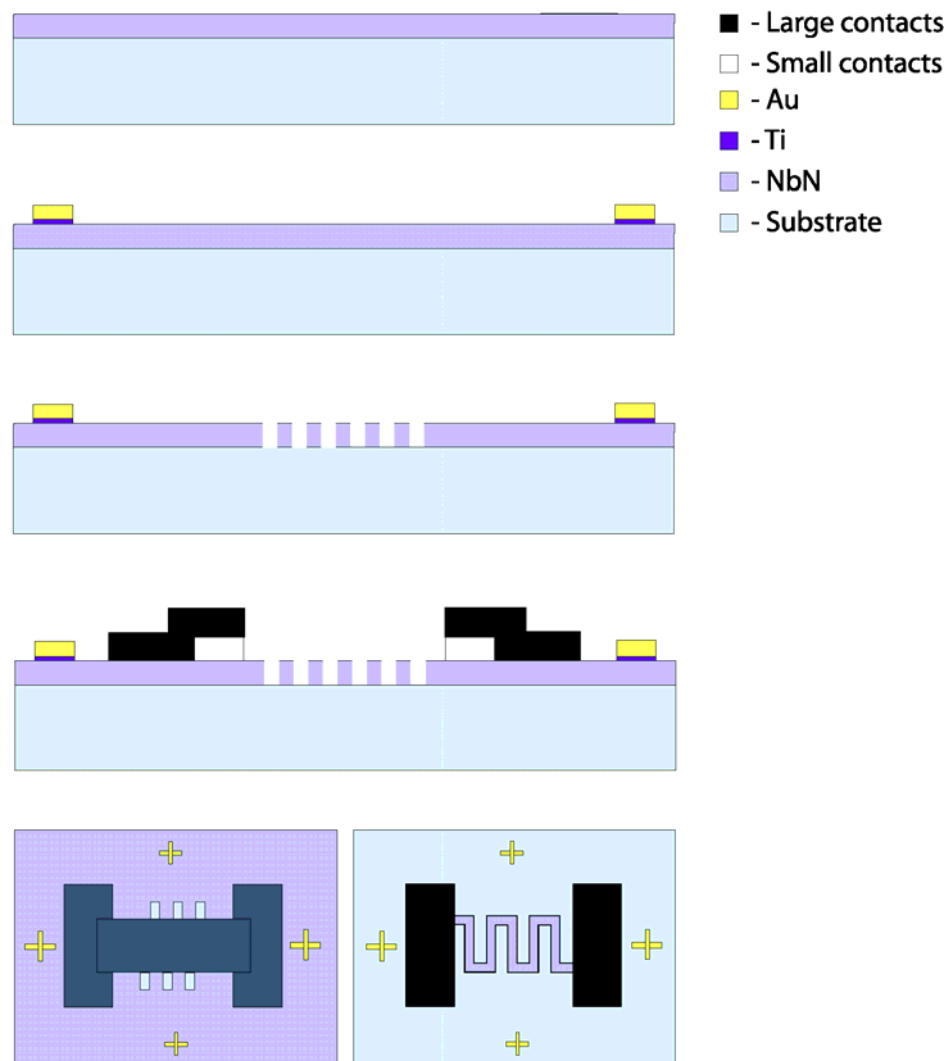
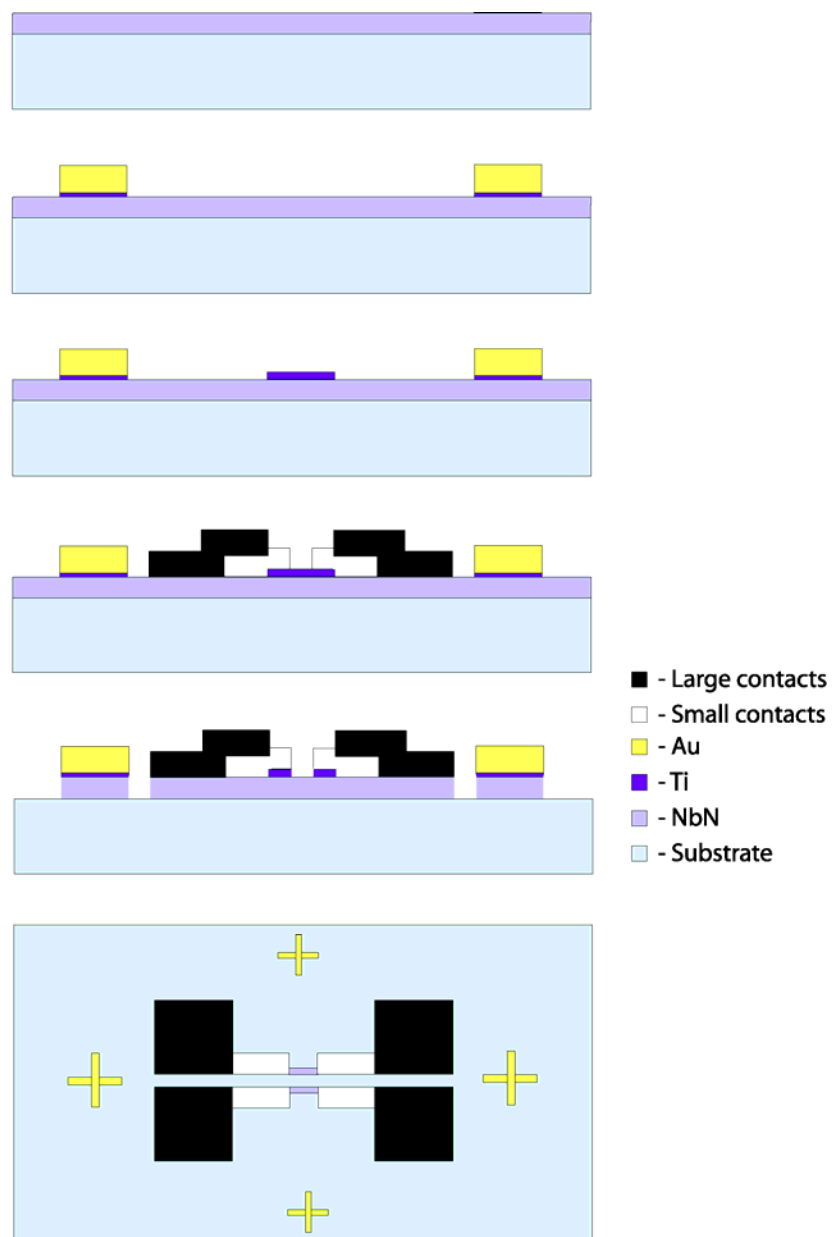


Figure 1.4 SSPD fabrication process, direct e-beam lithography.



**Figure 1.5 Nanobridge fabrication process, lift-off e-beam lithography. There are two bridges, completely isolated from each other, on each chip.**

## 1.2 Photoresponse mechanisms in superconductors

Before discussing experimental results of our nanowire detectors, we first need to understand the photoresponse processes in superconductors. Two main types are nonequilibrium hot-electron effect and equilibrium thermal heating [17]. As the nonequilibrium photoresponse is the process under which the SSPD operates, here, I will only focus on this mechanism.

During the nonequilibrium process, there is a heating of electron and phonon subsystems in a superconductor, after absorption of a photon. The radiation thermalizes first within the electron subsystem via electron-electron ( $e-e$ ) interaction, which causes the temperature of the electron subsystem  $T_e$  to increase with a specific heat  $C_e$ . Next, the electrons relax by interacting with phonons via electron-phonon ( $e-ph$ ) interaction, after which the temperature of the phonon subsystem  $T_{ph}$  also rises, with a specific heat  $C_{ph}$ . Some of the phonons can give the energy back to the electron subsystem through  $ph-e$  interaction, and eventually all the phonons escape to the substrate and the system returns to equilibrium. The above process can be described very well by a two-temperature (2-T) model, as illustrated in Fig. 1.6 and described by [18],[19]. Strictly speaking, the 2-T model is applicable for normal metals, and superconducting materials at temperatures near the superconducting  $T_c$ . It can be, however, quite successfully extended to devices operating far below  $T_c$ , as long as the optical perturbation is very weak (as, *e.g.*, in our single-photon case).



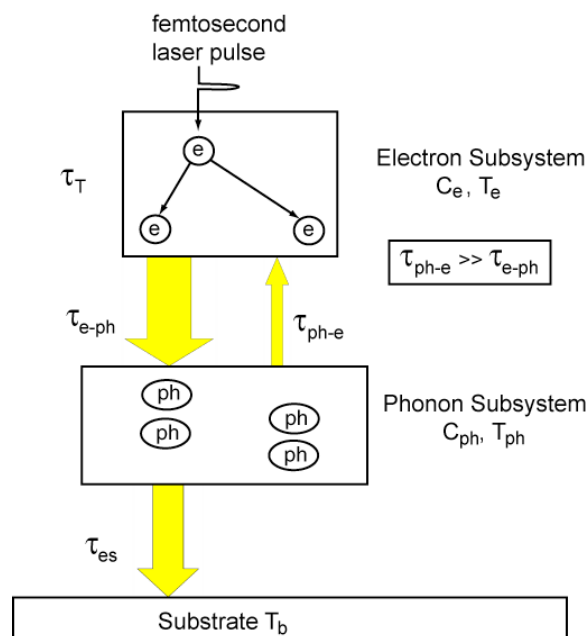


**Figure 1.6 Two-temperature model.** After photoabsorption, electrons thermalize on a  $\tau_T$  time scale. The energy from the electron subsystem is then transferred to the phonon subsystem with a time  $\tau_{e-ph}$ . Some of the phonons give the energy back to the electron subsystem with time  $\tau_{ph-e}$  and the phonon escape time into the substrate is given by  $\tau_{es}$ .

For  $T \ll T_c$ , and/or under moderate to intense illumination, the nonequilibrium photoresponse of superconductors has to be described by the Rothwarf-Taylor (R-T) model [20], which deals with the changes in the quasiparticle and phonon densities and is schematically illustrated in Fig. 1.7. Here, a Cooper pair is broken upon absorption of a photon, into a highly excited hot electron and a low energy quasiparticle. The hot electron relaxes while breaking more Cooper pairs via  $e-e$  and  $e$ -optical- $ph$  interactions. The high energy phonons generated during this thermalization process have enough energy to break more Cooper pairs, generating more electrons, which eventually relax back into low energy states just above the superconducting energy gap  $2\Delta$ , and recombine into Cooper pairs with recombination

time  $\tau_R$ . Phonons emitted during the quasiparticle recombination process have, however, the energy equal to at least  $2\Delta$ , so they can break Cooper pairs as well, which occurs on a timescale  $\tau_B$ . The above processes continue simultaneously, until, eventually, all the phonons escape into the substrate with the escape time  $\tau_{es}$ . The R-T dynamics are nonlinear, as the Cooper-pair recombination with emission of a phonon and phonon-induced pair breaking processes are coupled together. However, for weak optical perturbation, the R-T equations can be linearized, and become formally identical to the 2-T model.

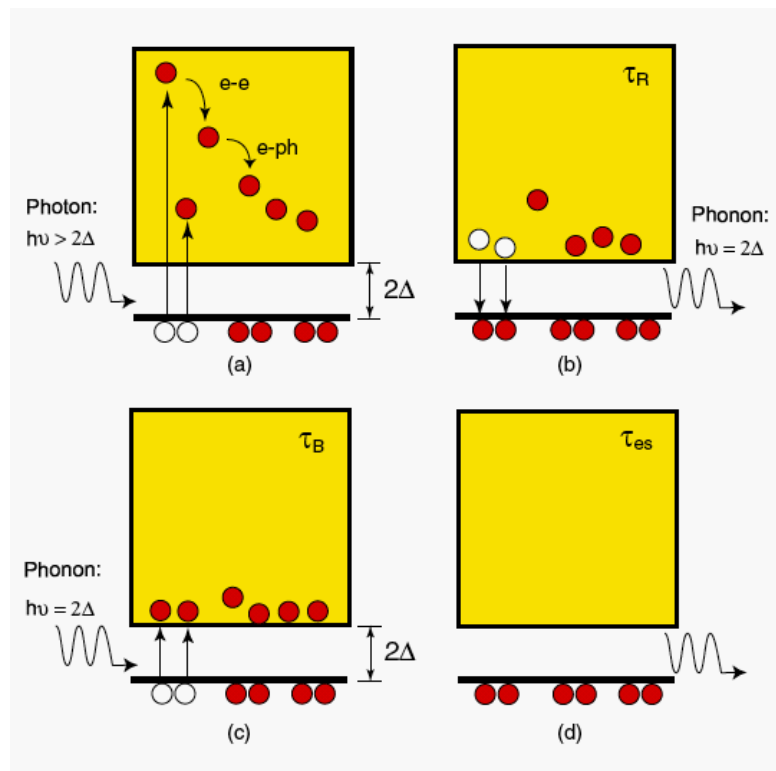


**Figure 1.7** Rothwarf-Taylor model, (a) a photon breaks a Cooper pair to create a highly-excited quasiparticle, which breaks other Cooper pairs via electron-electron and electron-phonon interactions. (b) Quasiparticles begin to recombine and emit acoustic phonons with energy  $2\Delta$ . (c)  $2\Delta$ -phonons have enough energy to break other Cooper pairs. (d) Phonons escape to the substrate.

### 1.3 Electrical model and device performance

In spatial terms, the SSPD photoresponse model can be described by hotspot formation. Following, *e.g.*, the 2-T model, the intensity of cascade multiplication and thermalization [21] of nonequilibrium quasiparticles (NQPs) is defined by the *e-e* and *e-ph* interactions, with characteristic relaxation times  $\tau_{e-e}$  and  $\tau_{e-ph}$ , respectively [22]. Once the concentration of NQPs in the site of photon absorption reaches the normal-state limit, a resistive hotspot appears in the superconducting film. An increase in concentration of NQPs leads to their diffusion out of the photon absorption area with a characteristic diffusion coefficient  $D$ , which depends on the mobility of NQPs and homogeneity of the superconducting film. If the film is electrically two-dimensional, *i.e.*, the film thickness is  $d < L_{th} = (D\tau_{th})^{1/2}$ , where  $\tau_{th}$  is the NQP thermalization time,  $L_{th}$  is the electron thermalization length, the hotspot forms a cylindrical slab containing  $n = N_o\Delta$  number of uniformly distributed NQPs. Here,  $N_o$  is the electron density of states at the Fermi level. Using experimentally measured values,  $D = 0.45 \text{ cm}^2/\text{s}$  [21] and  $\tau_{th} = 6.5 \text{ ps}$  [22], we calculate  $L_{th} = 17 \text{ nm}$ .

In macroscopic samples, photon perturbation and subsequent hotspot formation have a negligible impact on the superconducting state. However, if we have a nanowire with transverse dimensions comparable with the hotspot diameter, such that in our SSPDs, a photodetection process can take place. The hotspot region, due to quasiparticle diffusion, will eventually form across the entire width and thickness of the stripe, and in turn give rise to a transient voltage signal.

It is important to mention that the detector's temporal response, or counting rate, is limited by the large kinetic inductance  $L_k$  of the SSPD structures [23]. Kinetic inductance is the magnetic energy stored in the motion of charge carriers, and in thin superconducting films, it far exceeds the regular geometric inductance. A typical voltage pulse corresponding to the photon detection, along with an equivalent electrical model of the SSPD photoresponse, are shown in Figs. 1.8(a) and 1.8(b), respectively. The  $L_k$  element is in series with a parallel arrangement of a hotspot resistance  $R_{hs}$  and a switch  $S$  represents the photodetection (switching) event in the SSPD. The detector is then connected to a dc bias source and a read-out circuit, which consists in this case of a transmission line and amplifier with input impedance  $Z_o = 50 \Omega$ . In the simulations, which will be presented later, a band-pass filter representing the amplifier bandwidth is added. Finally,  $V_{out}$  is the experimentally observed transient voltage pulse during photodetection.

Initially, the switch is closed, and there is no voltage drop. Once a photon is absorbed by the nanostripe and the resistive state is formed, the switch opens, and as  $R_{hs}$  grows to a value much larger than  $Z_o$ , most of the current redistributes into  $Z_o$ , and the resultant voltage pulse amplitude is simply  $V_{out} \approx I_b Z_o$ . Then, the rise-time constant  $V_{out}$  is  $\tau_{rise} = L_k / (R_{hs} + Z_o)$  [23]. After the current through the device drops to a sufficiently low value, the cooling mechanisms can take over, the switch closes, and the fall-time constant of the pulse is now  $\tau_{fall} = L_k / Z_o$ . In a typical, large-mander SSPD,  $L_k$  is on the order of 500 nH, and if  $Z_o = 50 \Omega$ , then  $\tau_{fall} = 10$  ns, which makes

SSPDs still significantly faster than the other superconducting and semiconducting detectors.

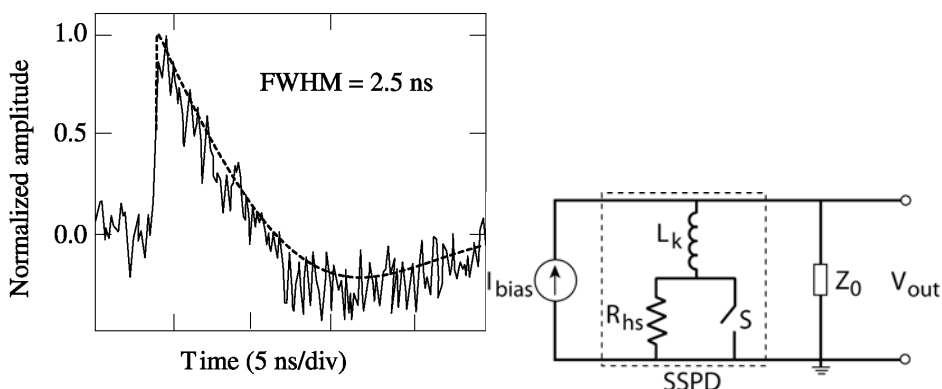


**Figure 1.8** (a) Transient voltage pulse corresponding to a single-photon event (black line), a simulated photoresponse (dashed line). (b) Equivalent electrical model of the photoresponse mechanism [23].

When operated at  $T = 4.2$  K, SSPDs typically demonstrate quantum efficiencies (QEs) up to 20% for the visible light photons (up to 800 nm), and up to 10% in the near-IR (NIR). Table 1.1 compares performance of semiconducting APDs with superconducting SPDs. Decreasing the temperature down to 2 K improves the SSPD operation significantly, given by lower dark counts and higher QEs: up to 30% in the visible range, which is the limit given by the optical absorption of NbN films. Recently, we have observed a QE of  $\sim 30\%$  at a telecommunication wavelength of 1.3  $\mu\text{m}$  for their best large-area ( $10 \times 10 \mu\text{m}^2$ ) detector, with a dark count rate below  $2 \times 10^{-4}$  Hz, and photon counting rate up to 250 MHz [24]. The latter counting rate was limited by the large  $L_k$  values, but we should note here that the earlier, small active area SSPDs demonstrated count rates up to 1 GHz [16]. Nevertheless, we typically

choose to work with the large-area devices, as they provide higher detection efficiencies (DE) due to low losses in the system (large active area provides better photon coupling).

In 2006, Rosfjord *et al.* [25] achieved DE efficiencies up to 57% at a telecommunication wavelength of 1.55  $\mu\text{m}$  (67% at 1.064  $\mu\text{m}$ ), by integrating a quarter-wavelength cavity on top of the detector, and anti-reflection coating at the bottom of the substrate, in order to trap photons and subsequently increase the effective QE.

**Table 1.1 Comparison of single-photon detectors**

Detectors	Si APDs	InGaAs APDs	TES SPD	STJ SPD	SSPD
Temperature (K)	300	200	0.1	0.4	2 – 4.2
Wavelength ( $\mu\text{m}$ )	0.4 – 1.1	0.9 – 1.7	0.1 – 5	0.2 – 1	0.3 – 5.6
Time resolution	300 ps	300 ps	300 ns	< 2 ns	18 ps
Quantum efficiency	70% @ 630 nm	25% @ 1.55 $\mu\text{m}$	92% @ 1.55 $\mu\text{m}$	50% @ 500 nm	10% @ 1.55 $\mu\text{m}$
Dark count rate (Hz)	< 25	< $10^4$	< $10^3$	N/A	< 0.01
Maximum count rate	10 MHz	1 MHz	20 kHz	50 kHz	250 MHz
Photon number resolution	Very limited	No	Yes	Yes	In progress

Quite recently, a QKD system using a 200 km fiber link has been demonstrated and tested with a twin SSPD setup at 1.55  $\mu\text{m}$  [26]. In addition, various single-photon sources (quantum dots and quantum wells emitting at different wavelengths) have been characterized using twin SSPDs [27],[28]. Also experimentally demonstrated are heralding of telecommunication photon pairs [29], and a 781 Mbit/s photon-counting optical communication [30] in a combined APD and SSPD system.

## 1.4 Thesis motivation

When the detector is completely blocked from all incoming radiation (shielded by a metallic enclosure), one can observe sporadic voltage pulses, identical in their temporal shape to the actual photon counting events, as shown in Fig. 1.9. Those events are purely spontaneous and they constitute the device dark counts. The dark counts directly affect any detector performance, as they determine its noise equivalent power (NEP), which in turn defines the sensitivity. For quantum detectors, the NEP is given by [31]

$$NEP = \frac{h\nu}{QE} \sqrt{2R_{dk}}, \quad (1.1)$$

where  $h\nu$  is the photon energy, and  $R_{dk}$  is the dark counting rate.

Figures 1.10(a) and 1.10(b) show typical dependences of QE and  $R_{dk}$  on the bias current  $I_b$ , respectively, recorded in our laboratory [32],[33]. Both increase near-exponentially with  $I_b$ , so when it comes to the sensitivity of the device, there will always be a trade-off between QE and  $R_{dk}$ , as shown by (1.1). The dark counts are, of course, an undesired phenomenon, and their full understanding in the context of the photodetection mechanism is the main topic of this thesis. From this practical point of view, minimization of dark counts will lead to improvements of the overall performance of SSPDs, as well as to a better understanding of their intrinsic performance and photodetection mechanism.

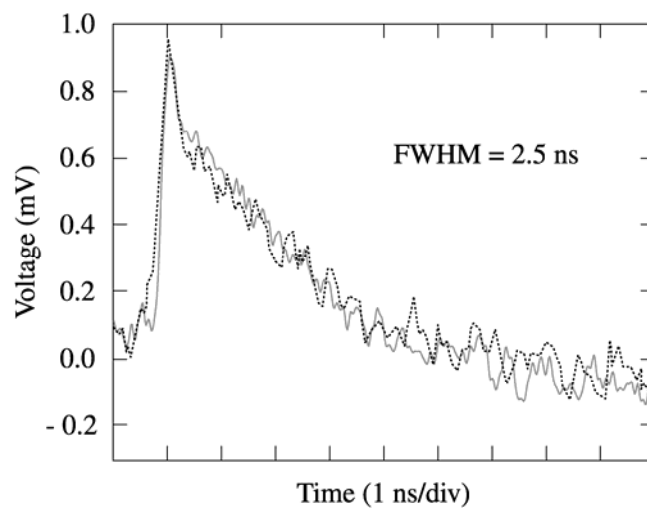


Figure 1.9 Comparison of dark-count event (dotted line) with a photon-count event (gray line).

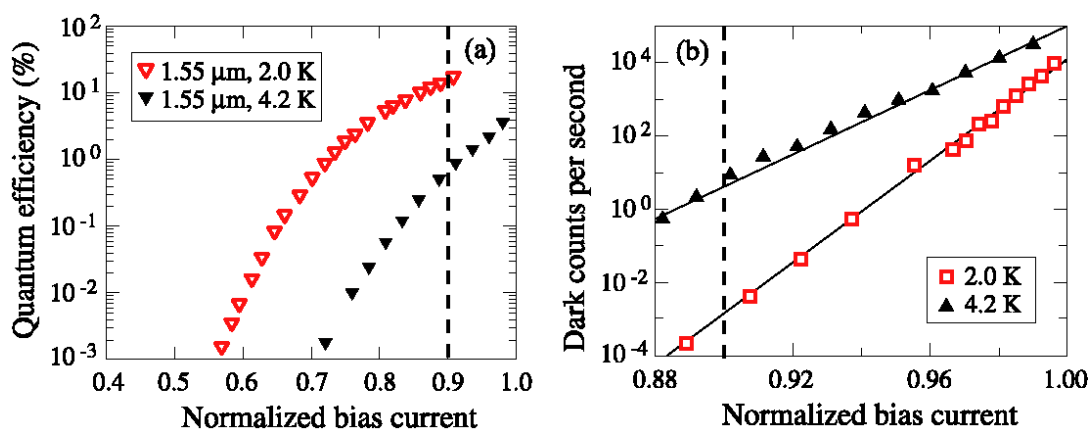


Figure 1.10 (a) Typical QE dependence on bias current and (b) dark counting rate dependence on bias current at temperatures 2.0 K (red symbols) and 4.2 K (black symbols). The dashed lines indicate typical operation point,  $I_b/I_c = 0.9$ .



## 1.5 Outline of the thesis

In Chapter 2, experimental methods, including both testing set-ups and procedures, are described in detail. In Chapter 3, I introduce dissipation mechanisms in one-dimensional and two-dimensional superconductors, which are the foundation for our dark count studies, and even give us clues into the NbN SSPD intrinsic operation, which is missing in the standard hotspot model. In Chapter 4, I report on my experimental studies of dark counts in NbN SSPDs as well as in superconducting NbN nanobridges. The latter structures were additionally fabricated in order to help us to gain a better insight into the physics of dark counts, by performing experiments on the simple, single-stripe structures. Chapter 5 investigates the photodetection mechanism as the dynamic hotspot process, along with the fluctuation-enhanced photodetection approach. In Chapter 6, I discuss how photon-number resolution (PNR) capability may be achievable with our devices using read-out electronics and a cryogenic low-noise amplifier. Finally, Chapter 7 summarizes and concludes my work.

## Chapter 2 Experimental methods

### 2.1 Dark counts

For dark count measurements, we decided to fabricate simple NbN nanobridge structures of different widths and lengths, along with the standard SSPDs. The NbN nanobridges have much lower  $L_k$  values as compared with SSPDs, which makes them better candidates for dark count studies. An SEM image of a chip containing two separate nanobridges is shown in Fig. 2.1.

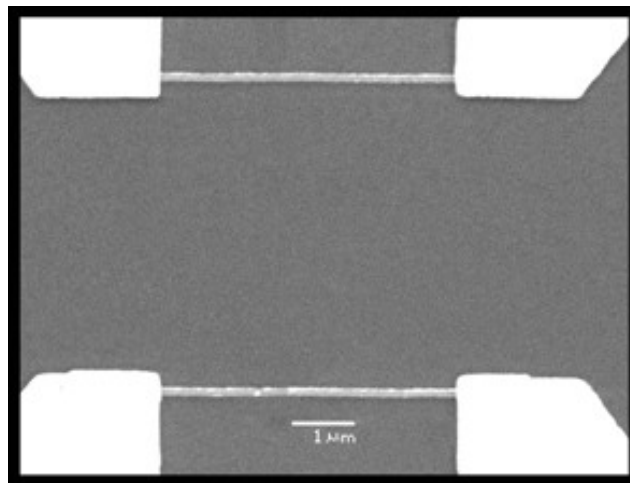


**Figure 2.1** SEM image of two nanobridge structures on the same chip.

The experimental setup for  $R_{dk}$  measurements is shown in Fig. 2.2, where the device is surrounded by a metallic enclosure and placed inside a variable-temperature cryostat. The structures were wire bonded to a microstrip transmission line, which in

turn was attached to a standard semirigid coaxial cable, and on the other end connected to a room-temperature bias-tee (bandwidth 0.08 – 26 GHz). The bias-tee allowed to simultaneously amplify the signal using a tandem of two broadband amplifiers (bandwidth 0.08 – 8.5 GHz; gain 22 dB), and bias it by a stable low noise dc voltage source, in series with a 50 k $\Omega$  resistor. The amplified dark counts were recorded either on a Tektronix TDS 6604 6-GHz digital single-shot oscilloscope, or using a photon counter. The measurements were performed in superfluid helium at temperatures between 1.5 K and 2.17 K, liquid helium at temperatures between 2.18 K and 4.2 K, and helium vapor between 4.2 K and 8 K. The sample chamber was surrounded by a metallic enclosure and a  $\mu$ -metal shield, to prevent outside radiation from coming into contact with the device, and to minimize the Earth's magnetic field surrounding the device.

Some of the dark counting rate measurements, which I will present in Chapter 4, were performed inside an adiabatic refrigerator, at temperatures from 100 mK to 5.5 K, where the devices were in vacuum. The room temperature electronics were the same, and we did not observe any difference in the data taken for devices immersed in helium versus devices measured in vacuum. The sub-Kelvin measurements were performed together with Dr. Sae Woo Nam at the National Institute of Standards and Technology in Boulder, Colorado.

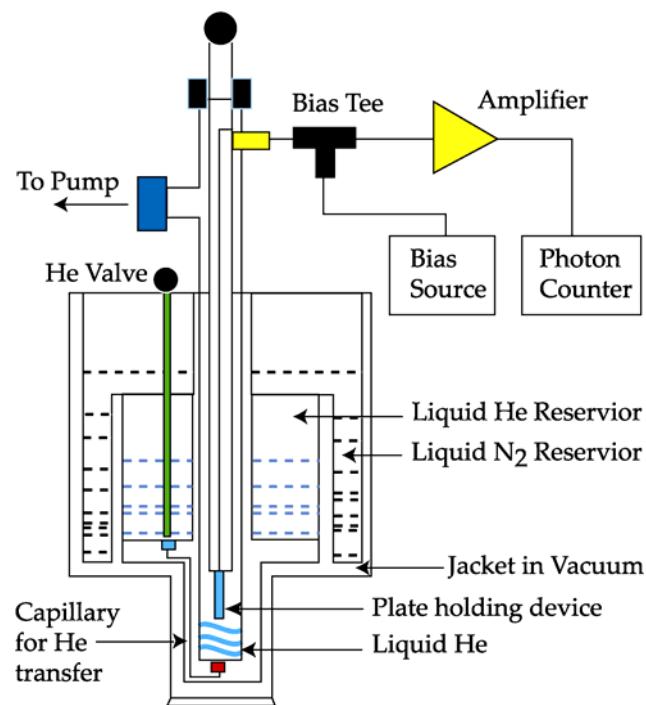


**Figure 2.2** Experimental setup for dark count measurements.

Current-voltage ( $IV$ ) characteristics for dissipation measurements near  $T_c$  were taken by sweeping a current from the Keithley 220 current source through a device, and reading out voltage across a device. The samples were once again placed inside a variable temperature cryostat, and surrounded by metallic enclosure and a  $\mu$ -metal shield. This time, they were directly connected to a current source and a voltmeter.

For resistance versus temperature ( $RT$ ) measurements at low currents (between 100 nA and 1  $\mu$ A), a lock-in amplifier was utilized to minimize the noise in the measured voltage. A 26.1-Hz voltage oscillator connected in series with a 100 k $\Omega$  resistor comprised the current source, and a lock-in amplifier were used to measure

the voltage drop across the device. A schematic diagram of this experiment is shown in Fig. 2.3.

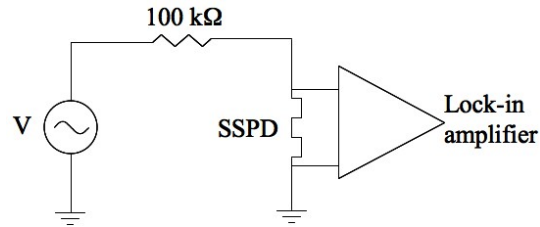


**Figure 2.3** Low-bias resistance measurement schematic. The current source is the 26.1 Hz voltage oscillator in series with a 100 kΩ resistor. The lock-in amplifier reads out the voltage across the SSPD.

## 2.2 Photon counts and quantum efficiency

A fiber-based setup was used for the QE dependence on temperature measurements. A photon beam was aligned with the optical fiber, and the fiber was in turn aligned with the SSPD. A Ti:Sapphire laser, with the beam heavily attenuated by neutral density filters, and tunable between 700 nm and 1000 nm wavelengths, was used as a single-photon source. When mode-locked, 100-fs-wide laser pulses came at a repetition rate of 78 MHz. Electrically the detector was connected at room temperature to the same instruments as for the dark count measurements: a bias tee, a low-noise dc voltage source in series with a 50 kΩ resistor, and a 300-MHz pulse counter. The schematic in Fig. 2.4 shows a typical fiber-based measurement setup.

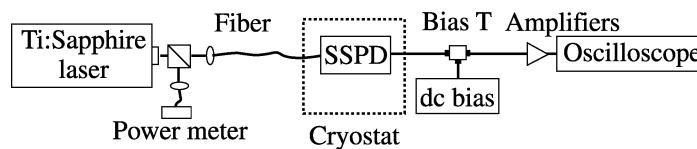


**Figure 2.4 Fiber-based experimental setup**

### 2.3 HEMT-amplifier-based detection setup

We have already established that after photon absorption, a resistive hotspot region is formed, and this resistance is estimated to be on the order of several hundred ohms, depending on operating conditions. In this case, after the hotspot formation, most of the current switches to the load impedance, in our case  $50 \Omega$  load line (characteristic impedance of the coaxial line and the amplifiers), and the amplitude of the observed response is simply given by Ohm's law,  $V_{pulse} \approx G \times I_b \times 50 \Omega$ , where  $G$  is the amplifier gain.

For dark-count pulse amplitudes and PNR measurements, which should in principle allow us to resolve pulse amplitudes, *e.g.*, corresponding to the number of absorbed photons, a high electron mobility transistor (HEMT) amplifier was mounted next to the SSPD [34]. This setup was designed and implemented at Delft University of Technology in Delft, The Netherlands, and experiments were performed during my six-months visit there. Because the HEMT impedance is nearly infinite, we utilized a  $500\text{-}\Omega$  load resistor  $R_L$  in parallel with the detector and the HEMT, to ensure that the current redistributes differently through the sample. A HEMT is a heterostructure field-effect transistor (FET), with a heterojunction as the channel instead of a doped

region. The heterojunction creates a thin layer of very mobile electrons with a high concentration, and this layer is called a two-dimensional electron gas. Because HEMT pinch-off voltage is negative, it is always on, even when the SSPD is superconducting and the gate voltage is zero, and it operates in the linear (amplifier) region. As the SSPD resistance grows, the gate voltage increases, and the current through the channel increases linearly with it. Thus, the conductivity in the channel is altered, and we can read out a voltage pulse. Then, this voltage will ideally be directly proportional to the hotspot resistance, and if a number of photons are absorbed in the SSPD, forming separate hotspots in a long meander, these hotspot resistances will add up in series. Thus, the number of photons absorbed will be proportional to the pulse height.

A schematic of such a circuit is shown in Fig. 2.5, together with a picture of the cold head shown in the inset. The SSPD is mounted on a printed circuit board and wire-bonded, with the HEMT and  $R_L$  mounted on the same board, all electrically connected to a SMA jack. The SMA connects to a  $50 \Omega$  coaxial cable, which allows to both bias the devices, and read out the ac voltage signal which constitutes photon counts.

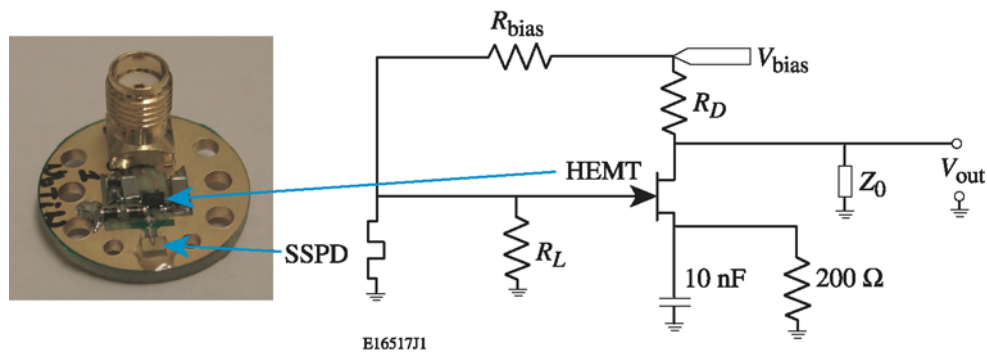


**Figure 2.5** Circuit schematics implementing HEMT amplifier and a 500- $\Omega$  load resistor,  $R_L$ . The 10 nF capacitor sets the maximum AC gain and 200- $\Omega$  resistor sets the DC current for the HEMT;  $R_{bias}$  and  $R_D$  are the biasing and pull-up resistors, respectively. The inset shows the actual physical layout.

## 2.4 PSpice simulations and circuit limitations

In order to understand the electrical photoresponse of our SSPDs and decide on the operating parameters of the read-out circuit, we have performed extensive PSpice simulations using a commercial PSpice program. The above approach was especially important in the case of HEMT-based read-out, since the amplifier was directly (in helium) integrated with the SSPD. Already the first PSpice simulations reveal that  $R_L$  values higher than  $\sim 270 \Omega$  lead to an underdamped circuit. The reason is that, as shown in Fig. 2.5, there is a large inductor ( $\sim 500$  nH  $L_k$  of the SSPD) in parallel with  $R_L$ . In addition, there is also always in our read-out circuit a small parasitic capacitance, coming from a circuit board, as well as other components, estimated to be around 2 to 3 pF. Figure 2.6(a) shows the PSpice simulated pulses for different values of  $R_L$ , and based on this figure, we chose the value of  $R_L$  to be 500  $\Omega$



[green line in Fig. 2.6(a)], even though we suspect that this value might be lower than the hotspot resistance, however, the underdamping for higher  $R_L$ 's is too large, and would limit the detector's counting rate. Figure 2.6(b) shows the experimental (black line), as well as simulated (red line) voltage pulses for our HEMT read-out approach. The broader, more damped oscillation behind the measured main pulse is likely due to some second order effects from the amplifier and/or stainless steel coaxial line. For the device used here,  $I_c = 5.5 \mu\text{A}$  at  $T = 4.2 \text{ K}$ , and the fit from the simulation yields  $R_{hs} \sim 1.2 \text{ k}\Omega$ .

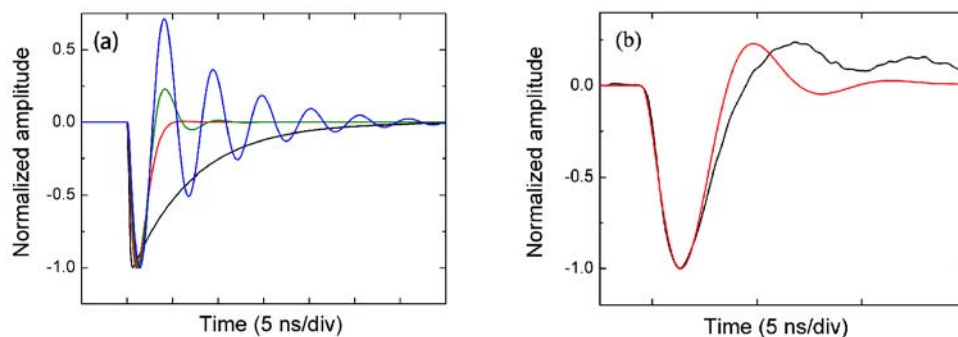


**Figure 2.6** PSpice simulations of voltage transients at different values of  $R_L$ : 50  $\Omega$  (black curve), 270  $\Omega$  (red curve), 500  $\Omega$  (green curve), and 2 k $\Omega$  (blue curve); and (b) measured photoresponse (black curve) and simulated photoresponse (red curve), for  $R_L = 500 \Omega$ .

As increasing  $R_L$  leads to further underdamping [Fig. 2.6(a)], more underdamping leads to latching of SSPDs. In other words, when the circuit is not damped enough, once the detector absorbs a photon, the entire stripe eventually switches to the resistive state, and it will not become superconducting again quickly unless the dc current source is switched off. This can be seen in Fig. 2.7, which

shows an experimentally observed latching event (black curve) compared with a standard photodetection event (red curve) in the HEMT circuit. The rise-time constant in the latched pulse is now just the relaxation time of the HEMT. This limits the performance of our devices implemented into the HEMT setup, and also limits the value of  $R_L$ .

For a given  $R_L$ , so long as the circuit is underdamped, the frequency of latching events increases with the bias current. This is illustrated in Fig. 2.8, and can be explained in the following way. When we monitor the current through the device after photon absorption, it initially drops to a value  $I_b \leq 0.2I_c$ , which allowed for cooling mechanisms to take over. When the circuit is underdamped, the actual current through the device will oscillate and, at some point, will even overshoot the  $I_b$  value. Because we already bias the devices close to  $I_c$ , if  $I_b$  is high enough, the current through the device at the point of overshoot is likely to overshoot  $I_c$ , leading the entire device to go into global resistive state. After that, the current never drops to a low enough value in order for superconductivity to be restored quickly, as we need to wait until the device cools back down to the operating temperature.

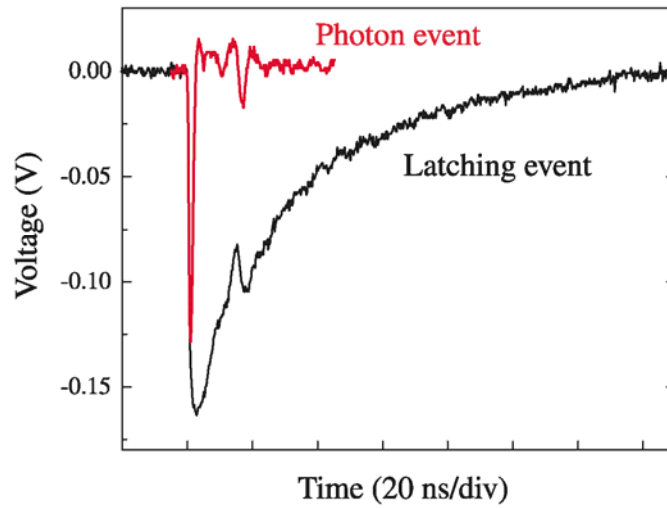


Figure 2.7 Comparison of a latching event (black curve), where the pulse rise-time is simply the relaxation time of the HEMT, and a typical photodetection event (red curve).

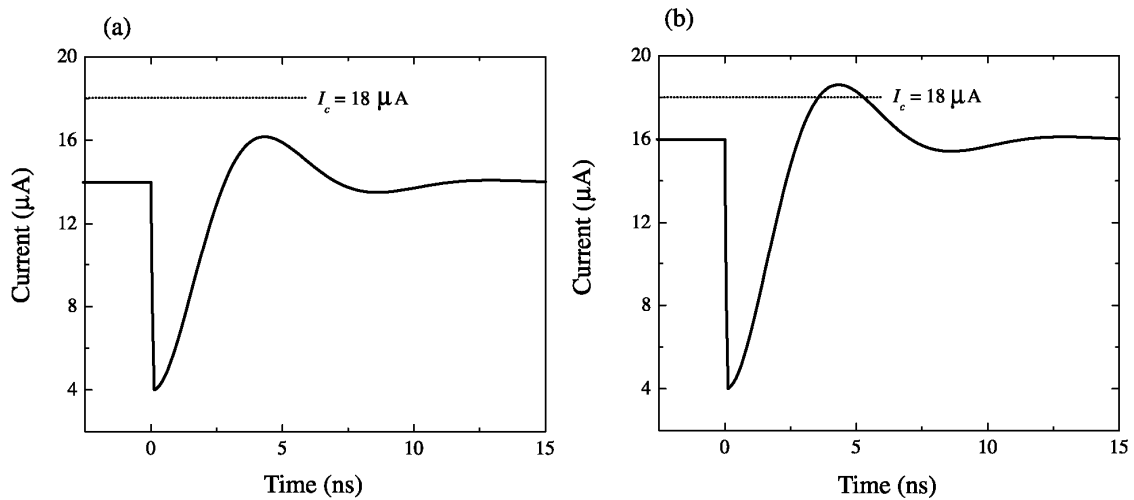


Figure 2.8 Current flowing through the SSPD at the time of a photodetection event,  $t = 0$ . In (b),  $I_b$  overshoots  $I_c$  at  $t = 5$  ns, leading the device to latch. Here,  $I_c = 18 \mu\text{A}$ .

If we consider the electrical model only, the difference in amplitude, for different hotspot resistances, stems from the time it takes for the current flowing through the meander to drop and redistribute into the read-out circuit. In other words, for a given  $R_{hs}$ , current redistribution time increases with  $R_L$ . We know that for the hotspot to stop growing and cooling mechanisms to take over, the current through the device must drop to a certain value  $I_r \ll I_c$  [35]. The higher the load resistance, the longer it takes for that to happen. This works against us because, for a given  $R_L$ , the redistribution time for two hotspots will occur faster than that for a single hotspot, making the amplitude of the two comparable. All of this we observed from PSpice simulations.

If we assume that the switch in the SSPD electrical model opens at  $t = 0$  (a photon is absorbed), and it develops an instantaneous hotspot resistance  $R_{hs}$ , the current will redistribute into  $R_L$  with a time constant  $\tau_{fall,1} = L_k / (R_L + R_{hs})$  [23]. When there are two hotspots,  $\tau_{fall,2} = L_k / (R_L + 2R_{hs})$ . Let us assume the switch closes as soon as the current drops to a value  $I_r$ , which happens twice as fast when there are two hotspots, as opposed to one. This is illustrated in Fig. 2.9(a), which monitors the current drop through the SSPD. The switch closes at  $t_1$  and  $t_2$  for a single and a double hotspot, respectively. Figure 2.9(b) shows the resultant voltage pulses for the model above. One can see that in this case, both pulses have the same amplitude, and only slightly different rise times.

Assuming, however, that  $R_{hs} = 1.2 \text{ k}\Omega$ , then PNR will only work if the time the switch closes, and superconductivity is restored, is independent of  $R_{hs}$ . A

simulation of this is shown in Fig. 2.9(c), where a single hotspot occurs at  $t = 0$ , and two simultaneous hotspots occur at  $t = 15$  ns. Here, the amplitude of the double hotspot is  $\sim 1.5$  times larger than that of a single hotspot.

Finally, we also need to mention that in order to fully model the behavior of a SSPD integrated with a HEMT read-out, it is not enough to simply use the above electrical model, as there are many physical processes at play simultaneously. The Joule heating occurs in parallel with cooling processes and the current redistribution [36] and, ultimately, a more complex "physical" model needs to be used. This will be investigated further in the later chapters of this thesis.

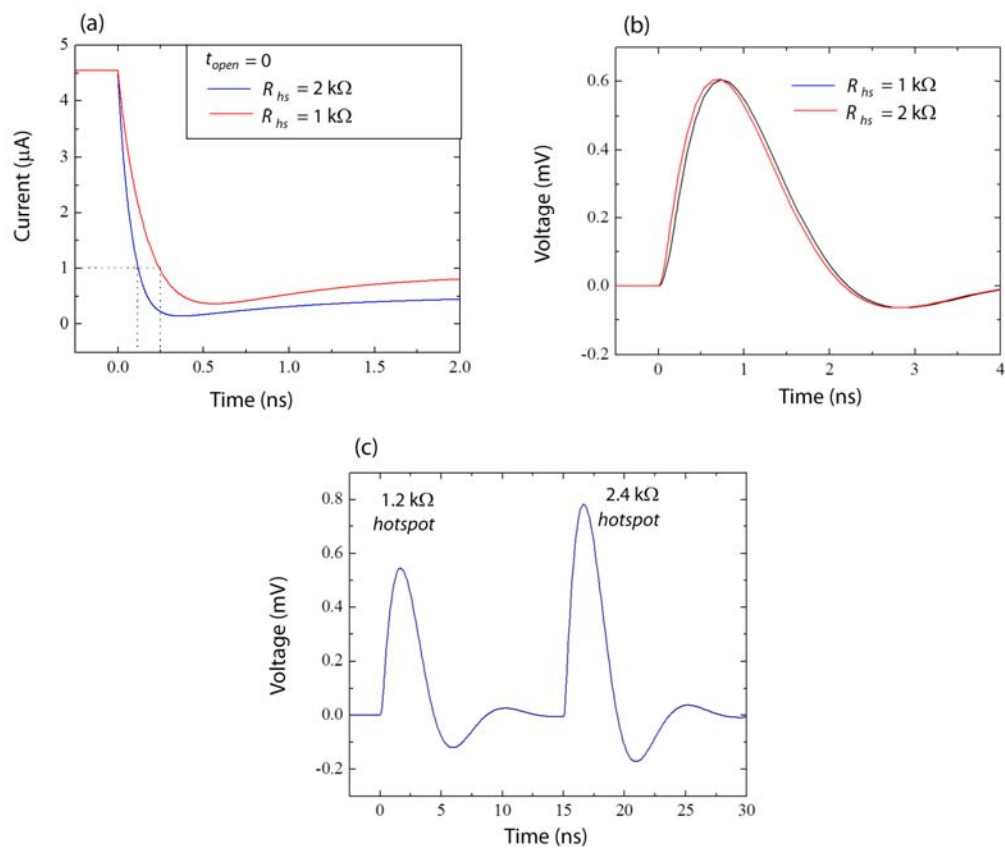


**Figure 2.9** (a) Current monitored through the SSPD during a photodetection event. Here, the switch remains open in order to observe better what happens to the current. (b) Comparison of two voltage pulses when the switch for a double-hotspot closes twice as fast. (c) Comparison of two voltage pulses when the switch for a single hotspot ( $t = 0$ ) closes as fast as that for a double-hotspot ( $t = 15 \text{ ns}$ ).

## Chapter 3 Dissipation and fluctuations in low-dimensional superconductors

### 3.1 Introduction

In this work, we are dealing with low-dimensional superconducting structures. A structure is two-dimensional (2D) when one of the transverse dimensions is smaller than the Ginzburg-Landau (GL) coherence length  $\xi$ . When both transverse dimensions are smaller than  $\xi$ , it is considered to be one-dimensional (1D). Our SSPD structures fall into the 2D category at all temperatures below  $T_c$ , except very near  $T_c$ , where  $\xi$ , because of its temperature dependence, becomes comparable with the width of the stripe; while the thickness is always  $d \leq \xi$ . Because 1D and 2D superconductors do not behave the same way as bulk superconductors, we have to take that into consideration when discussing SSPD operation, as these effects not only affect photodetection, but also give rise to fluctuations and dark counts.

True long-range order is not possible in low-dimensional systems. The superconducting order parameter is a macroscopic, complex wave function, and is given by [37]

$$\psi(\vec{r}) = |\psi(\vec{r})| \exp i\theta(\vec{r}), \quad (3.1)$$

where  $r$  is the spatial coordinate,  $\theta$  is the position-dependent phase, and the superfluid (Cooper pair) density is  $|\psi(\vec{r})|^2$ . When looking at the superconducting transition, in

1D and 2D superconductors, the transition region is broader than that in the bulk materials. This broadening is shown schematically in Fig. 3.1 [38]. Above the Bardeen-Cooper-Schrieffer (BCS) mean-field transition temperature  $T_c$ , the transition is dominated by fluctuations in the magnitude of the superconducting order parameter. This has the effect of increased conductivity before the actual transition, or paraconductivity, as discussed by Aslamazov and Larkin [39]. At  $T_c$ , the magnitude of the order parameter becomes well defined, but the resistivity does not drop directly to zero. Now, the broadening of the transition is due to fluctuations in the phase of the order parameter. When the phase fluctuates, it “slips” by  $2\pi$ . This happens in both 1D and 2D superconductors, via different mechanisms. It is thought that truly 1D wires never actually reach the state of total zero resistance [40],[41].

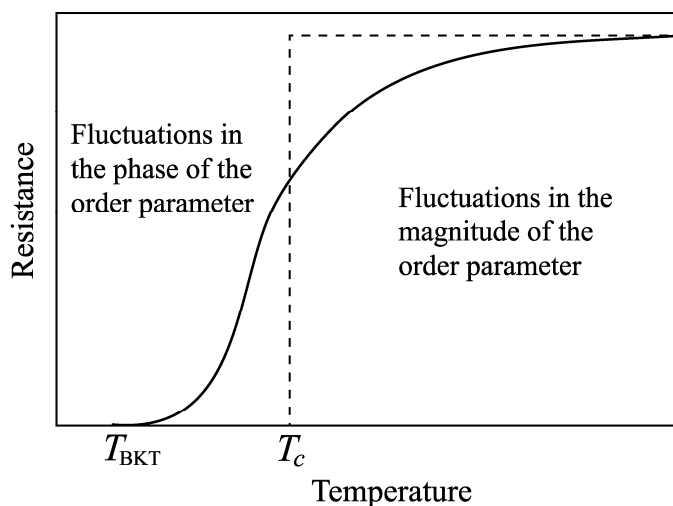


**Figure 3.1 Resistive transition in low-dimensional superconductors. Above  $T_c$ , the magnitude of the superconducting order parameter fluctuates, while below  $T_c$ , the phase of the order parameter fluctuates until a second transition temperature is reached, in this case, at  $T_{BKT}$  [38].**



### 3.2 Fluctuations in 2D superconductors: vortex-antivortex pairs

In 2D systems, destruction of the long-range order gives rise to the so-called topological defects in the order parameter. This phenomenon was first investigated by Kosterlitz and Thouless [42], and independently by Berezinskii [43] for superfluid helium films. In the following, I will discuss how it applies to thin superconducting films in general, and our devices in particular, within the framework of the Berezinskii-Kosterlitz-Thouless (BKT) model. The BKT model is applicable to phase transitions in a variety of 2D systems, such as planar spin systems, superfluid helium films, absorbed gases, etc. Very thorough theoretical discussions, and how they apply to superconducting films, are given by [44],[45],[46] with a good review of both theoretical and experimental results by [47].

In 2D superconducting films, the topological defects are excitations due to thermal fluctuations, and they come in the form of vortex-antivortex pairs (VAPs). In fact, one can observe a second transition below  $T_c$ , which we call a BKT transition  $T_{BKT}$ , below which the resistance goes to zero (see Fig. 3.1). In a temperature range between  $T_c$  and  $T_{BKT}$  both bound and unbound vortex pairs can exist. A vortex has the polarity of  $2\pi$  (while an antivortex has polarity of  $-2\pi$ ), and moving vortices (antivortices) produce dissipation in the temperature range between  $T_c$  and  $T_{BKT}$ . Below the BKT transition vortices with opposite polarities combine into pairs, and the resistance goes to zero [47]. A transport current, however, exerts a Lorentz force, which reduces the VAP binding energy, and thermal fluctuations can subsequently break the VAPs [46]. The latter effect can manifest itself as a spontaneous transient

resistive state. The VAPs are always present due to their finite excitation energies (on the order of  $k_B T$ ), and are analogous to electron-hole excitations in semiconductors [48].

The BKT model needed to be modified for superconducting films. A true BKT phase transition can occur only if the energy of a bound VAP depends logarithmically on separation  $r$ , which in superconductors happens only when  $r \ll 2\lambda_L^2/d$ , where  $\lambda_L$  is the bulk London penetration depth. [44]. For  $r > 2\lambda_L^2/d$  the binding energy becomes proportional to  $r^{-2}$ , which means that for large separations the binding energy is strongly reduced, unbound vortices exist at all temperatures, and there is no true BKT transition. Thus, in order to observe a BKT transition, one must be in the logarithmic regime, which limits the width of the film to  $w \ll 2\lambda_L^2/d$ . For dirty superconductors, this condition is easily satisfied as  $\lambda_L$  can be quite large, and it is satisfied in our experiments. Additionally,  $w \geq 4.4\xi$ , which insures that the width of the film is wide enough for VAPs to propagate [49]. Finally, in superconductors, the transition is somewhat smeared because some unbound vortices exist at all temperatures due to finite size effects and the finite binding energy of VAPs in conjunction with thermal fluctuations.

### 3.3 Fluctuations in 1D superconductors: phase slip centers

Some of our devices start to approach a 1D limit at temperatures close to  $T_c$ . In this regime, the superconducting channel may be too narrow for vortices to

navigate, and we must consider phase-slip centers (PSCs) as a source for dissipation and fluctuations. Theory of PSCs was first proposed by Little [50], and later developed by Langer, Ambegaocar, McCumber, and Halperin (LAMH) [51],[52]. The LAMH model is very well developed, and extensive literature on both the theory and experimental results is available [40],[41],[51]-[53]. Here, I will only summarize the results.

When a superconducting wire, or a stripe in our case, is biased at  $I_b < I_c$ , ideally the voltage drop between the two ends of the stripe is zero [54]. However, because of Johnson noise, thermal fluctuations, and possible nonuniformities in the width and thickness of the stripe, the voltage may not be exactly zero, though it will be extremely small. Then, the relative phase of the order parameter at the ends of the wire increases at the Josephson rate  $d\theta/dt = 2eV/\hbar$ , which is directly proportional to the voltage. In order to maintain steady state, the phase will keep increasing, until instantaneously snapping back by  $2\pi$  [53]. At that instant, the superconducting energy gap collapses at the core of a PSC. We consider the size of the PSC to be given by  $\xi$ . From the LAMH model, there are two types of PSCs: thermal, which exist near  $T_c$ , and quantum, which dominate at low temperatures.

Langer and Ambegaokar found the saddle-point energy for PSC activation by finding stable solutions to the 1D GL equations, of the form [54]

$$\Delta F = \frac{8\sqrt{2}}{3} \frac{H_c^2(T)}{8\pi} A \xi(T), \quad (3.2)$$

where  $H_c$  is the critical magnetic field, and  $A$  is the cross-sectional area of the wire. If the PSCs are thermally activated, they happen at a rate

$$\Gamma_{PSC} \sim \exp(-\Delta F / k_B T). \quad (3.3)$$

The activation energy  $\Delta F$  decreases as  $(1 - T/T_c)^{3/2}$  near  $T_c$ , which means that the probability of PSC activation grows exponentially with  $T$ . For quantum PSCs, which quite controversially have been recently observed by [55]-[57],  $k_B T$  in (3.3) is replaced by  $\hbar / \tau_{GL}$ , where  $\tau_{GL}$  is the temperature dependent GL relaxation time given by

$$\tau_{GL} = \frac{\pi \hbar}{8k(T_c - T)}. \quad (3.4)$$

### 3.4 Resistive transitions

In our devices, the resistive transition can be investigated in three different temperature regions. Above  $T_c$ , the excess conductivity (paraconductivity) in a superconductor is derived by Aslamazov and Larkin [39]:

$$\sigma_{2D} = \frac{1}{16} \frac{e^2}{\hbar d} \frac{T_c}{T - T_c} \quad (3.4)$$

for the 2D samples, and

$$\sigma_{1D} = \frac{\pi}{16} \frac{e^2}{\hbar w d} \xi_0 \left( \frac{T_c}{T - T_c} \right)^{3/2} \quad (3.5)$$

for 1D samples, where  $\xi_0$  is the GL coherence length at  $T = 0$ .

### 3.4.1 Two-dimensional nanostripes

Below  $T_c$ , in the framework of the BKT model, the resistance due to free vortices is directly proportional to the free vortex density  $n_f$ , and is given by [44]

$$R_{VAP}(T) = 2\pi R_N \xi^2(T) n_f(T), \quad (3.6)$$

where  $R_N$  is the normal-state resistance, and, one can find  $n_f$  by solving the Kosterlitz recursion equations [44],[45]. Finally, at temperatures  $T_{BKT} < T < T_c$ , the resistance is given by Halperin and Nelson [44]:

$$R_{HN} = 10.8bR_N \exp\left[-2\left(\frac{T_c - T_{BKT}}{T - T_{BKT}}\right)^{1/2}\right], \quad (3.7)$$

where  $b$  is a nonuniversal constant of the order unity. This temperature dependence may be difficult to observe in samples with  $R_s$  less than 1 k $\Omega$ , as the transition region  $\Delta T = T_c - T_{BKT}$  is quite small in such devices. The ratio  $T_{BKT}/T_c$  is given by [46]

$$T_{BKT}/T_c = [1 + 0.173R_s e^2 \varepsilon / \hbar]^{-1}, \quad (3.8)$$

where  $\varepsilon$  is a renormalization factor on the order of unity to take into account VAPs with smaller separation interacting with VAPs with larger separation. Given that the average  $R_s$  of our devices is  $\sim 800 \Omega$ , the transition region is  $\Delta T < 0.5$  K.

Below  $T_{BKT}$ , and in the limit of zero current, the dissipation (free vortices) is due to finite-size effects. Then (3.6), in the limit of large length scale, can be rewritten as [47]

$$R_{VAP} = 2\pi R_N \left[ \frac{T - T_{BKT}}{T_c - T_{BKT}} - 2 \left( \frac{\xi(T)}{w} \right)^{\frac{2(T_{BKT} - T)}{T_c - T_{BKT}}} \right] \quad (3.9)$$

In order to achieve current-induced unbinding of VAPs, where the Lorentz force has to exceed the attraction force of the pair, a certain threshold current  $I_{th}$  must be surpassed. This  $I_{th}$  increases with decreasing temperature, and is given by [38]

$$I_{th}(T) = 2eK(l_m)kT/\hbar, \quad (3.10)$$

where  $K(l_m)$  is the stiffness constant from the Kosterlitz recursion equations, bounded by the width of the film, and is given by  $K(l_m) = 2/\pi + 1/\pi \ln(w/\xi)$ . Then,  $I_{th}$  can be rewritten as [58]

$$I_{th}(T) \approx \left(1 + 2 \frac{T_C - T}{T_C - T_{BKT}}\right) \frac{2ekT}{\pi\hbar}. \quad (3.11)$$

In this regime, the resistance due to unbinding of VAPs is predicted to be [45], [58]

$$R_{VAP} \approx 4R_N \frac{T_C - T}{T_C - T_{BKT}} \left(\frac{I}{I_{sc}}\right)^{\frac{2(T_C - T)}{T_C - T_{BKT}}}, \quad (3.12)$$

where  $I_{sc} = wekT_{BKT}/\hbar\xi(T)$  is the scaling current.

### 3.4.2 One-dimensional nanowires

In the 1D regime, the resistive transition is dominated by thermally activated PSCs. It can be found that in the limit of low bias currents, the resistance is [40],[41], [52]

$$R_{PSC} = \frac{2hL}{\pi e^2 \xi(T)} \left(1 - \frac{T}{T_c}\right) \sqrt{\frac{\Delta F}{k_B T}} \exp\left(-\frac{\Delta F}{k_B T}\right), \quad (3.13)$$

and the activation energy can be written as [59]

$$\Delta F \approx 0.4k_B \frac{hw}{2e^2\xi(T)}(T_c - T), \quad (3.14)$$

where  $\xi$  has the temperature dependence of  $\xi = \xi_0(1 - T/T_c)^{-1/2}$ .

### 3.4.3 Resistance measurements

Five different structures were studied extensively for resistance measurements, as well as *IV* characteristics to be presented later: four nanobridge structures with different widths and a SSPD. Their geometries and device parameters are summarized in Table 3.1.

**Table 3.1** Device parameters

Type of structure	Nanobridge				SSPD
Device number	B1	B2	B3	B4	E11
Width $w$ (nm)	440	330	130	150	100
Thickness $d$ (nm)	4	4	4	4	4
Length $L$ ( $\mu\text{m}$ )	5	10	10	10	500
$R_s$ ( $\Omega/\text{sq}$ ), $T = 20$ K	890	670	900	720	700
$T_c$ (K)	13.36	11.37	9.87	--	9.98
$T_{BKT}$ (K)	12.88	11.06	9.51	--	--
$\varepsilon$	1.05	1.01	1.04	--	--

Figure 3.2 presents a semi-log plot of *RT* dependence for the B1 [Fig. 3.2(a)] and B2 [Fig. 3.2(b)] nanobridges. A lock-in technique described in Section 2.1 was implemented for these measurements. *RT* measurements for devices B3 and B4 were not available.

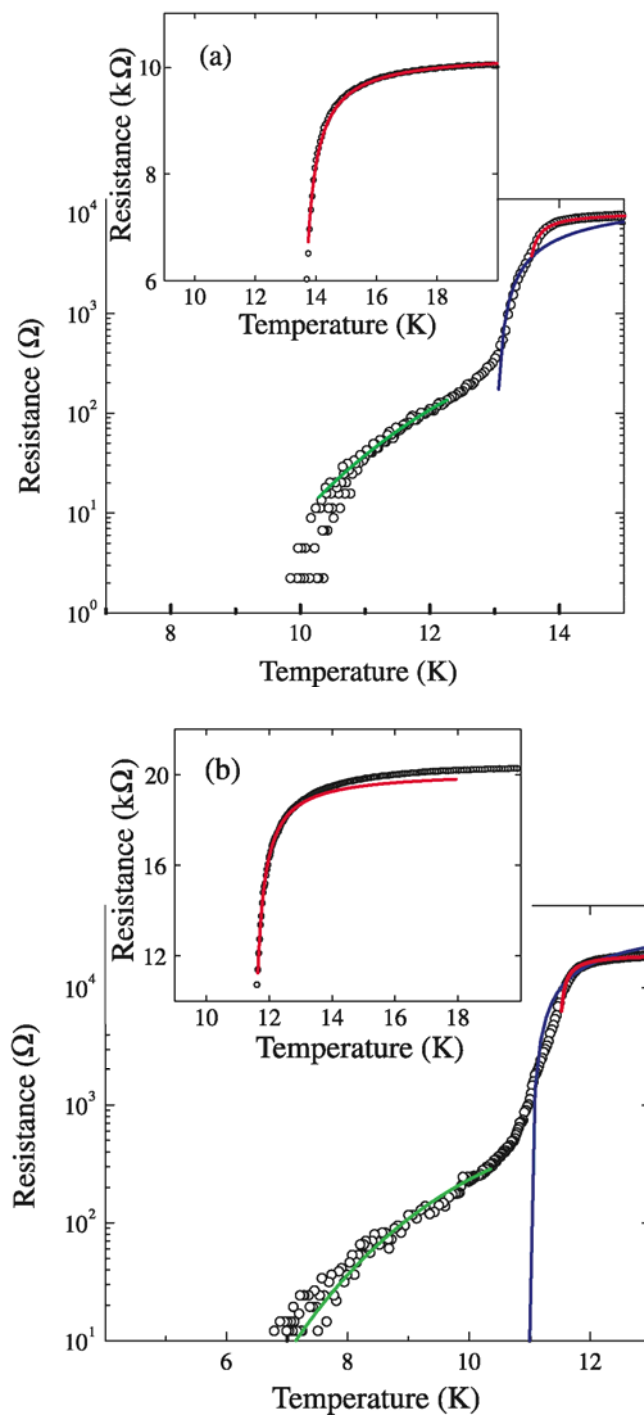


**Figure 3.2** Resistance versus temperature measurements for devices (a) B1 and (b) B2. The blue curves are fits from (3.7), and green curves are fits from (3.13). The insets show the measurements on a linear scale, with fits from (3.4).



Above  $T_c$ , the residual conductivity from (3.4) can be used to fit all our experimental data quite well, with  $T_c$  being the only free parameter. The resistance curve in this case is given by  $R_{AL} = R_N(1 - \sigma_{2D}\rho_N)$ , where  $\rho_N$  is the normal-state resistivity. The values of  $T_c$  derived in such a way for all four devices are listed in Table 3.1. A slight discontinuity feature around  $T = 13.7$  K in Fig. 3.2(a) is likely due to the fact that the contacts switch into superconducting state before the actual nanobridge structure.

Equation (3.8), by setting  $\varepsilon = 1$ , can give us the approximate values of the BKT transition, also listed in Table 3.1. It is interesting to compare the  $T_{BKT}$  values obtained this way with the values extracted from the fit of the transition using (3.7), also shown in Fig. 3.2, in the temperature range  $T_{BKT} < T < T_c$ . Comparing the two different  $T_{BKT}$  values for devices B1 and B2, we can find the renormalization factor  $\varepsilon$ . I must emphasize that the equations for the BKT model were derived for very large length scales, and we have a much better fit from (3.7) for device B1, which is wider than B2.

Finally, at temperatures below  $T_{BKT}$ , we can observe resistive tails in both samples. These are somewhat more difficult to explain. An attempt was made to check whether this is the broadening of the transition by vortices, either due to finite-size effects, or current induced VAP unbinding, given by (3.9) and (3.12). However, both of equations predict a transition that is only slightly broadened, and not to the extent which is observed here. At low currents, we can fit these data with the LAMH model. These structures are quite wide however, and the existence of PSCs, at first

glance, seems unlikely. Fitting these resistive tails with (3.13), and using  $L$  as a free parameter returns  $L \approx 240$  nm for device B1. Using (3.2) and the experimental value of  $H_c$  for NbN, we can calculate  $w \approx 19$  nm. A plausible explanation is that in our NbN stripes, there are local constrictions, or inhomogeneities, which have a lower  $T_c$  than the rest of the structure, and such regions activate PSCs [60].

Figure 3.3 shows the  $RT$  transition for device E11. This time the transition is completely dominated by the PSCs, as shown by the green curve in the figure. We set  $\xi_0 = 5$  nm, so that  $T_c$  was used as the only free parameter, which we found to be  $T_c = 10.7$  K. Given that the Aslamazov-Larkin fit gave  $T_c = 9.98$  K, there is a discrepancy of  $\sim 7\%$ , still within a reasonable range. Equation (3.7) from the BKT model is also plotted for comparison (blue curve), and the Aslamazov-Larkin fit is shown in the inset. It is not surprising that the PSC model fits for over five orders of magnitude, as this device, having the narrowest width, actually approaches the 1D limit at temperatures near  $T_c$ . Similar findings were presented in [60].

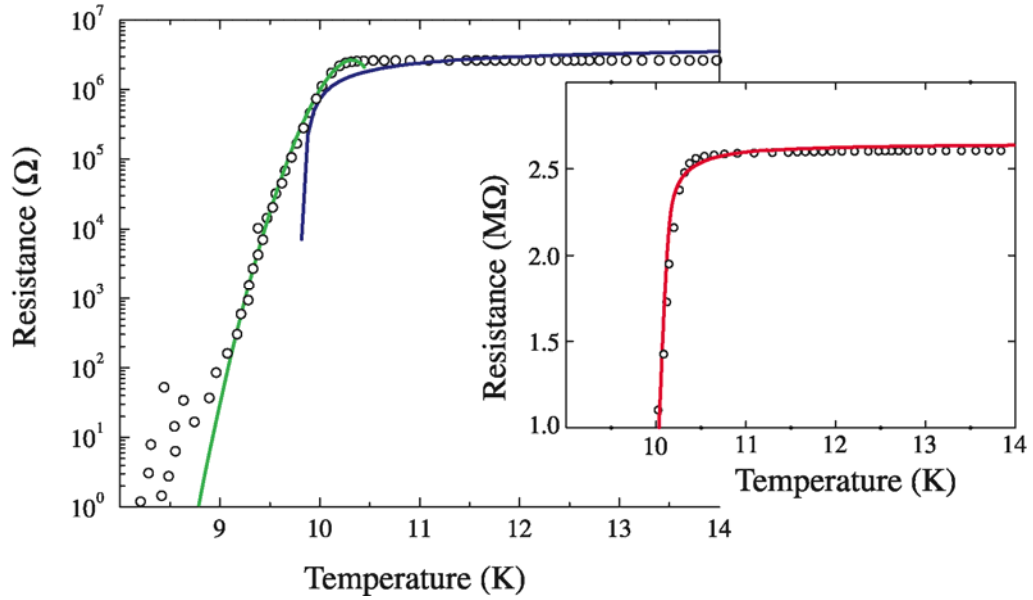


**Figure 3.3** Resistance versus temperature measurements for devices E11. The green curve is a fit from (3.13), with (3.7) plotted for comparison (blue curve). The inset shows the measurements on a linear scale, with a fit from (3.4).

### 3.5 Current-voltage characteristics

We can more directly probe the logarithmic interaction of two vortices in a pair by looking at dc  $IV$  characteristics near  $T_{BKT}$ . According to the BKT model [44],[47],[48], the voltage across the film is proportional to the power of current  $V \propto I^{\alpha(T)}$ , where  $\alpha$  is a temperature-dependent exponent.  $\alpha$  decreases linearly with increasing temperature until  $T_{BKT}$  is reached, at which point the  $IV$  curves stop being nonlinear and become ohmic and  $\alpha(T_{BKT}) = 3$ , while above  $T_{BKT}$  the exponent makes a sharp jump to  $\alpha = 1$ , where the superfluid density jumps to zero, and the curves become ohmic.

Figure 3.4(a) shows a log–log plot of a family of  $IV$  curves, taken for device B3 over a large range of currents and voltages, using a stable dc current source (Keithley 220). One can see that our  $IV$  characteristics are nonlinear for higher currents, as predicted by the BKT model. However, there is an ohmic tail at very low currents. This ohmic tail can be an artifact due to the current source noise, but is more likely due to unbound VAPs that seem to exist in our devices at all temperatures [61]. Since we used a  $\mu$ -metal shield around the sample, which reduced the background (Earth) magnetic field by about two orders of magnitude, the unbound VAPs are most likely related to the finite-size effects [47],[62]. The  $IV$  characteristics obtained for all other devices revealed similar results.

We have extracted  $\alpha$  from each experimental  $IV$  curve for each device and plotted it as a function of temperature, as shown in Fig. 3.4(b) for device B3. Because  $\alpha$  was obtained in the limit of high currents, where the  $IV$  characteristics were nonlinear, there is no “jump” from  $\alpha = 3$  to  $\alpha = 1$ , which should be observed in the limit of low currents. Again, this smooth transition may be attributed to unbound VAPs, as was discussed above.

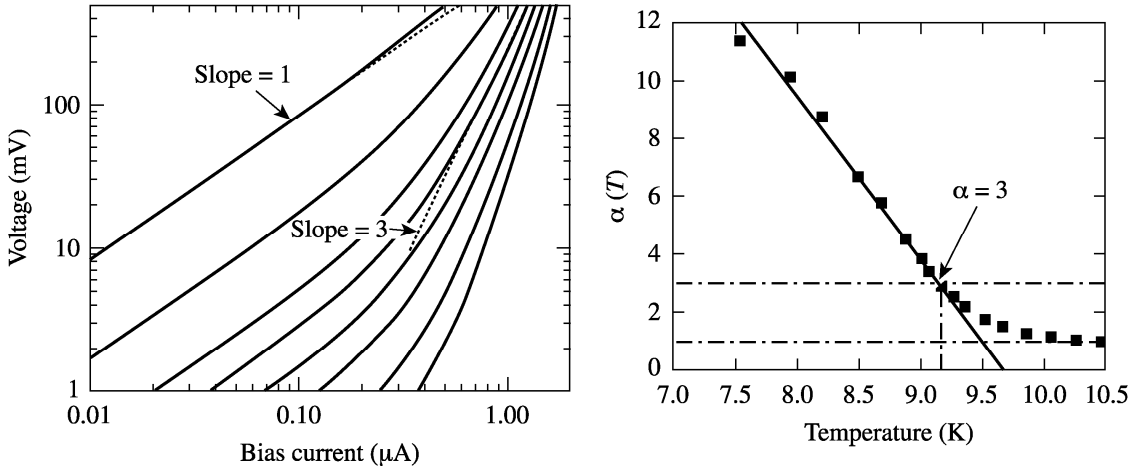


**Figure 3.4** (a) *IV* characteristics different temperatures near the superconducting transition for device B3. From left to right, the temperatures are: 10.06, 9.53, 9.27, 9.17, 9.07, 9.02, 8.88, and 8.68 K. (b) Exponent  $\alpha$  as a function of  $T$ . The BKT transition occurs at  $T = 9.17$  K.

From the *IV* characteristics, device B3 has  $T_{BKT} = 9.17$  K. Using (3.8) and the measured  $T_c = 9.87$  K, we get the renormalization factor  $\varepsilon = 1.04$ , fitting with BKT model very well.

Finally, we can look at transport properties by measuring *IV* curves far below  $T_c$ , as shown for device B4 in Fig. 3.5, at temperatures  $T = 2.3 - 9.0$  K. The steps in the *IV* curves, with excess current, are typically associated with PSCs [40].[41],[60], though alone are not a proof. We can argue, however, that in this particular device, the  $I_c$  is nearly three times smaller than in a typical device of similar dimensions, which indicates the existence of constrictions in the width and/or thickness of the stripe. The current exceeds  $I_c$  in the constrictions first, and, as described by Tinkham [54], stable superconducting solutions no longer exist, a finite electric field appears, and the superconducting order parameter collapses. Superconductivity is restored

after the phase slips by  $2\pi$ , and each PSC results in a voltage step. These voltage steps are not unique to device B4, but are quite common in most of our devices, and are expected to exist in devices with reduced  $I_c$ 's.

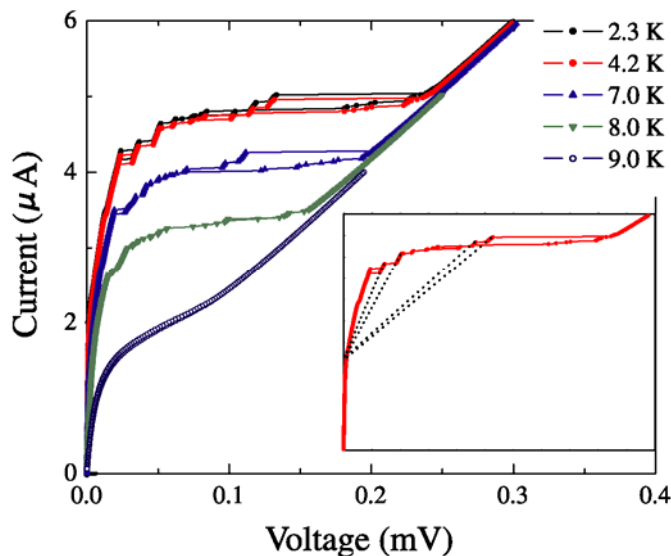


**Figure 3.5** Current-voltage characteristics measured for device B4 at different temperatures. The inset shows the curve at  $T = 4.2$  K once again, to demonstrate that the voltage steps have excess current (slope does not go back to the origin). The curves are also hysteretic.

### 3.6 Summary

Given all the evidence presented above, I would like to conclude that dissipation due to both VAPs and PSCs exists in our devices. Depending on the parameters of a particular device and the operating temperature, one process can dominate over another. For example, the  $RT$  measurements show that the resistive transition is dominated by PSCs in the narrower structures, even though the nonlinear  $IV$  characteristics reveal that VAPs are also present. Besides the stripe constrictions,

inhomogeneities, and defects in the substrate, which translate to the NbN film, can have a significant effect on the transport properties. Thus, fluctuations and dissipation are dependent not only on the sample's dimensions, but also on its quality. Typically, even the wider structures where VAP processes dominate, are not immune to PSCs near  $T_c$ .

## **Chapter 4 Dark counts: experimental results and interpretation**

In Chapter 1, we discussed that the SSPD time resolution is limited by the large value of  $L_k$  of the narrow, thin, and ultra-long superconducting stripe. This implies that no matter what causes the transient resistive state, whether it is a single photon, a pulse containing 10 photons, or a dark count, the response pulses are indistinguishable. Understanding the physical origin of dark counts in our SSPD nanostructures is important not only for the purpose of better operation of our devices (sensitivity depends on the dark count rate), but also to further our understanding of the physics of the photodetection mechanism in 2D superconducting stripes and 1D nanowires.

### **4.1 Experimental results**

The experimental setup for dark-count measurements was discussed in Chap. 2, and the NbN nanobridges tested in these experiments were 3.5-nm and 4-nm thick, the width ranging between 100 and 500 nm, with 10  $\mu\text{m}$  length. The meandering stripes of the measured SSPDs were 4 and 10 nm thick, 100 to 150 nm wide, and up to 500  $\mu\text{m}$  long. Table 4.1 summarizes the parameters of the measured devices: three



different SSPDs (samples A, B, and C), and nanobridges (D, E, F). Most structures fall into the 2D limit at all temperatures, as their thickness is much smaller, while the width is much larger than  $\xi$ , except sample F, whose thickness is on the order of  $\xi$ .

**Table 4.1 Parameters of measured devices**

Device #	A	B	C	D	E	F
Thickness $d$ (nm)	4	4	10	4	4	3.5
Width $w$ (nm)	120	120	150	170	100	500
Length $L$ ( $\mu\text{m}$ )	500	500	110	10	10	10
Sheet resistance $R_s$ ( $\Omega/\text{sq}$ ) at $T = 20$ K	700	660	550	600	900	900
$T_c$ (K)	9.0	9.3	10.0	10.2	9.8	10.3
QE at 1.3 $\mu\text{m}$ , %	0.3	8.0	--	--	--	--

Individual dark-count pulses, representative for simple nanobridges (E and F) and a long meanders (A and B), measured at different temperatures are shown in Figs. 4.1(a) and 4.1(b), respectively. The pulses recorded for the bridges exhibited the main peak with full-width-at-half-maximum (FWHM) of approximately 250 ps for F and 500 ps for E [inset in Fig. 4.1(a)]. On the other hand, voltage transients generated by SSPDs were in the several-ns-range (FWHM = 2.5 ns), due to the high  $L_k$  of the long meander structure [18],[27]. The amplitudes of dark count pulses for both types of structures were temperature dependent, which stems partly from the temperature dependence of the critical current density  $J_c$ , and will be discussed below.

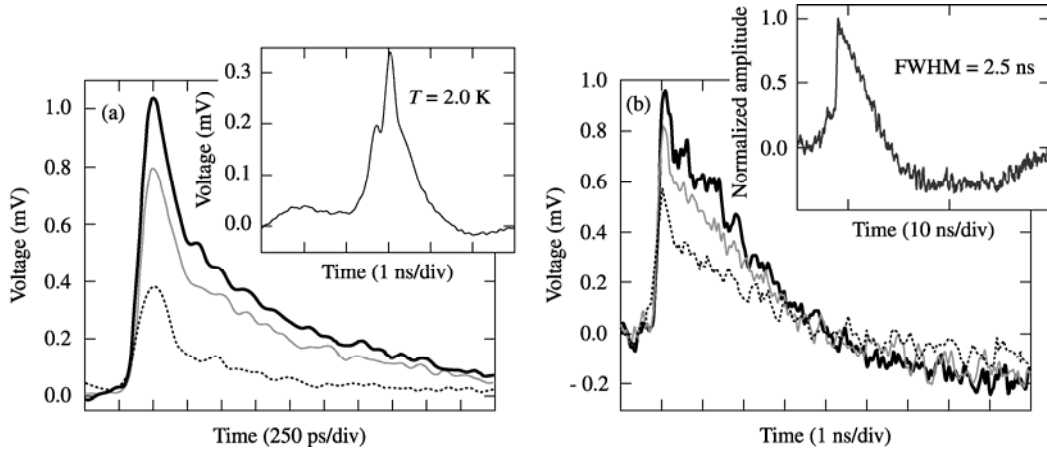


**Figure 4.1** Dark-count pulses for (a) device F and (b) device B at temperatures of 2.0 K (solid black line), 4.5 K (gray line), and 7.0 K (dotted line). The inset in (a) shows a typical dark-count pulse from device E, while the inset in (b) corresponds to device A.

## 4.2 Early data and discussion

Data for the spontaneous pulse-counting rate  $R_{dk}$  for sample A as a function of the reduced bias current  $I_b/I_c$  are shown in Fig. 4.2. We were able to observe an activation-type behavior of  $R_{dk} \propto \exp(I_b/I_c)$  within six orders of magnitude. To analyze the correlations between the device geometry and the  $R_{dk}$  behavior, we decided first to follow an approach developed in the LAMH model for 1D superconducting wires, as discussed by Tinkham [54] (also in Chap. 3). The LAMH model predicts that a voltage across a superconducting nanowire, due to PSCs, is

$$V = \frac{\hbar\Omega}{e} e^{-\frac{\Delta F}{kT}} \sinh \frac{\hbar I_b}{4ekT}, \quad (4.1)$$

where  $\Omega$  is the barrier attempt frequency found by McCumber and Halperin [52] to be

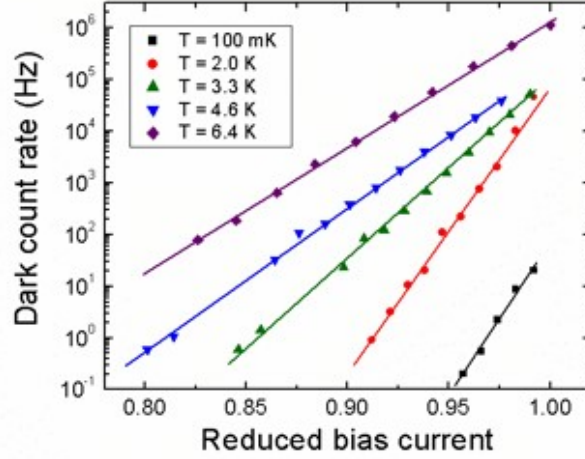


Figure 4.2 Dark counting rate dependence on the bias current for device A, in the temperature range between 100 mK and 6.4 K. The solid lines are fits according to the PSC model, with  $R_0$  and  $I_0$  as fitting parameters.

$$\Omega = \frac{L}{\xi} \frac{1}{\tau_{GL}} \left( \frac{\Delta F}{kT} \right)^{1/2}. \quad (4.2)$$

In our case of  $I_b$  close to  $I_c$ , the hyperbolic sine function in (4.1) can be approximated and written as

$$V = \frac{\hbar\Omega}{2e} e^{-\frac{\Delta F}{kT}} e^{\frac{I_b}{I_0}}, \quad (4.3)$$

where  $I_0$  is the characteristic current given by

$$\frac{I_0}{T} = \frac{4ek}{h} = 13nA/K. \quad (4.4)$$

Following the above approach and based on the experimental data shown in Fig. 4.2, we first fit our measured dark counts as an exponential function of  $I$ , as shown by solid lines in Fig. 4.2, in the following form:

$$R_{dk}(I) \propto R_0 e^{I_b/I_0}, \quad (4.5)$$

where the prefactor  $R_0$ , based on (4.2) and (4.3), can be written as

$$R_0 = \Omega \times \exp\left(\frac{-\Delta F}{kT}\right) = \frac{L}{\xi} \frac{1}{\tau_s} \left(\frac{\Delta F_0}{kT}\right)^{1/2} \exp\left(\frac{-\Delta F}{kT}\right). \quad (4.6)$$

Equation (4.6) corresponds to thermally activated PSCs that are observed near the superconducting transition.

During the course of our studies, we have collected a very large number of  $R_{dk}$  dependencies on  $I_b/I_c$  in the temperature range between 1.8 K and 7 K. Next, we extracted the parameters  $I_0$  and  $R_0$  from our experimental data and, for selected devices, plotted them as a function of  $T$ .

Figure 4.3 presents the measured  $I_0/T$  values versus  $T$  for samples A, B, C, and D. We note that our results strongly deviate from the 1D LAMH model, where  $I_0/T$  is expected from (4.4) to be a temperature-independent constant. Our data, however, converge to the predicted 1D limit of 13 nA/K at temperatures above 7 K, where the width of our samples starts to approach a quasi-1D limit. At the same time, the deviation from this limit is getting higher as the temperature decreases, and is also higher for device D, which has a stripe wider than the other three devices. The  $I_0/T$  dependence at low temperatures in the QPSC limit should follow the  $1/T$  dependence, which indeed it does, as we see in the inset of Fig. 4.3. The latter may be evidence in favor of quantum fluctuations, though we cannot rule out simple coincidence.

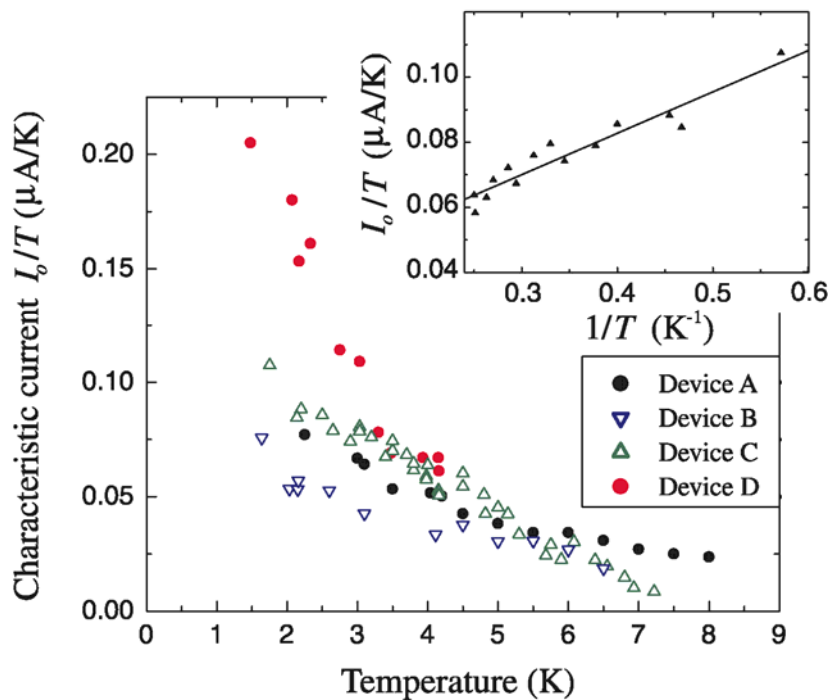


**Figure 4.3** Characteristic current for devices A, B, C, and D, extracted from dark counting rate data, as a function of temperature. The inset shows dependence on  $1/T$  for device B.

Figure 4.4 compares the  $R_0$ 's for devices A, B, C, and D. As in the case of  $I_0/T$ , the prefactors converge at high temperatures, as predicted by (4.6) for devices with the same  $L$ . At low temperatures, however, the  $R_0$ 's change dramatically, which means that the PSC interpretation of the data at low temperatures is likely incorrect, which is not surprising given that our devices are all in 2D limit except for temperatures approaching  $T_c$ . Thus a different model is needed to describe dark counts at low temperatures.

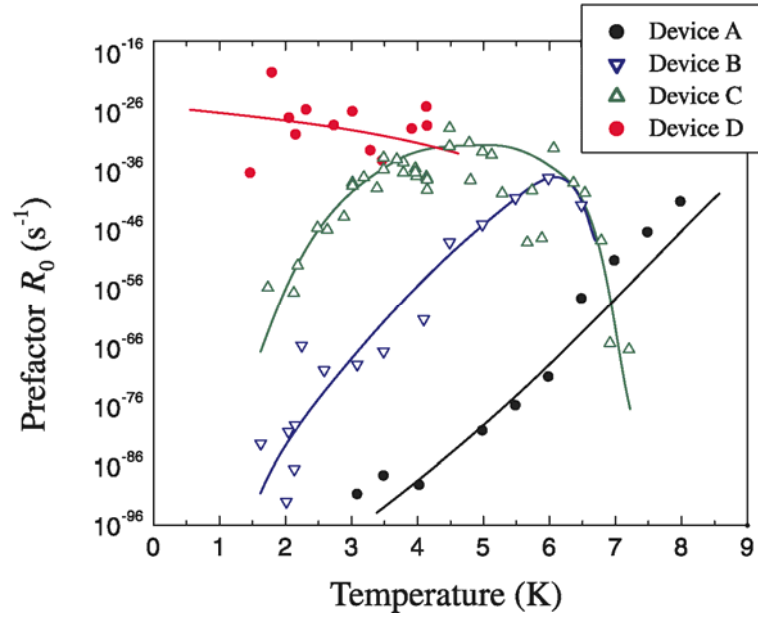


Figure 4.4 Prefactor  $R_0$  for devices A, B, C, and D, extracted from dark counting rate data, as a function of temperature. Solid lines are guides to the eye.

### 4.3 Vortex-antivortex unbinding approach

Devices E and F were later measured for dark counting rate as a function of bias current in a range of temperatures, from 2 to 8 K. Figure 4.5 shows some of these data for device F, this time, however, we used a VAP unbinding model derived by Engel *et al.* [62] (solid lines) to fit the new data. We note that the agreement is excellent and extends over six orders of magnitude.

In the sample, VAPs orient themselves perpendicular with respect to  $J_b$  with minimum binding energy

$$U = \frac{A(T)}{\epsilon(l_j)}(l_j - 1) + 2\mu_c, \quad (4.7)$$

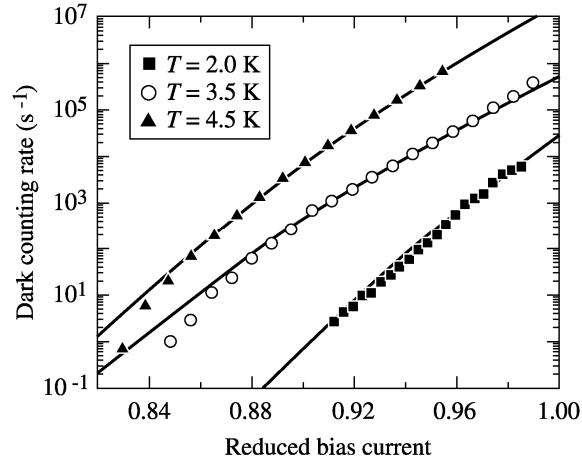


**Figure 4.5** Dark counting rate dependence on bias current for sample B, where the solid lines are fits according to (4.9).

where  $l_j = \ln(2.6J_c/J)$  is the current scale,  $\varepsilon(l_j)$  is the renormalization factor of the order unity due to the screening of larger VAPs by the smaller VAPs,  $\mu_c$  is the core potential, and finally  $J_c$  and  $J$  are the critical current density and the applied current density, respectively. Here,  $A(T)$  is the vortex interaction parameter, given by

$$A(T) = \frac{\pi^2 \hbar}{2e^2 R_s} \Delta(T) \tanh[\Delta(T)/kT]. \quad (4.8)$$

If the unbinding process is activated thermally, then  $R_{dk}$ , in [62] denoted as  $\Gamma_{VAP}$ , is proportional to  $\exp(-U/kT)$ , and is given by

$$\Gamma_{VAP} = \Omega_{VAP} \exp\left[\frac{A(T)}{\varepsilon(l_j)kT}\right] \times \left(\frac{J}{2.6J_c}\right)^{\frac{A(T)}{\varepsilon(l_j)kT}}. \quad (4.9)$$

Here,  $A(T)$  was calculated from device parameters,  $\Omega_{VAP}$  is the attempt frequency and was used together with  $\varepsilon(l_j)$  as the two fitting parameters which are summarized for devices F and B in Figs. 4.6(a) and 4.6(b), respectively.

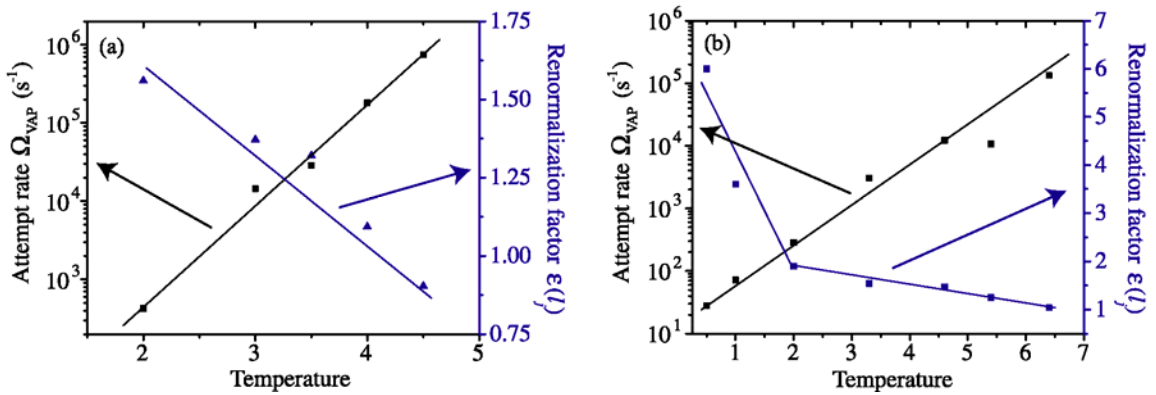


Figure 4.6 Fitting parameters  $\Omega_{VAP}$  (left axis) and  $\epsilon(l_j)$  (right axis) from (4.9) for (a) device F and (b) device B.

The attempt rate, as expected, increases with increasing temperature. The renormalization factor  $\epsilon(l_j)$ , however, decreases with increasing temperature, which is not consistent with theory. VAPs are thermal excitations, and at higher temperatures there are likely to be more of them present than at  $T \ll T_c$ , making  $\epsilon(l_j)$  increase with temperature [46],[63] in the limit of zero current. The renormalization factor should, however, also have a weak linear dependence on the bias current, which we did not take into account, as our fits were very good assuming a constant  $\epsilon(l_j)$ . We must admit, however, that our measurements were done in the limit of high currents, making the theoretical derivations not fully applicable to our results.

#### 4.3.1 Pulse amplitudes

In the presence of a bias current, the binding energy of VAP is reduced to [64]



$$U(J) \approx 2\pi K_0 \ln(J_{c0}/J_b), \quad (4.10)$$

which is comparable with  $k_B T$ . Here  $2\pi K_0 = \Phi_0 d \xi J_{c0}$  is the vortex energy scale, where  $J_{c0}$  is the mean-field critical current density and  $\Phi_0$  is the flux quantum. Thus, a voltage that corresponds to the depairing of a VAP, as a function of current and temperature, is given by

$$V(J, T) \approx \frac{\Phi_0}{e} e^{\xi(T) J_{c0}(T)} \ln(J_{c0}/J_b). \quad (4.11)$$

Figure 4.7 shows the amplitudes of dark voltage pulses (solid dots) versus temperature for devices F [Fig. 4.7(a)] and B [Fig. 4.7(b)]. Assuming that  $J_{c0}(T)$  is the experimentally measured quantity, and keeping  $J_{c0}/J_b$  ratio constant, we fit the amplitudes of the voltage pulses versus temperature for devices B and F with (4.11) (solid line).  $\xi(T)$  was extracted from experimental values of  $V(T)$  and  $J_c(T)$ , and by extrapolating the value of  $\xi$  to  $T = 0$ , we found that  $\xi(0) = 7$  nm and 6.1 nm for devices B and F, respectively. The  $\xi(0)$  values are within a reasonable range of values for NbN reported in literature [65], [66], supporting our interpretation. The dotted lines in Fig. 4.7 show what the amplitudes of dark-count pulses would be if they were simply equal to the bias current times the load resistance ( $R_L = 50 \Omega$ ), which clearly is not the case here, although they do look proportional, because (4.11) has a direct dependence on the bias current.

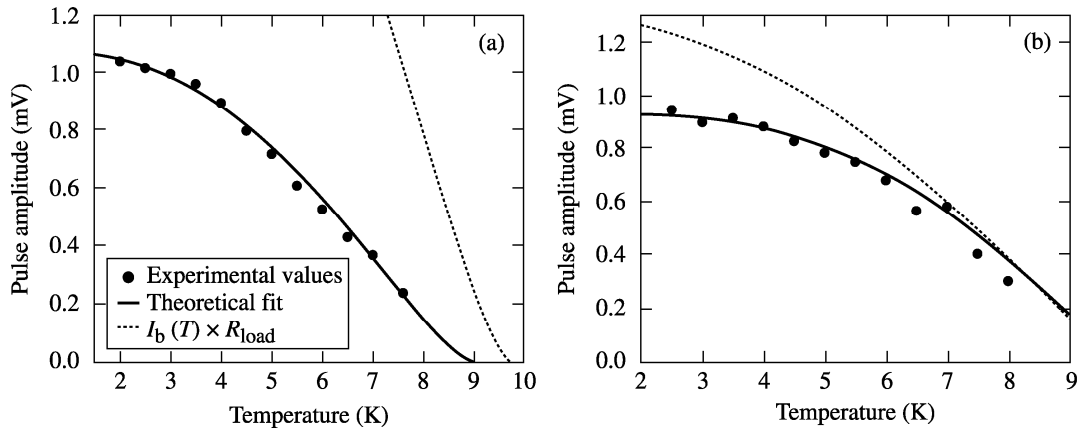


**Figure 4.7** Dark-count pulse amplitudes versus temperature for (a) device F and (b) device B. The solid line is a theoretical fit from (4.11), while the dotted line represents what would be a simple resistive behavior.

#### 4.4 Summary

In Chapter 3, I outlined the evidence for the existence of VAPs in our devices. Dark counts happen at  $I_b$ 's not far below  $I_c$ , and it stands to reason that the current-induced VAP unbinding is a likely process. By measuring  $R_{dk}$ 's, we demonstrated that this is indeed what happens, and in wider structures, it seems to be the dominant source of fluctuations.

However, as we stressed in the Summary of Chap. 3, we cannot totally discount the presence of PSCs in our devices, especially at temperatures approaching  $T_c$ , where the narrowest ( $w = 100$  nm) NbN stripes start to approach a quasi-1D limit. Because the NbN stripes are not perfectly uniform in width, some constrictions must exist, and, since we bias our devices close to  $I_c$ , PSCs are very likely to happen at the constriction sites. The superconducting energy gap at those sites will collapse, and the phase of the order parameter will slip by  $2\pi$  at a certain rate, and this rate

increases exponentially with  $I_b$ . We also have evidence for this from our  $R_{dk}$  values, and again from the steps in  $IV$  characteristics presented in Chap. 3. I then conclude that we have a superposition of dark counts due to both current-induced VAP unbinding, and PSCs, in our samples. Depending on the variables such as sample width, width/thickness uniformity, and temperature, one process will dominate over the other. Given our typical SSPD operating temperatures ( $T \leq 1/2T_c$ ), in the high-QE devices (high QE implying uniformity in stripe width and thickness), VAP unbinding should dominate over PSCs, while dark counts in our early, less-perfected technologically SSPDs are likely to be dominated by PSCs.

## Chapter 5 Hotspot dynamics

### 5.1 Hotspot model

I have already outlined in Chap. 1 that the SSPD photoresponse is based on hotspot formation in a constricted volume (sidewalks) of a superconducting nanowire. Here, we provide a much more detailed discussion and show that the SSPD operation principle is actually due to a supercurrent-enhanced resistive transition resulting from hotspot formation [10],[21], shown schematically in Fig. 5.1. as before, our phenomenological model assumes that the device is maintained at a temperature far below  $T_c$ , and is biased with current close to the NbN stripe  $I_c$ . After a photon of energy  $h\nu$  is absorbed, it breaks a Cooper pair, generating a highly excited quasiparticle, which, following either the R-T or 2-T models (both described in Chap. 1), through a cascade of secondary  $e-e$  and  $e-ph$  interactions, leads to a large number of NQPs forming a local hotspot region of suppressed/destroyed superconductivity.

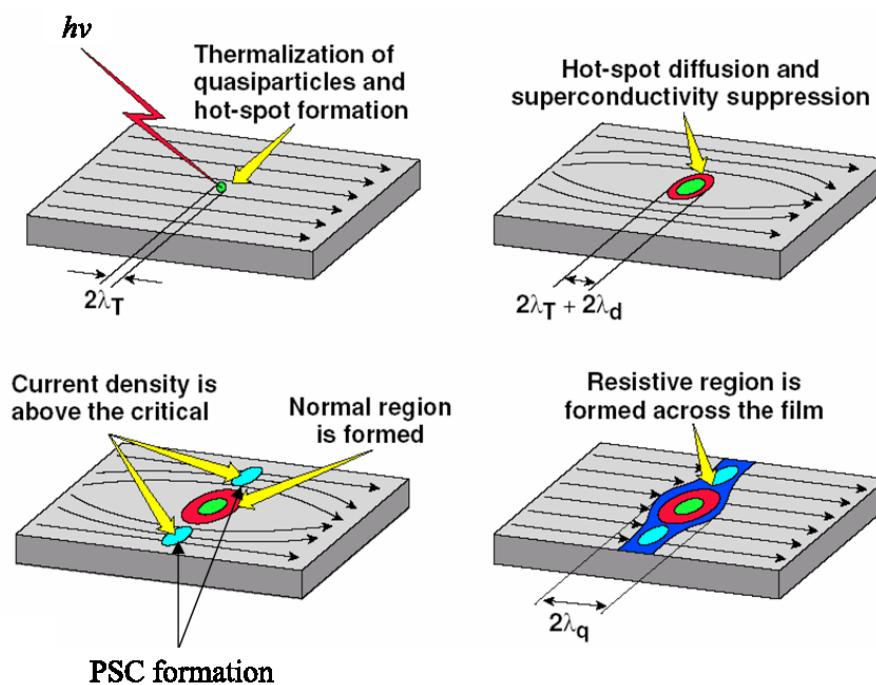


Figure 5.1 Hotspot model for single-photon response.

Next, the hotspot expands, forcing the bias supercurrent to be expelled from its volume and concentrated near the edges, or "sidewalks", of the stripe. When the current density in the sidewalks exceeds the critical value, superconductivity is locally destroyed due to formation of PSCs (see Chap. 3 for background on PSCs), and a resistive region is formed across the width of the stripe. This resistive region gives rise to a voltage signal. After the photon excitation, the hotspot continues to grow due to Joule heating. Once the current through the SSPD drops and redistributes into the read-out circuit, the hotspot can start to decrease due to recombination and out-diffusion of quasiparticles, and eventually collapses. The superconductivity in the entire stripe is restored and the detector is ready to register

another photon. We note that the presented mechanism can lead to a macroscopic voltage signal only in nanostructured superconducting stripes, which have  $d$  smaller and  $w$  comparable with the hotspot dimensions.

### 5.1.1 Hotspot radius

In an infinitely large superconducting film, we can calculate the maximal hotspot radius  $r_m$  [21]:

$$r_m = \left( \frac{M}{2D\tau_{th}dN_o\Delta} \right)^{1/2} \left( \frac{1}{\pi^4 N_o\Delta} \right)^{1/3} \ln \left( 1 + \frac{\pi^2 M}{D\tau_{th}dN_o\Delta} \right), \quad (5.1)$$

where  $M = \zeta h\nu/\Delta$  is the efficiency of NQP multiplication, with the material-related parameter  $\zeta < 1$ , which accounts to the energy losses by subgap phonon generation in the superconductor.

In the case of our SSPDs, where  $w = 100$  nm, and photon wavelength is in the NIR region,  $2r_m < w$ . Then, the device photoresponse is a trade-off between the bias current and hotspot diameter, related by the criterion  $2r_m = w(1 - J_b/J_c)$ , where  $J_b/J_c$  is the reduced current density of the superconducting stripe, or the minimum bias current needed to produce a photoresponse signal in the SSPD for a hotspot of diameter  $2r_m$ . In other words, the detector's sensitivity is enhanced by the supercritical current self-induced Joule heating of the still superconducting sidewalks around a comparatively small hotspot.

The criterion given above implies that there should be a cut-off in the QE below some value of  $J_b/J_c$ . Figure 5.2 shows the QE dependence on the reduced current bias for several temperatures, where instead of zero QE below the cut-off, we

see a change of slope where QE starts to drop off much faster with the  $J_b/J_c$  decrease. This residual QE is likely due in part to the nonuniformities in the stripe, where the parts of the stripe with  $w < 100$  nm are still activated for photodetection even below the “global”  $J_b/J_c$  cut-off, and partly due to fluctuation-enhanced photodetection. Let us set aside those effects to be discussed later, and first focus on the hotspot dynamics and temperature effects.

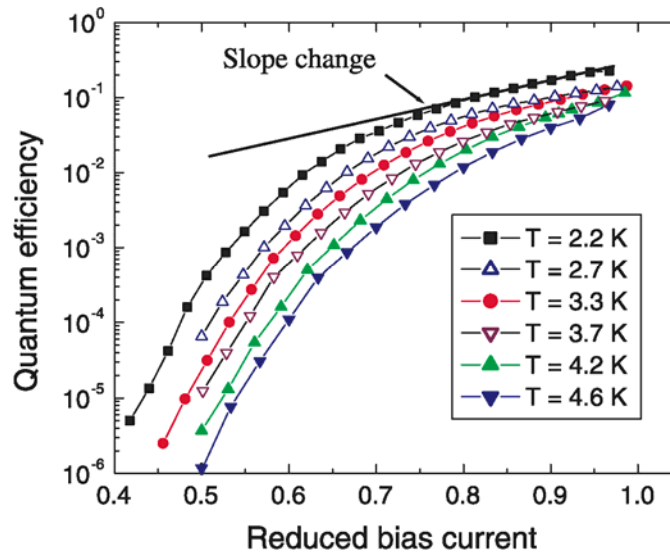


**Figure 5.2** SSPD quantum efficiency as a function of bias current at different ambient temperatures.

From the data in Fig. 5.2, for each  $T$ , we calculated the minimum hotspot radius needed to produce a photoresponse by using the values of the  $J_b/J_c$  threshold where the slope change occurs in QE. These are presented in Fig. 5.3 (closed circles), compared with the curve from (5.1) (red curve), where  $\Delta$  is assumed to be temperature dependent, but independent of bias current, and  $\zeta = 0.75$ , a value

obtained for 700-nm-wavelength photons from previous measurements [67]. Note that according to (5.1),  $r_m$  increases slowly with  $T$ , diverging near  $T_c$ . The measured values of  $r_m$ , on the contrary, decrease monotonically with increasing  $T$ , while simultaneously giving almost twice larger values than those calculated from (5.1).

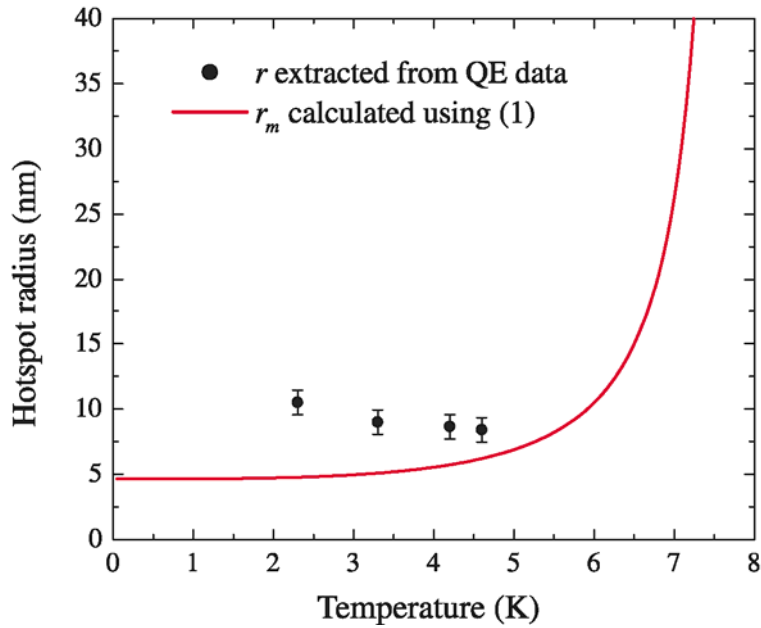


**Figure 5.3** Hotspot radius extracted from QE measurements as a function of temperature (closed circles), and  $r_m$  calculated from (5.1) (red curve).

As presented in Fig. 5.4, our model also proposes that the  $r_m$  – radius hotspot, which consists of the QP core, is surrounded with the  $L_E$  – wide ring of weak superconductor, where  $\Delta$  is suppressed by the electric field penetration into the superconductor at the boundary with the normal spot (N-S boundary) [21]. Here,  $L_E = (D\tau_Q)^{1/2}$  is the penetration length of electric field at the boundary, which affects the dissipation of the bias current in the superconductor, as well as the time of the



hotspot evolution across the width of the superconducting stripe, and  $\tau_Q$  is the relaxation time of the charge imbalance. Relaxation of the charge imbalance depends on  $I_b$ , and for the currents close to  $I_c$  and near  $T_c$ , it is given by [68]

$$\tau_Q = 0.55 \left( \frac{\hbar \tau_e T_c}{k_B (T_c - T)^2} \right)^{1/2}, \quad (5.2)$$

where  $\tau_e$  is the inelastic electron scattering time at the Fermi surface.

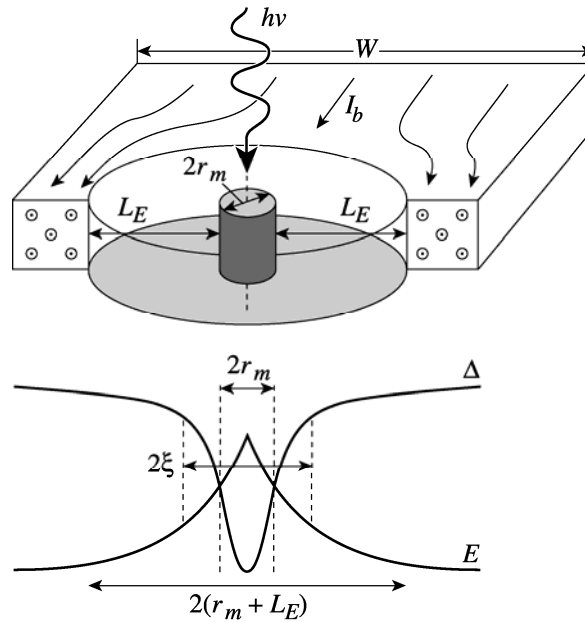


**Figure 5.4** Cross-section of the SSPD nanowire, showing the hotspot generated by a single photon. The original hotspot consists of a QP core with diameter  $r_m$ . Due to QP out-diffusion and electric field penetration at the normal (hotspot) boundary with the superconductor, the total hotspot diameter is now  $2(r_m + L_E)$ . The supercurrent, denoted by the arrows, is now expelled from the hotspot region into the stripe edges.

The hotspot evolution must also depend on the “healing” processes by the means of fast diffusion of highly-energetic QPs from the resistive area, and cooling down of the QPs due to sharing their energy surplus via  $e-ph$  interactions. The characteristic healing length of the hotspot is given by  $L_h = (D\tau)^{1/2}$ , where

$\tau = \tau_{e-ph} + \tau_{es} c_e / c_{ph}$  is the effective electron cooling time. Thus, in principle, effective hotspot radius should be  $r = r_m + L_E - L_h$ . When the healing length  $L_h > (r_m + L_E)$ , the supercritical current state in the sidewalk disappears, and the detector is unable to register the absorbed photon. In the temperature range of interest,  $L_E$  and  $L_h$  vary only weakly with  $T$ , and adding  $L_E - L_h$  to the red curve in Fig. 5.3 would move it up, depending on the  $L_E > L_h$  condition. This corrects the amplitude prediction, but still does not give us a good temperature fit for the data extracted from Fig. 5.2, thus, an alternative approach is needed.

## 5.2 Revised hotspot model: heating effects and resistive domain wall propagation

In this section, I demonstrate that the heating effects, namely Joule heating, play an important role in the SSPD photodetection mechanism. Let us assume a stepwise heat-production model as discussed by Gurevich and Mints [69], where the resistance  $R = 0$  for  $T < T_r$ , and  $R = R_{hs}$  for  $T > T_r$ , where  $T_r$  is the temperature at which some part of our SSPD nanostripe stops being superconducting. For the sake of simplicity, let us make the following assumptions:  $J_c(T)$  decreases linearly with increasing  $T$ , the  $\rho_N$ , along with the heat-transfer coefficient  $h$  from the NbN film to the substrate, are independent of temperature, and  $T_r \approx T_c$ .

When  $I_b < I_c$ , in the absence of inhomogeneities and/or external perturbations, the thin superconducting film will stay superconducting. This is not typically the

case, however, as in our very long and narrow SSPD stripes, inhomogeneities, such as constrictions and nonuniformities in the width or thickness, and/or defects in the film material and sapphire substrate are likely to be present. The measured  $I_c$  is then determined by the narrowest and thinnest sections of the stripe. These same sections are also the most sensitive to both thermal fluctuations and external perturbations. As  $I_b$  is driven close to  $I_c$ , these constricted sections start switching to the resistive state first.

We can define a parameter  $\alpha_s$ , called the Stekly parameter, as the ratio of characteristic heat generated in the normal state, to the heat transfer into the substrate [69]:

$$\alpha_s = \frac{\rho J_c^2(T_0) d_p}{h(T_c - T_0)}. \quad (5.3)$$

Here,  $T_0$  is the bath temperature, and  $d_p = wd/(2w + 2d)$ . Self-heating is important when  $\alpha_s > 1$ , and is negligible for  $\alpha_s \ll 1$ . Thus, taking into consideration the temperature dependence of  $J_c$ ,  $\alpha_s$  decreases with increasing  $T_0$ , and self-heating becomes unimportant at temperatures close to  $T_c$ , vanishing at  $T_c$ .

Consider  $IV$  characteristics of a typical SSPD, in the fixed-voltage regime, shown in the Fig. 5.5. The current is increased while the voltage drop is zero up to  $I_c$ , where the narrowest/thinnest portion of the stripe switches to the normal state. The normal domain grows to a resistance larger than the  $50\text{-}\Omega$  load, and  $I_b$  through the SSPD drops to a value  $I_l$ , and becomes stable. The current through the SSPD can then increase again, until a second normal domain appears, and the current drops

again to a value  $I_2$ . This process continues until the domains overlap, normal-superconducting (N-S) boundaries disappear, and the entire stripe becomes normal. When we finally start decreasing the current, the power dissipated by Joule heating is high enough to keep the SSPD in the normal state until  $I_b = I_r$ , at which point the superconducting state is recovered. Thus a hysteretic  $IV$  curve behavior is observed.

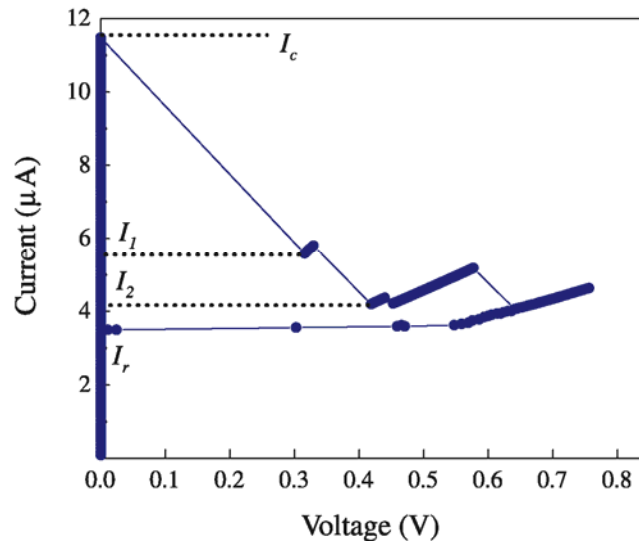
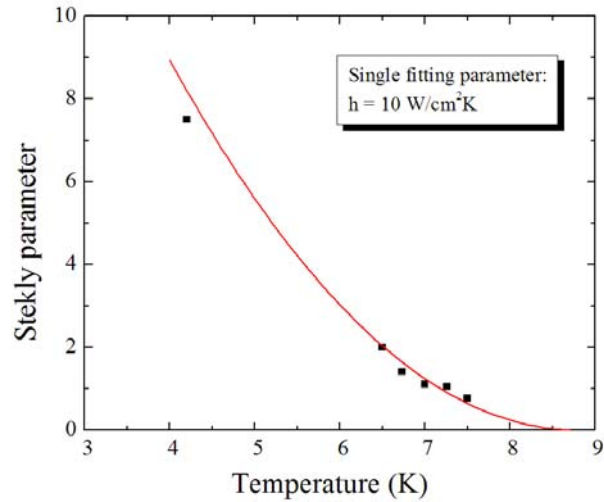


Figure 5.5 Typical SSPD current-voltage characteristics at  $T = 4.2$  K.

We associate  $I_r$  with the minimum normal-zone propagating current  $I_p$  [69], so that for a long stripe,  $I_r \approx I_p$  and is given by  $I_p = \frac{I_c}{2\alpha_s}(\sqrt{1+8\alpha_s} - 1)$ , for  $\alpha_s \geq 1$ .

Extracting  $I_p$  from our hysteretic  $IV$  curves, we were able, in turn, to extract  $\alpha_s$  at different temperatures, and fit the data with (5.3) using only one fitting parameter,  $h = 10^5$  W/m<sup>2</sup>K, of the same order as that calculated for NbN devices by Yang *et al.* [36]. This is presented in Fig. 5.6.



**Figure 5.6** Stekly parameter  $\alpha_s$  as a function of temperature.

Thus, the propagation of the N-S boundary of the hotspot in a superconducting thin film occurs at  $I_p < I_b < I_c$ . A photon absorbed in a SSPD is a perturbation, and a hotspot appears at the photon absorption site, with the N-S boundary propagating outward (see Fig. 5.4). The velocity of N-S boundary passes through zero at  $I_b = I_p$ , increases as  $I$  increases, and becomes maximum at  $I_b = I_c$ . Assuming that  $\alpha_s$  for our NbN film is  $\sim 7$ , which is true for typical SSPD operating temperatures, then  $I_p \sim 0.43 I_c$ , which indicates that self-heating due to a bias current is expected even at  $I_b \ll I_c$ , and the hotspot will keep growing until the current through the SSPD drops below  $I_p$ .

For a thermally insulated superconductor, where the heat transfer from the film to the substrate coefficient is  $h \rightarrow 0$ , the N-S boundary propagation velocity  $v$ , in the limit of  $\alpha_s \gg 1$ , is given by [69]:

$$v = \frac{J_c}{c_e + c_{ph}} \sqrt{\frac{\sigma_{th}\rho}{T_c - T}} \frac{i}{\sqrt{1-i}}, \quad (5.4)$$

where  $\sigma_{th}$  and  $\rho$  are the thermal conductivity and resistivity, respectively, at the superconducting transition of the SSPD, and  $i = I_b/I_c$ . Figure 5.7 shows the dependence of  $v$  on reduced  $I_b$  at  $T = 4.2$  K, with  $J_c = 3 \times 10^{10}$  A/m<sup>2</sup>,  $\sigma_{th} = 1$  W/m K [21],  $\rho = 2.4 \times 10^{-6}$   $\Omega$ m,  $c_e = 2400$  J/m<sup>3</sup>K, and  $c_p = 9800$  J/m<sup>3</sup>K [21]. At  $i = 0.9$ ,  $v = 5500$  m/s, which seems rather high, but reasonable as long as this value is lower than the speed of sound in NbN.

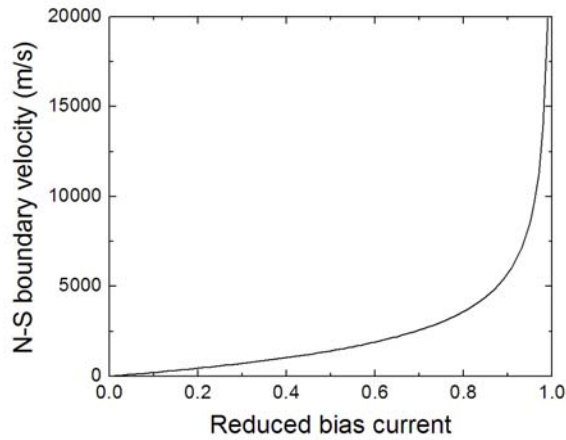


**Figure 5.7 Resistive domain propagation velocity as a function of reduced bias current, at  $T = 4.2$  K.**

Using the same values of  $i$  which were used to extract hotspot radius from QE measurements shown in Fig. 5.2 (see also Fig. 5.3), we were able to fit these data using (5.4), as presented in Fig. 5.8. Multiplying the  $v$  by  $\tau_{th}$ , and using a single fitting parameter of 0.34, we get the values of  $r_m$  (black curve) which are in very good agreement with the data. For comparison, Fig. 5.7 also shows  $r_m$  calculated from

(5.1). Furthermore, if we multiply  $v = 5500$  m/s calculated above by our fitting parameter of 0.34, we get a much more reasonable value of resistive domain velocity,  $v = 1870$  m/s. Thus, because  $v$  has a strong dependence on  $I_b$  near  $I_c$  at  $T \leq 1/2T_c$ , where SSPDs are typically operated, the bias current dependence dominates over the temperature dependence shown in Fig. 5.3. Also, because of the linear dependence of  $v$  on the  $J_c$ , which has temperature dependence given by  $J_c(T) \approx J_c(0)(1 - T/T_c)^{3/2}$ , the N-S boundary velocities for the same  $i$  are higher at lower temperatures, giving rise to a larger hotspot radius. Thus, indeed, the device QE should increase with the ambient  $T$  decrease even at temperatures  $T/T_c < 0.5$ , where the superconducting parameters such as  $\xi$ ,  $\Delta$ , and  $\lambda_L$ , are practically independent of  $T$ . Indeed, for the same  $i = 0.9$ , the QE at  $T = 2.2$  K is 4.3 times larger than that at  $T = 4.6$  K.

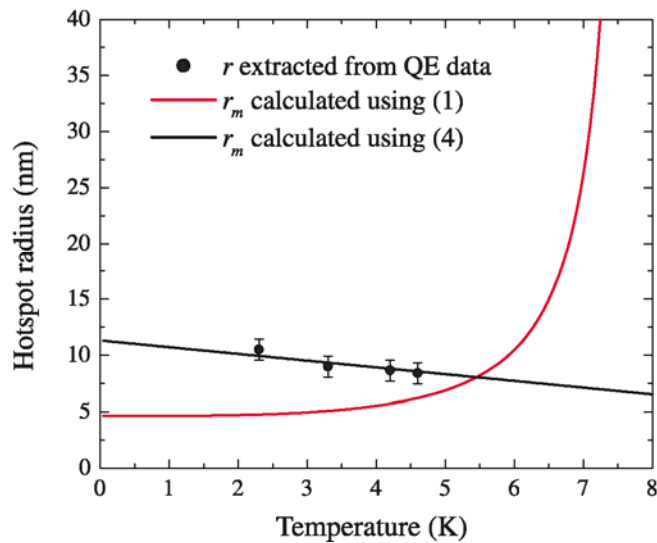


**Figure 5.8** Hotspot radius with a fit using (5.4) (black curve), with  $r_m$  from (5.1) for comparison.

It is important to emphasize here that the need for approximations described above stems from the difficulty in solving directly the nonlinear differential heat flow equation. The heat flow equation is treated in detail in [36],[69],[70]. It is likely that the fitting parameter of 0.34 for the N-S boundary propagation arises due to these approximations. We also know that the NbN film is not thermally insulated, as was assumed in our derivation of  $v$ . Finally, [71] and [72] showed that the N-S boundary velocity depends on the bias current density in a linear manner. Taking into consideration the above restrictions, we believe that the above model explains the experimentally observed QE dependence on temperature quite well, as demonstrated in Fig. 5.9.

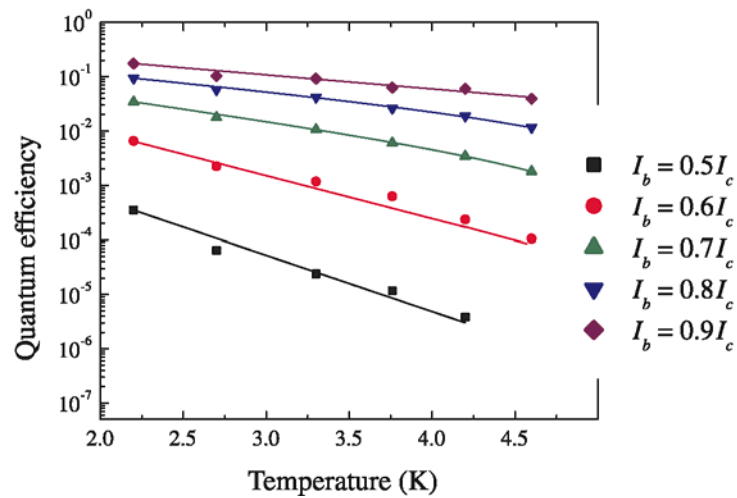


Figure 5.9 Quantum efficiency dependence on temperature at different reduced bias currents.



### 5.3 Fluctuation-enhanced photodetection: vortex-antivortex pairs

In the previous discussion we determined that when  $2r_m < w$ , a photoresponse signal of the superconducting stripe is a trade-off between the bias current and hotspot diameter. If the hotspot is very small,  $r_m \leq \xi$ , Cooper pairs can easily tunnel through it and the resistive region does not form, but the photon energy may still be large enough to nucleate the breaking of a thermally-excited VAP (see Chap. 3 for details). This, in turn, leads to dissipation and transient resistive state similar to dark counts, but now can be seen as a photodetection event. The latter could be, in fact, the dominant photodetection mechanism for optical photons with very low energies (*e.g.*, in the mid-IR), and/or in the case of relatively wide SSPD stripes.

Three nanobridges of different widths were used to observe how the width of the stripe affects photodetection. Figure 5.10 shows the photon count rate as a function of bias current for 150 nm, 330 nm, and 440 nm wide nanobridges, at  $T = 4.2$  K, illuminated with similar incident photon fluxes. We can see that for the 330-nm-wide device, the count rate drops off faster with  $I_b$  decrease, compared with the narrower 150-nm-wide device. In the widest, 440-nm-wide stripe, the photon count rate drops off even faster. The fact that photodetection can be triggered at all in a stripe as wide as 440-nm-wide stripe shows that the photodetection mechanism must indeed be enhanced by VAPs, as our  $J_b/J_c$  criterion in the sidewalks is not likely to be reached. A more thorough discussion of VAP-enhanced photodetection is given by Semenov *et al.* [73]. Here, we would like to conclude that VAP-enhanced photodetection can take place only under the following circumstances: wide stripes,

low photon energies where the resulting hotspot radius is smaller than  $\xi$ , and for low  $I_b$ 's, when the  $J_b$  in the sidewalks does not exceed  $J_c$ .

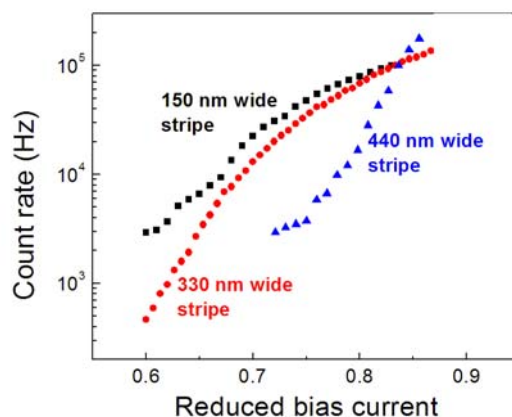


**Figure 5.10 Photon count rate as a function of bias current for bridges of different widths.**

#### 5.4 Summary

Quantum efficiency dependence on temperature measurements demonstrate that the dynamics of hotspot N-S boundary propagation must be considered. The static model, which has been applied previously, does not predict the observed QE behavior. Here, we outlined a dynamic hotspot model, which was used to better describe the photodetection mechanism. We also demonstrated that in some cases, notably mid-IR photons, the photon counting events are due to VAP dynamics instead of the hotspot dynamics.

## Chapter 6 Toward photon-number resolution

### 6.1 Introduction

Certain fast-emerging fields, such as quantum cryptography and linear optical quantum computing, require reliable, high-speed, photon-number resolving (PNR) single photon detectors. Photon-number resolution means the ability of a detector to distinguish single-photon pulses from two-photon pulses, three-photon pulses, and so on. Two types of superconducting detectors which we already mentioned in Chap. 1, namely, the TESs and STJs, exhibit PNR capability and are already available today. The TES detector [8],[9], is operated in the superconducting-normal transition region, and when light is absorbed, the temperature of the sample rises slightly. This change in resistance is proportional to the total optical energy, *i.e.*, number of photons absorbed, which makes the TES a PNR detector. In the case of STJ detectors [6],[7], the absorption of a photon or photons in one of the superconducting electrodes leads to a series of processes in which the photon energy is converted into QPs and phonons. The excited QPs then tunnel through the barrier, and are collected on the other end by SQUID (superconducting quantum interference device) amplifier. The SQUID can resolve the number of QPs and therefore the number of photons incident on the STJ.

As we have stressed several times in this thesis, NbN SSPDs are fast and reliable, however, because of the way they are typically designed and operated today, they are simply photon counters. Achieving PNR by using pixelated SSPDs has been shown [75][76], however, this scheme is extremely expensive, as each pixel requires a separate bias and read-out circuit. The number of pixels represents the number of photons the detector can resolve: the main idea behind the operation is that, *e.g.*, two simultaneous photons will be absorbed and registered by two different pixels, as the probability of both photons being absorbed in the same pixel is extremely low.

In the following, we demonstrate that using our HEMT-based read-out scheme (see Chap. 2 for details), we are able to distinguish the difference between dark counts and photon counts, and simultaneously, we should also be able to resolve pulses containing one and more-than-one photons.

Figure 6.1 compares random time traces of SSPD photoresponse for the standard scheme and the HEMT (500- $\Omega$  load) scheme. Even from such short time trace, we can clearly see that with the standard technique, pulse amplitudes do not vary as much as those where the HEMT is utilized. The SSPD used here, which we will refer to as device S1, has  $I_c = 5.5 \mu\text{A}$  at  $T = 4.2 \text{ K}$ , which is about 3 to 4 times lower than the typical Moscow-patterned and MIT-patterned SSPDs, though its operation is comparable, with  $\text{QE} = 2\%$  at the wavelength  $\lambda = 800 \text{ nm}$ . With the typical  $I_b \leq 5 \mu\text{A}$ , we can estimate the hotspot resistance to be  $R_{hs} \sim 1.2 \text{ k}\Omega$ , from fitting the live pulses with the PSpice model (see Sec. 2.3.1 for PSpice modeling).

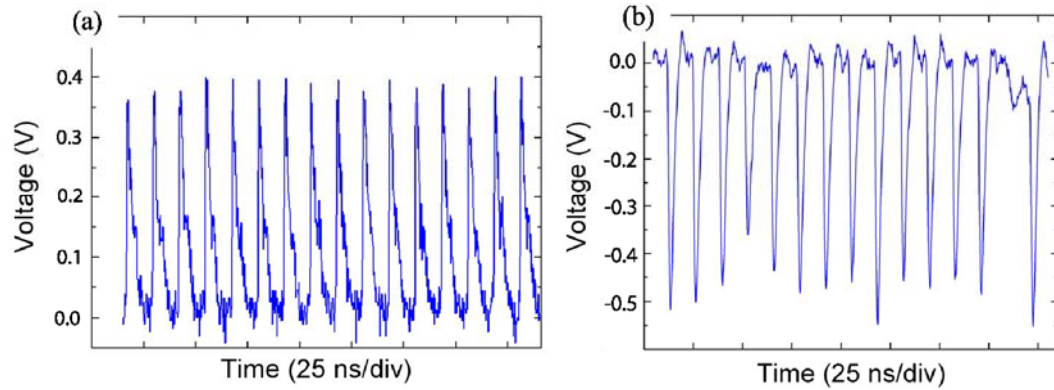


**Figure 6.1** Comparison of live oscilloscope time-domain traces for (a) traditional scheme and (b) HEMT read-out scheme, taken at similar laser intensities, such that  $n \leq 1$  (HEMT is an inverting amplifier, resulting in negative pulses). Here,  $n$  is the number of absorbed photons per pulse.

## 6.2 Experimental results

We used the setup described in detail in Chap. 2 to compare time traces of photon events at different wavelengths with dark count events. Figure 6.2 shows histograms comparing pulse-amplitude distributions of the dark-count [Fig. 6.2(a)] and photon-count events [Figs. 6.2(b) and 6.2(c)], at two different laser intensities. All data were taken at  $I_b = 0.9I_c$ . The photon-count amplitude distributions shown in Figs. 6.2(b) and 6.2(c), collected when the detector was irradiated by 700-nm photons, are clearly wider than that corresponding to the dark counts, even in the single-photon regime [Fig. 6.2(b)], when the average number of photons per pulse in the optical beam incident upon the SSPD is  $n \ll 1$  (e.g., 0.01 photons per pulse). When the laser intensity was increased such that  $n \geq 1$ , we can see that the full-width-at-half-maximum (FWHM) of the distribution shown in Fig. 6.2(c) becomes over 2

times wider than that in Fig. 6.2(a). The amplitude histograms were fitted with Gaussian distributions (red lines).

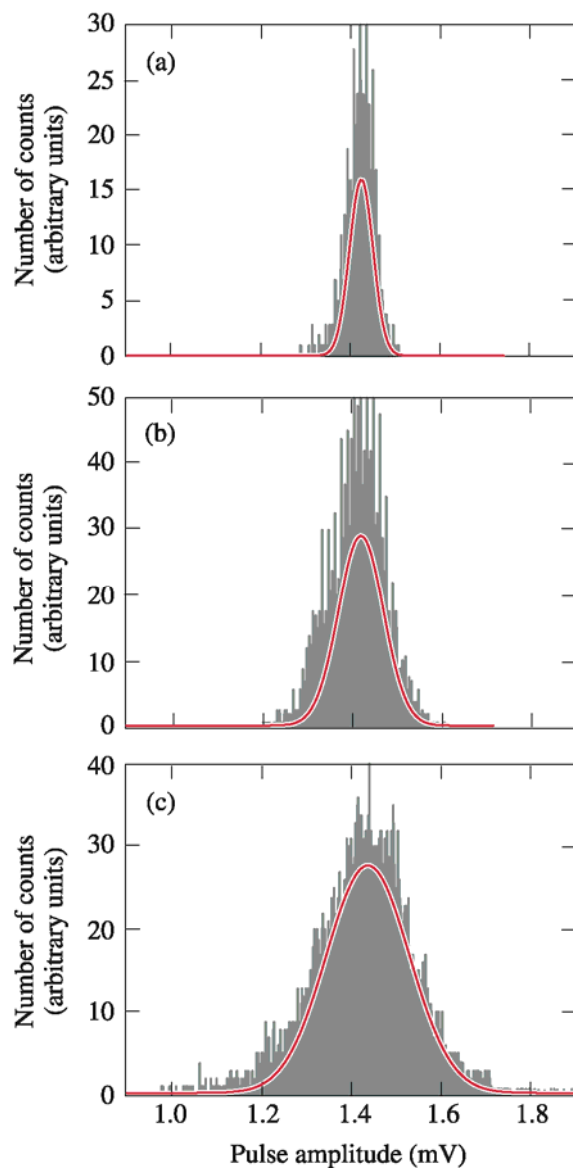


**Figure 6.2** Pulse amplitude histograms of dark counts (a), photon counts at  $\lambda = 700$  nm in the single-photon regime,  $n \ll 1$  (b), and multi-photon regime,  $n \geq 1$  (c). All measurements performed at 4.2 K and at  $I_b = 0.9 I_c$ . The SSPD output voltage amplitudes are divided by the amplifier gain.

The correlation between the beam intensity (average number of photons per pulse) incident upon the SSPD and the Gaussian distribution width of the response signals was very reproducible and, as is presented in Fig. 6.3, it has a dependence on the SSPD  $I_b$ . We can clearly see that the dark-count signals (open squares) exhibit overall the narrowest distribution, which, in addition, is independent of  $I_b$ .

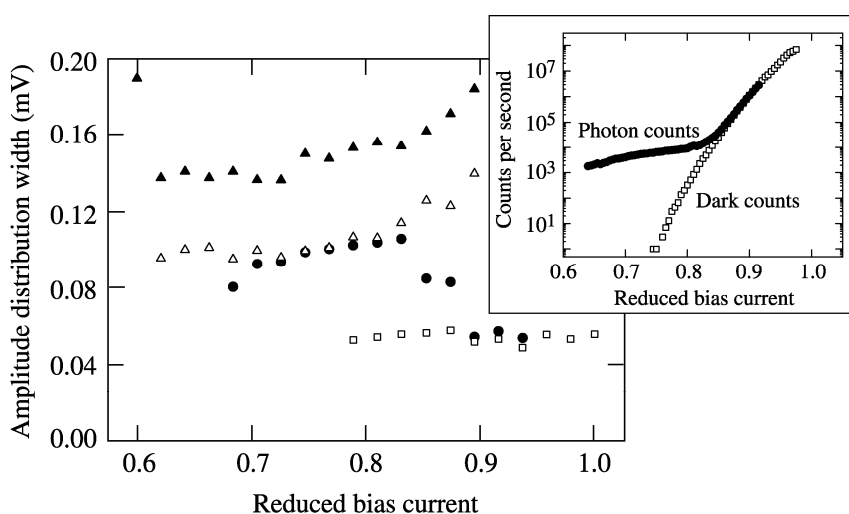


**Figure 6.3** Amplitude distribution width (FWHM of Gaussian fits) for dark counts (open squares),  $n \ll 1$  (closed circles),  $n \leq 1$  (open triangles), and  $n \geq 1$  (closed triangles). The inset shows counting rate as a function of bias current for dark counts (open squares), and  $n \ll 1$  (closed circles).

For photon counts, the general trend is that the distribution width increases somewhat with increasing  $I_b$ , and there is a wide jump between FWHMs corresponding to the multi-photon ( $n \geq 1$ , closed triangles) and single-photon ( $n < 1$ , closed circles and open triangles) illumination. However, for  $n \ll 1$  (closed circles), as  $I_b$  approaches  $I_c$ , the dark counts start to overall dominate over the photon counts and the amplitude distribution width (FWHM), starts to drop around  $I_b = 0.83I_c$ ,

eventually overlapping with open squares at  $I_b > 0.9I_c$ . The latter behavior agrees very well with our earlier observation of dependence of the rate of photon and dark counts on  $I_b/I_c$ , as shown in the inset of Fig. 6.3.

The above trend can be explained in the following way. Because the fabrication of SSPDs is not perfect, we know that there must be a variation in  $w$ , as well as in  $d$ , of our NbN stripes. We also know that experimental  $I_c$  is determined by the narrowest and thinnest section(s) of the stripe. The dark counts are more likely to happen in these particular sections, because that is where  $I_b$  first comes close enough to  $I_c$  in order to reduce the binding energy of VAPs, and eventually break them. Thus, the Joule heating resulting from dark count events produces a region which always has the same resistance, or only slight variations in resistance.

By the same token, photon events can also occur in wider sections of the stripe, because photons have energy and can break enough Cooper pairs in the wider sections to create an initial hotspot, which also grows further due to Joule heating. Fluctuations in the stripe width will translate to fluctuations of final hotspot resistance, which in turn leads to the observed FWHM broadening of our transient voltage pulses. When  $n \geq 1$ , more sections can be activated, leading to even wider distributions, higher fluctuation in the pulse amplitudes, and finally, larger FWHM.

We also used a frequency tripling system, and 1310 nm laser diode, to compare the SSPD photoresponse at three different photon wavelengths: 267 nm, 720 nm, and 1310 nm. Spectral resolution property of SSPDs has already been demonstrated, using either the statistical method [24], or other indirect methods [73].



Amplitude histograms were fit again with Gaussian distributions, and studied in great detail at different laser intensities and bias currents. As a result, we were able to observe a difference in the mean amplitude between the dark counts, and the three aforementioned photon wavelengths, more directly than before, by simply looking at variations of pulse amplitudes on our single-shot oscilloscope.

Figure 6.4(a) shows a plot of mean pulse amplitudes as a function of  $I_b$ , in the single-photon regime for the three different photon wavelengths, and compares them with those of dark counts. We can clearly see that the pulse amplitude increases with the photon-wavelength increase, with the dark counts having the highest amplitude. This is consistent with the earlier observation by Semenov *et al.* [73], we, however, have a different interpretation. Figure 6.4(b) presents FWHM of the same histogram distributions. It is quite obvious that FWHM increases with the photon energy increase, which is logical given that the higher energy photons can break more Cooper pairs, which means they can activate wider sections of the NbN meander. Given these data, it is more likely that the differences in the amplitude observed for different photon energies stem from the nonuniformity of the superconducting stripe, rather than a true, intrinsic spectral resolution. Lower energy photons will activate only the narrowest sections of the stripe, and due to their higher local resistance as opposed to the wider sections, will result in higher pulse amplitudes. This must also be true for dark counts, which are observed to have the highest pulse amplitudes.

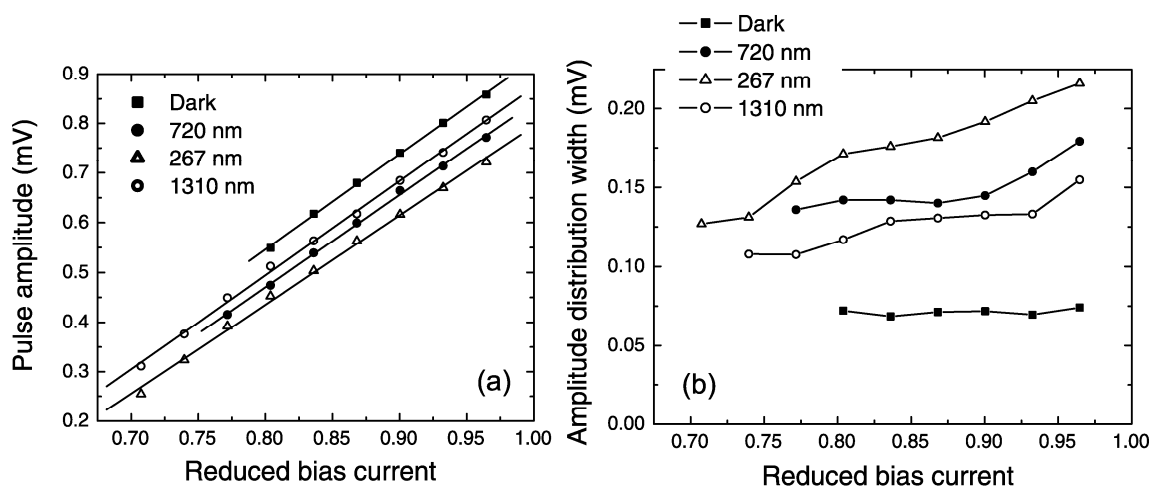


**Figure 6.4** Comparison of (a) mean pulse amplitudes and (b) FWHM of 267 nm photons (open triangles), 720 nm photons (closed circles), 1310 nm photons (open circles), and dark counts (closed squares).

### 6.3 Photon-number resolution

As we mentioned before and was presented by [34], the integrated, cryogenic HEMT read-out should allow us to achieve PNR in SSPDs [77]. For large  $R_L$ 's, the SSPD transient output pulse resulting from photodetection should be proportional in amplitude to the number of photons absorbed, or equivalently, the number of hotspots created in the SSPD. With the estimated hotspot resistance of  $1200 \Omega$ , and with our  $R_L = 500 \Omega$ , it should then be possible, in principle, to distinguish between the single- and multi-photon events.

Indeed, when we increased the laser intensity and the bias current so that the detector started to register nearly every incident light pulse, while the dark counts were still very low, we observed that in time-domain traces some response pulses exhibited visibly higher amplitudes than the rest. Figure 6.5 shows an example of

such a time trace, which is quite convincing, but, of course, it is impossible to conclude that these large pulses were due to double-photon events, instead of, *e.g.*, single-photon events arriving close in time to dark count events, or even resulting from inhomogeneities of our meander and the longer current redistribution time. It was therefore very useful to look at the statistics of the pulse-amplitude distributions once again. This time, the bulk of our measurements was done by varying the laser intensity (mode-locked and twice up-converted light to get  $\lambda = 267$  nm), and  $I_b$ , and collecting amplitudes of several thousand pulses at each value of laser intensity and  $I_b$ . Operating in the UV also resulted in the increased QE of our SSPDs, as it has already been demonstrated by Verevkin *et al.* [31], who showed that QE increases exponentially with the photon wavelength decrease.

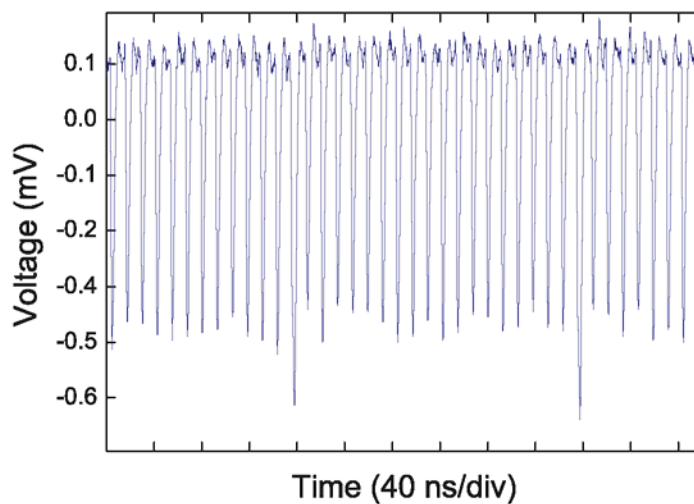


**Figure 6.5** Live oscilloscope time-domain trace, showing higher pulse amplitudes of some pulses.

The results are presented in Figure 6.6. When  $I_b \approx 0.7I_c$ , the amplitude distribution could be easily fit with a simple Gaussian function, as shown in Figs. 6.6(a) and 6.6(b). However, once  $I_b$  reached  $0.9I_c$ , as shown in Figs. 6.6(c) and 6.6(d), we started to see a clear second peak at lower amplitudes, and the distribution now had to be fit with two Gaussians. We believe that both peaks existed in the entire range of  $I_b$ 's, but at higher  $I_b$ , the second peak at lower amplitudes became much more prominent. The latter can be easily explained again by the varying width of the NbN stripe: at higher  $I_b$ , more and more wider sections of the SSPD meander were activated, giving rise to the second peak. This peak should in principle be centered at lower amplitudes, because Joule heating in the wider sections should give rise to lower  $R_{hs}$ , as in those sections we should expect a better heat dissipation into the substrate than that in the narrower sections.

When we plotted the data shown in Figs. 6.6(c) and 6.6(d) on a semi-log scale, as presented in Figs. 6.6(e) and 6.6(f), respectively, it became quite clear that the  $n \leq 1$  regime [Fig. 6.6(f)] exhibits a small third peak, centered around 0.8 mV. This third peak was completely absent in the  $n \ll 1$  regime [Fig. 6.6(e)], and when  $I_b$  was below  $0.78I_c$ . At present, we have no clear interpretation for the existence of the peak. It cannot be related to the dark counts, as they fall-off exponentially with  $I_b$  and are nearly zero below  $0.85I_c$ . Thus, the most reasonable, tentative, explanation is that it is indeed due to multi-photon events associated with two photons simultaneously hitting the SSPD meander, as schematically shown in Fig. 6.7. Furthermore, if we assume that these are indeed single and double-photon events, using these data, we can

calculate the hotspot resistance to be  $R_{hs} \approx 1500 \Omega$ , in rough agreement with the earlier estimate of  $1200 \Omega$ , in favor of PNR interpretation.

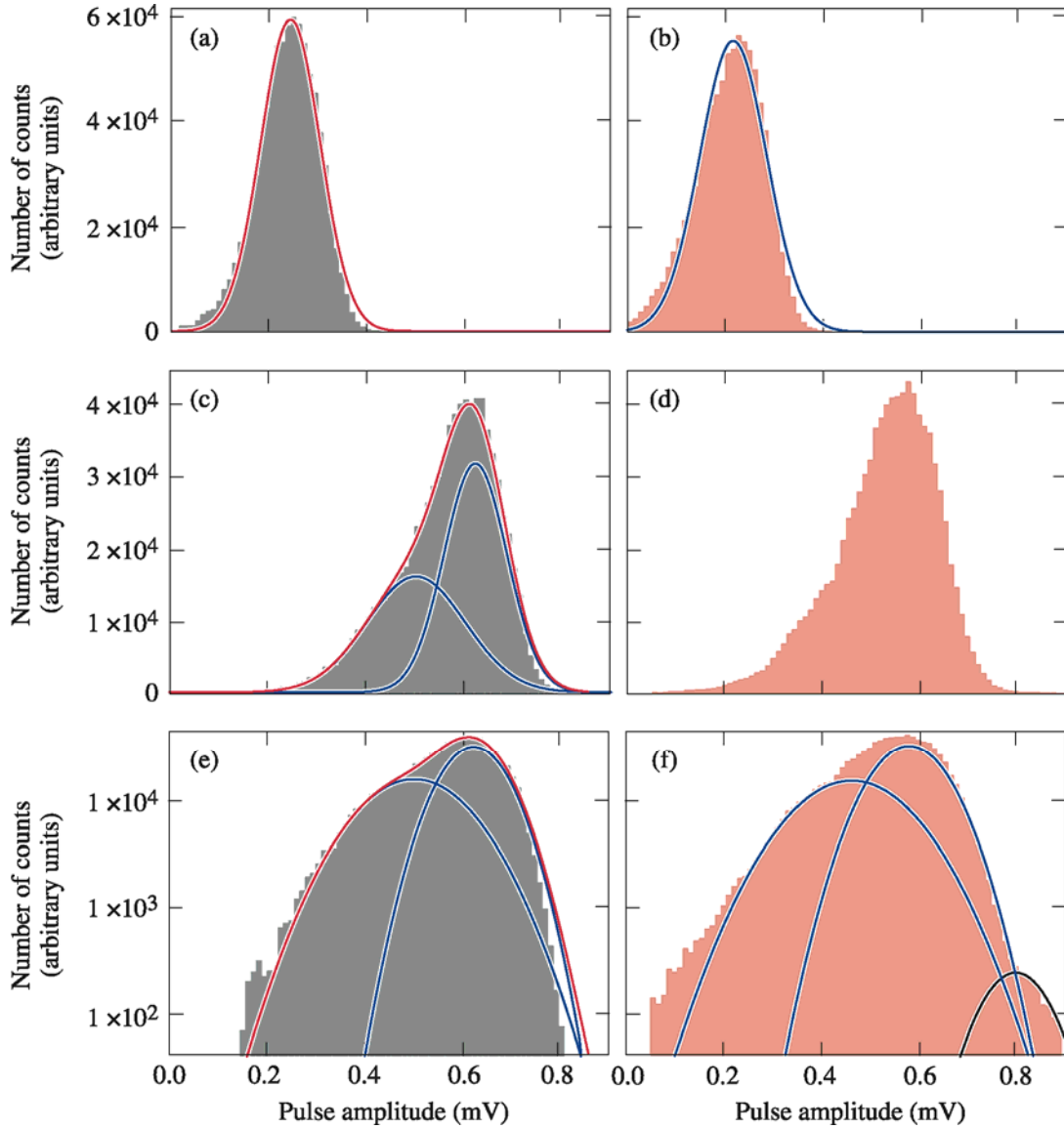


**Figure 6.6** Pulse amplitude histograms for (a)  $n \ll 1$ ,  $I_b = 0.7 I_c$ , (b)  $n \leq 1$ ,  $I_b = 0.7 I_c$ , (c)  $n \ll 1$ ,  $I_b = 0.9 I_c$ , (d)  $n \leq 1$ ,  $I_b = 0.9 I_c$ , (e) semi-log plot of (c), (f) semi-log plot of (d) (black histograms indicate the same incident photon flux for the  $n \ll 1$  regime, red histograms indicate the same incident photon flux for the  $n \leq 1$  regime).

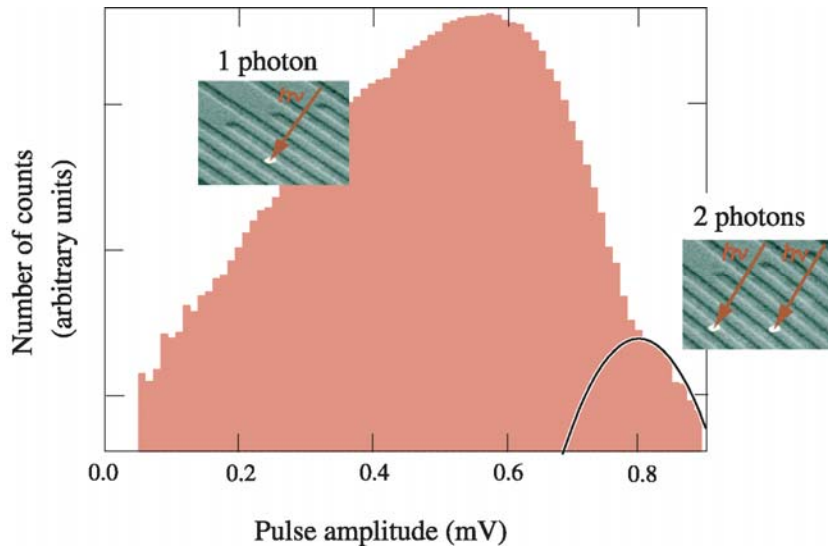


**Figure 6.7 Photon pulse amplitude distribution representing single-photon events (main peak), and possible double-photon events (secondary peak).**

It turned out that the low  $I_c$  of our device S1, whose measurements were presented above, worked to our advantage. We were eventually able to fabricate a very high quality device, with  $QE = 17\%$  at  $T = 4.2\text{ K}$ ,  $\lambda = 800\text{ nm}$ , and  $I_c = 16\ \mu\text{A}$ , referred to as device S2 from now on. We implemented it into the HEMT setup, and repeated the same PNR-type measurements for pulse amplitude distribution widths. In principle, a high-QE device should have a better observable PNR, as the probability of observing a double-photon pulse is proportional to  $QE^2$ .

What we found, however, is that at high enough bias currents ( $I_b \geq 0.9 I_c$ ), and/or high photon fluxes (anything larger than  $n \ll 1$ ), device S2 latched. In other words, for large  $I_c$ ,  $I_b$  must be also large and close to  $I_c$ , and, since Joule heating is  $h = I_b^2 R_{hs}$ , with  $R_L = 500\ \Omega$ , the current in the SSPD was not able to redistribute into

$R_L$  fast enough before run-away heating occurred, sending the entire device into resistive state.

Figure 6.8(a) presents pulse amplitudes a function of bias current, for both dark and photon counts at  $\lambda = 800$  nm. A histogram of collected pulse amplitudes for  $I_b = 0.9 I_c$  is shown in the inset. For this device, however, we did not observe any difference in pulse amplitude between the dark and photon counts, and only a small difference in amplitude distribution width, shown in Fig. 6.8(b). In addition, the distribution width, in terms of the percentage of the mean amplitude, is narrower for device S2, as compared with device S1 (*e.g.*, for  $I_b = 0.9 I_c$ , amplitude distribution width/mean amplitude = 22 % for S1, and 10 % for S2).

The inability to observe PNR stems one or both of the following reasons: first, device S2 latched at photon fluxes higher than  $n \ll 1$ , which means that it could only be operated in the low-flux regime, but in such case the probability of observing two photons simultaneously is nearly zero. Second, device S2 was biased with a current up to 2.5 times higher than device S1, which should give rise to a higher  $R_{hs}$ . Indeed, from simulations we estimated  $R_{hs} \sim 3.5$  k $\Omega$  at  $T = 4.2$  K, which means that  $R_{hs} \gg R_L$ , most of the current redistributes into  $R_L$  during photodetection, and the difference in pulse height for one hotspot as opposed to two hotspots is very small. In fact, for  $R_{hs} \gg R_L$ , the HEMT system starts to operate in a similar mode to the detection scheme with the 50- $\Omega$  load line. The latter is confirmed, as we are not able to observe the difference between dark counts and photon counts.

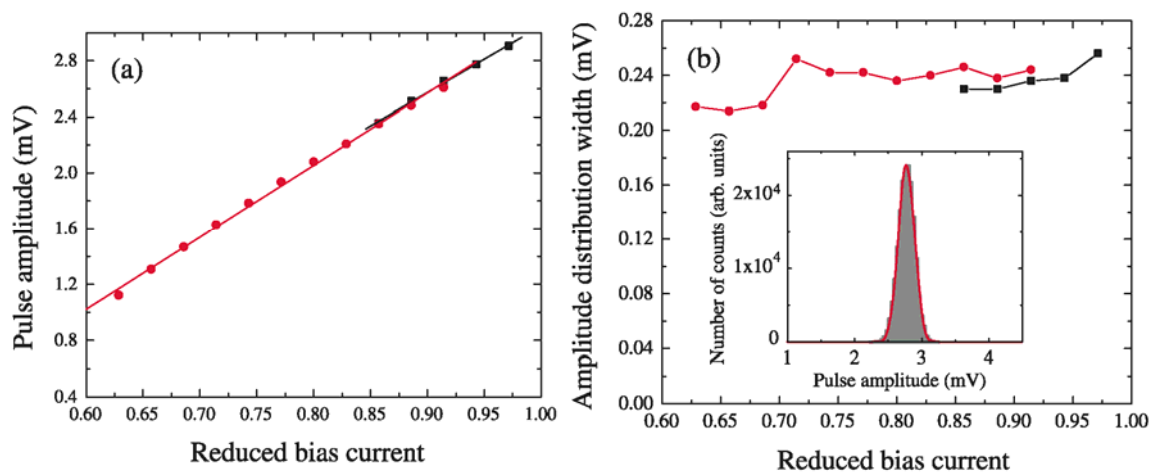


**Figure 6.8** (a) Pulse amplitude and (b) amplitude distribution width as a function of bias current, for dark counts (black squares) and photon counts (red circles) at  $\lambda = 800$  nm. The inset in (b) shows amplitude distribution histogram at  $I_b = 0.9 I_c$ .

## 6.4 Summary

Thus far, our HEMT detection scheme for PNR seems promising only for devices with low  $I_c$ 's. The higher- $I_c$  devices have  $R_{hs} \gg R_L$ , as well as the problem with latching. On the other hand, as we showed in Sec. 2.3.1, increasing  $R_L$  only increases the underdamping of the circuit, which makes the device un-operational. One may attempt to decrease the parasitic capacitance of the circuit board, which would be difficult to do, as the board capacitance is already quite low. That would not guarantee, however, that the device would stop latching.

The most promising approach, I believe, is to design SSPDs with an intentionally  $I_c$ , between 5 and 6  $\mu\text{A}$ , but this approach has its own implications. In order to achieve a high-QE, low- $I_c$  device, one has to fabricate a much narrower ( $\sim 50$  nm wide), but still uniform NbN stripe, an obviously daunting task. Unfortunately,



this would increase the device  $L_k$  twice, as  $L_k$  is inversely proportional to the cross-sectional area of the stripe [78], and one would need to compensate for this by making the effective length of the meandering stripe half as long ( $L_k$  is directly proportional to stripe length), resulting in the smaller device active area. I will leave it up to the next Ph.D. student to decide which approach to follow.

## Chapter 7 Conclusions and future work

In this work, we analyzed dissipation mechanisms in low-dimensional superconductors as they relate to dark counts in NbN SSPDs and nanostripes, as well as presented the physics of hotspot dynamics in our detectors. Along with SSPDs, we fabricated several nanostripes with various dimensions, for study of the nanowire transport properties and dark counts. Measured dc  $IV$  characteristics show voltage steps in some of our devices, which are typically associated with PSCs, even though our devices are not truly 1D. However, constricted regions, inhomogeneities, and defects, which are likely to be present in our samples, and can give rise to PSCs even in 2D superconductors. In general, however, we were also able to show that while in the samples with the smallest width, the resistive transition was dominated by PSCs, while in most of our wider samples, broadening of the transition was due to VAPs. Evidence of BKT phase transition, found by measuring  $IV$  characteristics near  $T_c$ , was found in all samples.

Dark counts, which are indistinguishable from photon counts, were investigated by measuring  $R_{dk}$  as a function of  $I_b$ , at different temperatures. We found that  $R_{dk}$  decreases exponentially with decreasing  $I_b$ , and it decreases at a slower rate at higher temperatures, as opposed to low temperatures. We were also able to show that in wider nanostripe samples, as well as samples with a good width uniformity (*i.e.*, free of constrictions and/or inhomogeneities), the dark counts were due to the current

induced VAP unbinding. In SSPDs, at higher temperatures, we could successfully apply the PSC model to  $R_{dk}$ . We believe that since our devices are in a quasi-1D regime, dark counts are due to the superposition of PSCs and VAPs.

In order to probe the hotspot dynamics during photodetection, we measured the dependence of QE on temperature. We found that the N-S boundary propagates with a higher velocity at low temperatures, giving rise to a larger hotspot, which translates to higher QE. The hotspot dynamics are quite complex, and a full understanding is important for future design and improvement of SSPDs.

Finally, we implemented a HEMT-based, high-load read-out setup, which allowed us to achieve some pulse amplitude resolution. Thus far, the 500- $\Omega$  load is still somewhat low, however, higher  $R_L$ 's result in circuit underdamping, which limits the SSPD count rate. In the future, a design is needed which will optimize the trade-offs between  $R_L$ , count rate, and amplitude resolution.

## Bibliography

- [1] Si APD single photon counting module with < 25 dark counts/second (2007), available online, <http://optoelectronics.perkinelmer.com>
- [2] Photon counters (2007), available online, <http://www.idquantique.com>
- [3] A. Tomita and K. Nakamura, "Balanced, gated-mode photon detector for quantum-bit discrimination at 1550 nm," *Opt. Lett.*, vol. 27, no. 20, pp. 1827–1829, 2002.
- [4] G. Ribordy, N. Gisin, O. Guinnard, D. Stucki, M. Wegmuller, and H. Zbinden, "Photon counting at telecom wavelengths with commercial In-GaAs/InP avalanche photodiodes: Current performance," *J. Mod. Opt.*, vol. 51, pp. 1381–1398, 2004.
- [5] Yoshizawa, R. Kaji, and H. Tsuchida, "Gated-mode single-photon detection at 1550 nm by discharge pulse counting," *Appl. Phys. Lett.*, vol. 84, pp. 3606–3608, 2004.
- [6] Peacock, P. Verhoeve, N. Rando, A. van Dordrecht, B. G. Taylor, C. Erd, M. A. C. Perryman, R. Venn, J. Howlett, D. J. Goldie, J. Lumley, and M. Wallis, "Single optical photon detection with a superconducting tunnel junction," *Nature*, vol. 381, pp. 135–137, 1996.
- [7] D. D. E. Martin, P. Verhoeve, A. Peacock, A. van Dordrecht, J. Verveer, and R. Hijmering, "A  $12 \times 10$  pixels superconducting tunnel junction array based spectro-photometer for optical astronomy," *Nucl. Instrum. Methods Phys. Res.*, vol. 520, pp. 512–515, 2004.
- [8] J. Miller, S. W. Nam, J. M. Martinis, and A. V. Sergienko, "Demonstration of a low noise near-infrared photon counter with multiphoton discrimination," *Appl. Phys. Lett.*, vol. 83, pp. 791–793, 2003.
- [9] D. Rosenberg, A. E. Lita, A. J. Miller, and S. W. Nam, "Noise-free high efficiency photon number-resolving detectors," *Phys. Rev. A*, vol. 71, pp. 061803-1–061803-4, 2005.
- [10] G. N. Gol'tsman, O. Okunev, G. Chulkova, A. Lipatov, A. Semenov, K. Smirnov, B. Voronov, A. Dzardanov, C. Williams, and R. Sobolewski, "Picosecond superconducting single-photon optical detector," *Appl. Phys. Lett.*, vol. 79, pp. 705-707 (2001).
- [11] R. Sobolewski, A. Verevkin, G. N. Gol'tsman, A. Lipatov, and K. Wilsher, "Ultrafast superconducting single-photon optical detectors and their applications," *IEEE Trans. Appl. Supercond.*, vol. 13, p. 1151 (2003).
- [12] J. Zhang, W. Slysz, A. Verevking, O. Okuneve, G. Chulkova, A. Korneev, A. Lipatov, G. Gol'tsman, and R. Sobolewski, "Response time characterization of NbN superconducting single-photon detectors," *IEEE Trans. on Appl. Supercon.* 80, (2003).
- [13] J. Zhang *et al.*, "Noninvasive CMOS circuit testing with NbN superconducting single photon detectors," *Electron. Lett.*, vol. 39, pp. 1086-1088 (2003).
- [14] Slysz *et al.*, "Fibre-coupled, single-photon detector based on NbN superconducting nanostructures for quantum communications," Special Issues on Single Photon: Sources, Detectors, Applications, and Measurement Method, *J. Mod. Optics*, vol. 54, pp. 356-326 (2007).

- [15] G. N. Gol'tsman, K. Smirnov, P. Kouminov, B. Voronov, N. Kaurova, V. Drakinsky, J. Zhang, A. Verevkin, and R. Sobolewski, "Fabrication of nanostructured superconducting single-photon detectors," *IEEE Trans. Appl. Supercond.*, vol. 13, pp. 192-195 (2003).
- [16] A. Korneev, P. Kouminov, V. Matvienko, G. Chulkova, K. Smirnov, B. Voronov, G. N. Gol'tsman, M. Currie, W. Lo, K. Wilsher, J. Zhang, W. Slysz, A. Pearlman, A. Verevkin, R. Sobolewski, "Sensitivity and gigahertz counting performance of NbN superconducting single-photon detectors," *App. Phys. Lett.*, vol. 84, 5338 (2004).
- [17] Carlo Williams, "Ultrafast photodetection based on the hot-electron effect in superconductors," Ph.D. thesis, unpublished.
- [18] N. Perrin and C. Vanneste, "Response of superconducting films to a periodic optical irradiation," *Phys. Rev. B*, vol. 28, p. 5150 (1983).
- [19] A. Frenkel, "Mechanism of nonequilibrium optical response of high-temperature superconductors," *Phys. Rev. B* vol. 48, p. 9717 (1993).
- [20] A. Rothwarf and B. N. Taylor, "Measurement of recombination lifetimes insuperconductors," *Phys. Rev. Lett.*, vol. 19, p. 27 (1967).
- [21] A. D. Semenov, G. N. Gol'tsman, and A. A. Korneev, "Quantum detection by current carrying superconducting film," *Physica C*, vol. 351, pp. 349-356 (2001).
- [22] K. S. Il'in, M. Lindgren, M. Currie, A. D. Semenov, G. N. Gol'tsman, and Roman Sobolewski, "Picosecond hot-electron energy relaxation in NbN superconducting photodetectors," *Appl. Phys. Lett.* vol. 76, 2752 (2000).
- [23] A. J. Kerman, E. A. Dauler, W. E. Keicher, J. K. W. Yang, K. K. Berggren, G. Gol'tsman, and B. Voronov, "Kinetic-inductance-limited reset time of superconducting nanowire photon counters," *Appl. Phys. Lett.*, vol. 88, p. 111116 (2006).
- [24] E. Reiger, S. Dorenbos, V. Zwiller, A. Korneev, G. Chulkova, I. Milostnaya, O. Minaeva, G. Gol'tsman, J. Kitaygorsky, D. Pan, W. Slysz, A. Jukna, R. Sobolewski, "Spectroscopy with nanostructured superconducting single-photon detectors," *IEEE J. Sel. Topics Quant. Elec.*, vol. 13, 934 (2007).
- [25] K. M. Rosfjord, J. K. W. Yang, E. A. Dauler, A. J. Kerman, V. Anant, B. M. Voronov, G. N. Gol'tsman, K. K. Berggren, "Nanowire single-photon detector with an integrated optical cavity and anti-reflection coating," *Opt. Express*, vol. 14, 527 (2006).
- [26] R. H. Hadfield, J. L. Habif, J. Schlafer, R. E. Schwall, and S. W. Nam, "Quantum key distribution at 1550 nm with twin superconducting singlephoton detectors," *Appl. Phys. Lett.*, vol. 89, pp. 241129-1–241129-3, Dec. 2006.
- [27] M. J. Stevens, R. H. Hadfield, R. E. Schwall, S. W. Nam, R. P. Mirin, and J. A. Gupta, "Fast lifetime measurements of infrared emitters using a low-jitter superconducting single-photon detector," *Appl. Phys. Lett.*, vol. 89, pp. 031109-1–031109-3, Jul. 2006.
- [28] R. H. Hadfield, M. J. Stevens, S. S. Gruber, A. J. Miller, R. E. Schwall, R. P. Mirin, and S. W. Nam, "Single photon source characterization with a superconducting single photon detector," *Opt. Express*, vol. 13, no. 26, pp. 10846–10853, 2005.

- [29] M. A. Jaspan, J. L. Habif, R. H. Hadfield, and S. W. Nam, "Heralding of telecommunication photon pairs with a superconducting single photon detector," *Appl. Phys. Lett.*, vol. 89, pp. 031112-1–031112-3, 2006.
- [30] B. S. Robinson, A. J. Kerman, E. A. Dauler, R. J. Barron, D. O. Caplan, M. L. Stevens, J. J. Carney, S. A. Hamilton, J. K. W. Yang, and K. K. Berggren, "781 Mbit/s photon-counting optical communications using a superconducting nanowire detector," *Opt. Lett.*, vol. 31, no. 4, pp. 444–446, Feb. 2006.
- [31] A. Verevkin, J. Zhang, R. Sobolewski, A. Lipatov, O. Okunev, G. Chulkova, A. Korneev, K. Smirnov, G. N. Gol'tsman, and A. Semenov, "Detection efficiency of large-active-area NbN single-photon superconducting detectors in the ultraviolet to near-infrared range," *Appl. Phys. Lett.*, vol. 80, pp. 4687–4689 (2002).
- [32] A. Korneev, P. Kouminov, V. Matvienko, G. Chulkova, K. Smirnov, B. Voronov, G. N. Gol'tsman, M. Currie, W. Lo, K. Wilsher, J. Zhang, W. Slysz, A. Pearlman, A. Verevkin, R. Sobolewski, "Sensitivity and gigahertz counting performance of NbN superconducting single-photon detectors," *Appl. Phys. Lett.* vol. 84, 5338 (2004).
- [33] J. Kitaygorsky, J. Zhang, A. Verevkin, A. Korneev, V. Matvienko, P. Kouminov, K. Smirnov, B. Voronov, G. Gol'tsman, R. Sobolewski, "Origin of dark counts in nanostructured NbN single-photon detectors," *IEEE Trans. Appl. Supercon.*, vol.15, 545, (2005).
- [34] M. Bell, A. Antipov, B. Karasik, A. Sergeev, V. Mitin, A. Verevkin, "Photon-number resolving detection with sequentially connected nanowires," *IEEE Trans. Appl. Supercon.*, vol. 17, 289 (2007).
- [35] R. H. Hadfield, A. J. Miller, S. W. Nam, R. L. Kautz, and R. E. Schwall. "Lowfrequency phase locking in high-inductance superconducting nanowires." *Appl. Phys. Lett.*, vol. 87, 203505 (2005).
- [36] J. K. W. Yang, A. J. Kerman, E. A. Dauler, V. Anant, K. M. Rosfjord, K. K. Berggren, "Modeling the electrical and thermal response of superconducting nanowire single-photon detectors." *IEEE Trans. Appl. Supercon.*, vol. 17, 581 (2007).
- [37] T. Van Duzer and C. W. Turner, *Superconductive devices and circuits*, Second edition, Prentice Hall PTR, p. 357, (1998).
- [38] A. F. Hebard and A. T. Fiory, "Vortex dynamics in two-dimensional superconductors," *Physica* 109 & 110B, 1637 (1982).
- [39] L.G. Aslamasov, A.I. Larkin, "The influence of fluctuations pairing of electrons on the conductivity of normal metal," *Phys. Lett. A*, vol. 26, 238 (1968).
- [40] C.N. Lau, N. Markovic, M. Bockrath, A. Bezryadin, M. Tinkham, "Quantum phase slips in superconducting nanowires," *Phys. Rev. Lett.*, vol. 87, 217003-1 (2001).
- [41] M. Tinkham and C.N. Lau, "Quantum limit to phase coherence in thin superconducting wires," *Appl. Phys. Lett.*, vol. 80, 2946 (2002).
- [42] J. M. Kosterlitz, D. J. Thouless, "Ordering, metastability, and phase transitions in two-dimensional systems", *J. Phys. C*, vol. 6, p. 1181 (1973).

- [43] Z. L. Bereizinskii, *Zh. Eksp. Teor. Fis.*, vol. 61, p. 1144 (1971).
- [44] B. I. Halperin and D. R. Nelson, "Resistive transition in superconducting films," *J. Low Temp. Phys.*, vol. 36, p. 599 (1979).
- [45] A. T. Fiory, A. F. Hebard, W. I. Glaberson, "Superconducting phase transitions in indium/indium-oxide thin-film composites," *Phys. Rev. B*, vol. 28, p. 5075 (1983).
- [46] A. M. Kadin, K. Epstein, and A. M. Goldman, "Renormalization and the Kosterlitz Thouless transition in a two-dimensional superconductor," *Phys. Rev. B*, vol. 27, pp. 6691-6702 (1983).
- [47] J. E. Mooij, "Two-dimensional transition in superconducting films and junction arrays," in *Percolation, localization, and superconductivity*, A. M. Goldman and S. A. Wolf, Eds., NATO ASI, series B, vol. 109. New York: Plenum Press, pp. 325-370 (1984).
- [48] A. M. Kadin, "Duality and fluxonics in superconducting devices," *Journ. Appl. Phys.*, vol. 68, 5741 (1990).
- [49] K. K. Likharev, "Superconducting weak links", *Rev. Mod. Phys.*, vol. 51, p. 101 (1979).
- [50] W. A. Little, "Decay of persistent currents in small superconductors," *Phys. Rev.*, vol. 156, 396 (1967).
- [51] J. S. Langer and V. Ambegaokar, "Intrinsic resistive transition in narrow superconducting channels," *Phys. Rev.*, vol. 164, pp. 498-510 (1967).
- [52] D. E. McCumber and B. I. Halperin, "Time scale of intrinsic resistive fluctuations in thin superconducting wires," *Phys. Rev. B*, vol. 1, pp. 1054-1070 (1970).
- [53] W. J. Skocpol, M. R. Beasley, M. Tinkham, "Phase-slip centers and nonequilibrium processes in superconducting tin microbridges," *J. Low Temp. Phys.*, vol. 16, 145 (1974).
- [54] M. Tinkham, *Introduction to Superconductivity*, 2nd ed., International Series in Pure and Applied Physics. New York: McGraw-Hill, pp. 288-293 (1996).
- [55] H.-T. Elze, I. Sarcevic, "Statistical field theory of multiparticle density fluctuations," *Phys. Rev. Lett.*, vol. 68, 1988 (1992).
- [56] F. Altomare, A. M. Chang, M. R. Melloch, Y. Hong, C. W. Tu, "Evidence for macroscopic quantum tunneling of phase slips in long one-dimensional superconducting Al wires," *Phys. Rev. Lett.*, vol. 97, 017001 (2006).
- [57] M. Tian, J. Wang, J. S. Kurtz, Y. Liu, M. H. W. Chan, T. S. Mayer, T. E. Mallouk, "Dissipation in quasi-one-dimensional superconducting single-crystal Sn nanowires," *Phys. Rev. B*, vol. 71, 104521 (2005).
- [58] M. Bell, A. Sergeev, V. Mitin, J. Bird, A. Verevkin, G. Gol'tsman, "One-dimensional resistive states in quasi-two-dimensional superconductors: experiment and theory," *Phys. Rev. B*, vol. 76, 094521 (2007).
- [59] S. L. Chu, A. T. Bollinger, A. Bezryadin, "Phase slips in superconducting films with constrictions," *Phys. Rev. B*, vol. 70, 214506 (2004).

- [60] P. Mikheenko, X. Deng, S. Gildert, M. S. Coclough, R. A. Smith, C. M. Muirhead, P. D. Prewett, J. Teng, "Phase slips in submicrometer YBaCuO Bridges," *Phys. Rev. B*, vol. 72, 174506 (2005).
- [61] J. M. Repaci, C. Kwon, Q. Li, X. Jiang, T. Venkatessan, R. E. Glover III, C. J. Lob, and R. S. Newrock, "Absence of a Kosterlitz-Thouless transition in ultrathin YBa<sub>2</sub>Cu<sub>3</sub>O<sub>7-d</sub> films," *Phys. Rev. B*, vol. 54, pp. R9674-R9677 (1996).
- [62] A. Engel, A. D. Semenov, H. -W. Hübers, K. Il'in and M. Siegel, "Fluctuation effects in superconducting nanostrips," *Physica C*, vol. 444, pp. 12-18, (2006).
- [63] L. Romano, C. Paracchini, "Current effect on vortex-antivortex depairing in type-II superconductors," *Phys. Rev. B*, vol. 62, 5349 (2000).
- [64] A. M. Kadin, M. Leung, and A. D. Smith, "Photon-assisted vortex depairing in two-dimensional superconductors," *Phys. Rev. Lett.*, vol. 65, pp. 3193-3196 (1990).
- [65] A. Engel, A. Semenov, H. -W. Hübers, K. Il'in, and M. Siegel, "Fluctuations and dark count rates in superconducting NbN single-photon detectors," *Phys. Stat. Sol. C*, vol. 2, pp. 1668-1673 (2005).
- [66] K. Il'in, M. Siegel, A. Semenov, A. Engel, and H. -W. Hübers, "Critical current of Nb and NbN thin-film structures: The cross-section dependence," *Phys. Stat. Sol. C*, vol. 2, pp. 1680-1687 (2005).
- [67] A. Jukna, "Investigation of photoresponse to a single photon in biased NbN superconducting stripe", to be submitted to *Phys. Rev. B*.
- [68] M. Stuiyinga, J. E. Mooij, T. M. Klapwijk, "Current-induced relaxation of charge imbalance in superconducting phase-slip centers," *J. Low Temp. Phys.*, vol. 46, 555 (1982).
- [69] A. V. Gurevich, R. G. Mints, "Self-heating in normal metals and superconductors," *Rev. Mod. Phys.*, vol. 59, 941 (1987).
- [70] W. J. Skocpol, M. R. Beasley, M. Tinkham, "Self-heating hotspots in superconducting thin-film microbridges," *J. Appl. Phys.*, vol. 45, 4054 (1974).
- [71] C.N. Whetstone, C.E. Roos, "Thermal Phase Transitions in Superconducting Nb-Zr Alloys." *J. Appl. Phys.*, vol. 36, 783 (1965).
- [72] W. H. Cherry, J. I. Gittleman, "Thermal and electrodynamic aspects of the superconductive transition process." *Solid-State Electronics*, vol. 1, 287 (1960).
- [73] P. H. Haas, A. Semenov, H.-W. Hübers, J. Beyer, A. Kirste, T. Schurig, K. Il'in, M. Siegel, A. Engel, A. Smirnov, "Spectral sensitivity and spectral resolution of superconducting single-photon detectors," *IEEE Trans. Appl. Supercon.*, vol. 17, 298 (2007).
- [74] J. Zhang, W. Slysz, A. Pearlman, A. Verevkin, R. Sobolewski, O. Okunev, G. Chulkova, G.N. Gol'tsman, "Time delay of resistive-state formation in superconducting stripes excited by single optical photons." *Phys. Rev. B*, vol. 67 132508 (2003).



- [75] E. A. Dauler, B. S. Robinson, A. J. Kerman, J. K. W. Yang, K. M. Rosfjord, V. Anant, B. Voronov, G. Gol'tsman, K. K. Berggren, "Multi-element superconducting nanowire single-photon detector," *IEEE Trans. Appl. Supercon.*, vol. 17, 279 (2007).
- [76] A. Divochiy, F. Marsisi, D. Bitauld, A. Gaggero, R. Leoni, F. Mattioli, A. Korneev, V. Seleznev, N. Kaurova, O. Minaeva, G. Gol'tsman, K. G. Lagoudakis, M. Benkhaoul, F. Levy, A. Fiore, "Superconducting nanowire photon-number resolving detector at telecommunication wavelengths," *Nature Photonics*, vol. 2, 302 (2008).
- [77] J. Kitaygorsky, R. Shouten, S. Dorenbos, E. Reiger, V. Zwiller, R. Sobolewski, "Resolving dark pulses from photon pulses in NbN superconducting single-photon detectors," to be published in *J. Mod. Opt.*
- [78] Aaron Pearlman, "Ultrafast NbN single-photon optical detectors for quantum communications," Ph.D. thesis, unpublished.